

Novel Photostructurable Polymer for On-Board Optical Interconnects
Enabled by Femtosecond Direct Laser Writing

Zur Erlangung des akademischen Grades eines
DOKTORS DER INGENIEURWISSENSCHAFTEN (Dr.-Ing.)
von der KIT-Fakultät für Elektrotechnik und Informationstechnik des
Karlsruher Instituts für Technologie (KIT)

angenommene

DISSERTATION

von

Ho Hoai Duc NGUYEN

Tag der mündlichen Prüfung: 04.03.2021
Hauptreferent: Prof. Christian Koos
Korreferent(en): Prof. Ulrich Lemmer

Preface

Throughout this research project, I was blessed with guidance, support, and encouragement from various institutions, researchers, colleagues, friends, and family. In this preface, I would like name a few to express my sincere appreciation.

It all started in a summer afternoon of the year 2011. In his office at Institute of Microstructure Technology (IMT), Dr. Jürgen Mohr, described to me the idea of bringing the third dimension to optical interconnects and the high risk of developing a novel photosensitive polymer. From that day on, I am deeply indebted to my supervisor not only for giving me the opportunity to research on this exciting project, but also for his valuable guidance and excellent support both professionally and personally. Special thanks should be given to Uwe Hollenbach, who was also in that interview, for mentoring and working with me during and after this *POLALI3D* project. He also conducted project communications to *German Federal Ministry of Economics* and to our project partner *micro resist technology GmbH*.

My special thanks are extended to Prof. Dr. Christian Koos for accepting me as a PhD. student at Department of Electrical Engineering and Information Technology (ETIT), Karlsruhe Institute of Technology (KIT). He was the supervisor of my master thesis and introduced me to this PhD. thesis. It was a great pleasure working with him and knowing him as a person. His help and advice were always there whenever I needed.

I am deeply indebted to my mentor - Martin Lauer for not only nurturing my personal development throughout my Ph.D. but also pushing for my thesis defense. Administrative assistance provided by Kerstin Kalesta and Lisa Böringer was greatly appreciated. Without them, more than 500 samples could not have been fabricated, characterized and recorded within 3 and half years.

I wish to acknowledge a fruitful collaboration with our project partner, micro resist technology GmbH. By name I would like to thank Ute Ostrzinski, Karl Pfeifer,

Dr. Stefan Pfirrmann, and Anja Voigt for creating and improving photosensitive materials for *POLALI3D*.

Support from multidisciplinary colleagues at KIT brought further understanding, more results and, sometimes, new ideas to the research. Therefore, I would like to thank:

- Stefan Hengsbach for helping me with Photonic Profession-3D laser lithography system from Nanoscribe GmbH and for reading my papers; his friendship and support made my work in the cleanroom more exciting and memorable.
- Paul Abaffy for capturing scanning electron microscope (SEM) Micrograph and inspiring discussions.
- Heinrich Sieber for guiding me through fabrication and measurement setups for polymer waveguides.
- My colleagues and also good friends: Radwanul Hasan Siddique, Sentayehu Fetene Wondimu, Muhammad Rodlin Billah, Shyam Sundar Adhikari and Valentina Bykovskaya for sharing with me all the good, the bad and the ugly of doing a doctoral thesis.
- Nicole Lindenmann, Tobias Hoose, Philipp-Immanuel Dietrich. Matthias Blaicher for extending my knowledge on photopolymerization and troubleshooting direct laser writing; in particular Tobias Hoose for producing the B-spline trajectories for bend loss analysis.

A very great gratitude goes out to all at Centre for Microsystems Technology, Ghent University (Ugent), Belgium; with a special mention to Prof. Geert Van Steenberge for accepting me as a visiting researcher and strong guidance during my stay. Prof. Jeroen Missinne provided the inputs for Lumerical simulation. Other colleagues Prof. Erwin Bosman, Steven Van Put, Ahmed Elmogi, Andres Desmet, Celine Vanhaverbeke, Bart Plovie, Patricia Khashayar, Jindrich Windels, Yang Yang, Prof. Benoit Bakeroot, Prof. Herbert De Smet, Dr. Pieter Bauwens, Dr. Kamalpreet Kaur, Nadine Carchon, Kristof Dhaenens, Dr. Frederik Leys, Katrien Vanneste, Nuria Teigell Beneitez, Andrés Felipe Vasquez Quintero, to name a few, brought extra

happiness and worthiness to my 6-months at Ugent with their hospitality, assistance and encouragement.

This work was funded by German Federal Ministry of Economics (KF 2308204MU2) and partly supported by Karlsruhe School of Optics and Photonics (KSOP). The research equipment used in this work was partly provided by Karlsruhe Nano Micro Facility (KNMF, www.kit.edu/knmf), a Helmholtz Research Infrastructure at Karlsruhe Institute of Technology (KIT). Visiting Researcher Scholarships for Ugent stay was funded by Karlsruhe House of Young Scientists (KHYS); particularly Gaby Weick for administrative backing.

I wish to thank Prof. Uli Lemmer (LTI/IMT, KIT) for his acceptance to be my second examiner and for making KSOP a great school to study and. Thanks to my dissertation committee for their time and support.

Special thanks to Thai Son Nguyen (Institute for Anthropomatics, KIT) for helping with the thesis printout.

Assistance provided by my students was greatly appreciated: Ngoc Minh Tran and Fadi Al Salti for near field patterns measurements; Purnima Polamarasetty for polymer molecular modeling in Avogadro; Chengcheng Yan for polarization dependent loss measurement; Sara Bahrieh and Shima Nasiri for lab preparations.

This thesis is dedicated to my mother, my wife, my brother for always providing me unconditional support and love. Finally, to my wonderful children, Duc Viet and Hannah: growing up together with you especially during this study has been the hardest yet worthies period of my life.

Karlsruhe, December 2017

Ho Hoai Duc Nguyen

Abstract

Integrated optics has emerged as a promising solution to the electronic interconnect bottleneck, enabling high bandwidth density and low power consumption. Recently, confining photochemical and physical reactions in a micro-volume has given an extra dimension to optical interconnection using glass or polymer materials. Three-dimensional waveguides can connect, combine, or split the optical signal among any blocks in all dimensions. However, due to the insufficient refractive index contrast, the reliable fabrication of free-form and single-mode three-dimensional buried waveguides is a challenge.

This thesis presents a new concept to tackle this challenge using the combination of femtosecond direct laser writing in polymer and external diffusion of a gaseous monomer. Direct laser writing with two-photon absorption was used to initiate cross-linking along a programmed trajectory, to form the waveguide core. A sufficient refractive index contrast was produced for guiding single-mode Gaussian beams. The variation of the scanning speed and laser intensity enabled to vary the feature-sizes. This fabrication method requires only one layer of a single material without masks, contact, or wet processing.

By using this novel technique, three-dimensional waveguide array, fan-in/fan-out, splitters were fabricated. Free-form three-dimensional waveguides have high potential to improve the density and flexibility of optical interconnects at board level.

Kurzfassung

Die integrierte Optik hat sich als vielversprechende Lösung für elektronische Verbindungen erwiesen, die eine hohe Bandbreitendichte und einen geringen Stromverbrauch ermöglicht. Seit kurzem ist es möglich photochemische und physikalische Reaktionen auf ein Mikrovolumen zu begrenzen. Dies hat der optischen Verbindungstechnik unter Verwendung von Glas oder Polymer eine zusätzliche Dimension verliehen. Dreidimensionale Wellenleiter können das optische Signal zwischen Blöcken aller Dimensionen verbinden, kombinieren oder aufteilen. Die Erhöhung des Brechungsindex ist jedoch immer noch eine Herausforderung für die Herstellung stabiler Freiform- und monomodaler Wellenleiter mit dreidimensionaler Ausdehnung, welche sich innerhalb der Platine befinden.

Diese Dissertation stellt ein neues Konzept vor, um dieser Herausforderung zu begegnen, indem direktes Femtosekunden-Laserschreiben in Polymer und externe Diffusion eines gasförmigen Monomers verwendet wird. Direktes Laserschreiben mit Zwei-Photonen-Absorption wurde verwendet, um die Vernetzung entlang eines vorher definierten Pfades zur Bildung des Wellenleiterkerns zu initiieren. Es wurde ein ausreichender Brechungsindexkontrast erzeugt, um gaußförmige Strahlen mit einem Modus zu führen. Feature-Größen konnten durch Variieren der Scangeschwindigkeit und der Laserintensität linear angepasst werden. Dieses Herstellungsverfahren erfordert nur eine Schicht eines einzelnen Materials ohne Masken-, Kontakt- oder Nassbearbeitung.

Durch Verwendung dieser neuartigen Methode wurden dreidimensionale optische Wellenleiter-Arrays, Fan-in/Fan-out- und Splitter-Strukturen hergestellt. Dreidimensionale freiforme Wellenleiter haben ein hohes Potential zur Verbesserung der Packungsdichte und Flexibilität optischer Verbindungen auf Platinenebene.

Contents

Preface	ii
Abstract.....	v
Kurzfassung	vi
Contents	vii
Chapter 1. Introduction	11
1.1 Motivation	11
1.2 Objective and outline	14
Chapter 2. Materials.....	17
2.1 Optical materials for waveguides	17
2.1.1 Material requirements.....	17
2.1.2 Processing requirements	18
2.1.3 State of the art polymer materials	19
2.2 Host guest systems	20
2.2.1 Internal diffusion versus external diffusion.....	20
2.2.2 Material components	22
2.3 Material characterizations	26
2.3.1 Gravimetric analysis.....	27
2.3.2 Transmission loss	28
2.3.3 Dispersion	29
2.3.4 Prebake temperature.....	31
2.3.5 Photosensitizer	32
Chapter 3. Fabrication	34
3.1 Planar waveguide patterning techniques	34
3.1.1 Three dimensional waveguide fabrication method.....	35

3.2	<i>Femtosecond direct laser writing</i>	36
3.2.1	Three-dimensional two-photon lithography system	36
3.2.2	Optical impairments	38
3.3	<i>Modification of voxel size</i>	40
3.4	<i>Fabrication steps</i>	44
3.4.1	Spin coating	46
3.4.2	Prebake process	47
3.4.3	Waveguide writing	48
3.4.4	Post exposure bake	52
3.4.5	External diffusion	55
3.4.6	Flood exposure and hard bake	64
3.4.7	Conclusion	68
3.4.7.1	Advantages and limitations of the fabrication method	69
Chapter 4.	Optical structures.....	71
4.1	<i>Single optical waveguides</i>	71
4.1.1	Surface roughness and end facet and surface microscope analysis.....	71
4.1.2	Index profile	73
4.1.3	Near field pattern.....	74
4.1.4	Far field pattern.....	77
4.1.5	Transmission loss.....	78
4.1.6	Bend loss	80
4.1.7	Polarization dependent loss	81
4.1.7.1	Measurement methods	83
4.1.7.2	Experiments and Analysis	84
4.2	<i>Multilayer waveguide arrays</i>	85
4.3	<i>Fanin Fanouts</i>	86
4.4	<i>Reliability</i>	88
Chapter 5.	System integration	90

5.1	<i>Concept</i>	90
5.2	<i>Fabrication method</i>	91
5.2.1	Multi-layer waveguide description.....	92
5.2.2	Contact pad metallization using image reversal lithography.....	92
5.2.3	LIFT micro bumps.....	93
5.2.4	Laser ablation for mirror definition	94
5.2.5	Chip placing.....	97
5.3	<i>Characterization</i>	99
5.3.1	Surface roughness by laser ablation.....	99
5.3.2	Near field pattern	101
5.3.3	Insertion loss.....	102
Chapter 6.	Conclusion and outlook	105
6.1	<i>Conclusions</i>	105
6.2	<i>Outlook</i>	106
Bibliography		107
Appendix		119
Fabrication notes		120
Failed Approaches.....		122
	<i>Varying the solvent concentration</i>	122
	<i>PEB at lower temperatures</i>	122
List of figures		125
List of publications		131
Curriculum Vitae		133

Chapter 1. Introduction

1.1 Motivation

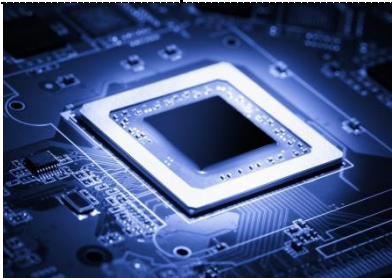


Global data traffic is growing explosively with an annual rate of around 50 percent [1] and information, and communication technology constitutes more than 10 percent of the total electric power consumption in most industrialized countries [2]. Those are the reasons why solutions for high speed, high spectral efficiency and low power consumption in data communication are increasingly in focus.

Optical interconnects are indisputably needed for transmitting information in telecommunications, local area network, and rack-to-rack links. Recently, bringing the optical domain to board level has emerged as a potential solution for the physical limitations of electrical interconnections in terms of bandwidth density and power consumption [3].

Table 1.1 tells the history trend of communication links from single-mode fiber for World Wide Web to integrated waveguides in chip and board levels. Short-distance optical interconnects have been developed using various methods such as free-space optics [4,5], optical fibers [6,7] and waveguide stacks [8,9]. Despite of offering a high density, free-space optical links requires a complicated structuring as they consist of lenses and prisms. Optical fibers at board-level provide immense flexibility and low transmission loss but demand troublesome packaging owing to the vast number of fibers in a short range. Polymer based waveguides have emerged as high potential candidates for on-board interconnects since direct waveguides can eliminate optical fibers and connectors. Additionally, they are low cost and flexible. Embedded multimode waveguides were particularly favored thanks to their relaxed alignment tolerances and compatibility with printed circuit board (PCB) fabrication processes. However, single-mode waveguides are now in focus due to their coupling efficiency to on-chip single-mode integrated waveguides and single-mode fibers [10]. Nonetheless, stacking layer after layer of

planar waveguides needs significant alignment effort and time, especially in case of single mode waveguides with tight alignment tolerance. Finally, standard lithography involves multiple process steps and multiple photopolymer material layers.

Table 1.1 Trends of communication links from long distance to short distance

Computer Communication		Datacom				Telecom		
Chip level	Board level	Back plane	Cabinet	LAN	Access	Metro	Core	
conductive tracks, waveguides		Multi-mode fiber			Single- mode fiber			
1 cm	10 cm	1 m	10 m	100 m	1 km	10 km	100 km	
100000	10000	100-	1000	100	100	10	1	1 line
In research	2010-now	2010	2005	2005	1990s	1990s	1980s	
								
*		**				***		

* www.shutterstock.com ** Sandman Media Inc. *** www.greatfon.com

Since first reported in 1965 [11], three-dimensional direct laser writing (3D-DLW) has attracted much attention thanks to its unique capability of fabricating arbitrary three-dimensional nano- and micro-structures, [12,13] particularly in integrated optics. [14]. Femtosecond laser is the most popular laser source for its short energy deposition time and high peak energy compared to continuous wave and

nanosecond lasers [15]. Femtosecond laser pulses excite multi-photon absorption within a tightly localized volume in the material, modifying its physical and chemical properties including the refractive index. The written pattern, with high enough refractive index contrast, allows guiding of optical signals freely in 3D, providing a promising solution to overcome the density and complexity limit of conventional planar (two-dimensional) integrated optics. The two main materials used in 3D-DLW are glass and photopolymer.

By two-photon absorption, 3D-DLW in glass generates a micro-plasma that permanently modifies the refractive index of the glass in the focal volume [15,16]. Moving the sample or the laser beam in a computer-programmed 3D path creates a free-form waveguide. Compared to glass, polymer materials offer greater flexibility and optical sensitivity at a lower cost. 3D-DLW in photopolymer utilizes both one-photon and multi-photon absorption via continuous laser irradiation and ultrashort laser pulses respectively. The former demands less energy but offers limited confinement of the polymerization volume [17]. The latter, in contrast, allows for strong confinement of the multi-photon absorption volume, enabling freeform structures. Nevertheless, sufficient refractive index contrast in embedded polymer waveguides is still a great challenge. Unlike freeform waveguides for chip-scale interconnects [18,19], here, an acceptable index contrast must be achieved without wet developing unexposed structures. Several approaches have been demonstrated using the difference between radical and cationic monomers [20] or between thermal cure and photolytic cure [21]. Unfortunately, the main drawback of these approaches is that the polymerization can continue via thermal or one-photon processes which in turn leads to reduced structural stability and hence high optical losses (e.g. 1.3 dB/cm, [21]). Alternatively, 3D freeform waveguides have been fabricated using a micro-dispenser system to dispense core monomer into liquid cladding monomer via a needle [22]. However, this approach is only suitable for multimode waveguides because of the large core sizes.

In this thesis, we report a novel fabrication technique utilizing external diffusion of a low-index guest monomer into the photopolymer matrix in order to increase the refractive index contrast. Specifically, we demonstrate the manufacturing of symmetric single-mode 3D waveguides with adjustable core dimensions in polymer via two-photon lithography. Four by two waveguide arrays and three-core fan-outs were fabricated with compact pitch size, low cross talk and high precision.

1.2 Objective and outline

The aim of this thesis is to develop a novel fabrication process for 3D free-form polymer waveguides and demonstration with system integration. A new host-guest photopolymer system is represented enabling non-stacking single-mode waveguide arrays for optical interconnect with high bandwidth and low power consumption. The swelling effect and thermal impact of the external diffusion from gaseous monomer to oligomer was investigated. Optical properties of the fabricated waveguides such as guiding modes, transmission loss and polarization dependence were characterized. The in-situ alignment of this fabrication method can be illustrated by a multi-layer waveguide array. System integration using VCSEL arrays and detector arrays at communication wavelength for transmitting optical signal at board-level is the fundamental application. Fan-in/ Fan-out structures connecting multicore fiber (MCF) to a fiber ribbon are fabricated utilizing flexibility of 3D waveguides. Furthermore, a novel optical functionality so called 3D integrated optical router is introduced, which allows for routing a waveguide matrix input to an arbitrary order at the waveguide matrix output. This new functionality increases the spectral density of on-board interconnections while decreasing the complexity of the electrical wire bonding; see Figure 1.1.

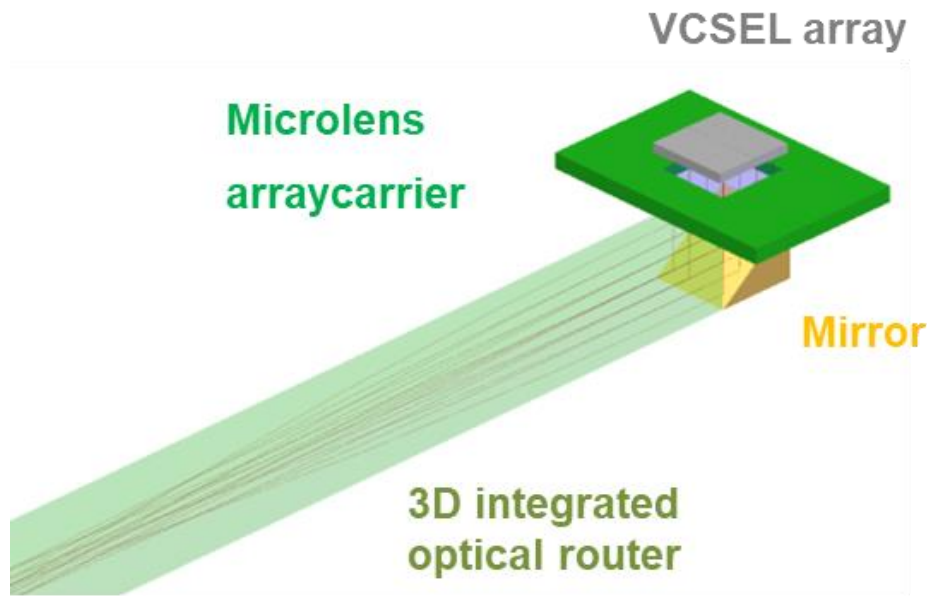


Figure 1.1 The concept of the 3D optical router to perform all the optical interconnections on board and in three dimensions equipped with vertical-cavity surface-emitting lasers (VCSEL) and mirrors.

This unique yet simple fabrication process should possess various advantages over other waveguide fabrication methods. It requires only one layer of a single material. Its rapid prototyping technique no longer involves masks, contact or any wet chemical process steps such as wet etching. The number of material layers and fabrication steps are independent of waveguide layers or structural complexity. High index contrast offers a good confinement of the guided light inside the core.

This thesis is structured in the following way:

Chapter 2 studies the developments of innovative photosensitive materials and methods that could add the third dimension to integrated waveguides. The novel material system and fabrication approach that met all requirements are introduced. Material components and characteristics such as transmission loss, dispersion, change of refractive index prove the feasibility of the concept.

Chapter 3 describes the fabrication flow that requires only one layer of a single material utilizing three dimensional direct laser writing. External diffusion of a

gaseous monomer induced a sufficient and permanent index contrast for light guiding. Laser power and writing speed allow the modification of the waveguide core sizes both horizontally and vertically.

Chapter 4 characterizes fabricated waveguides including surface roughness, index profile, near field pattern, far field pattern, transmission loss, bend loss, polarization loss, and reliability. Demonstration of waveguide arrays and fan-ins/fan-outs showcases the exemplary applications of the concept.

Chapter 5 focuses on the flip-chip optoelectronic integration of the waveguide arrays using ablated total internal reflection mirror and laser induced forward transfer. Decoupling the horizontal pitch size and vertical pitch size boosts the compactness of integrated optical interconnects.

Chapter 6 concludes the thesis, and introduces potential utilizations of 3D integrated polymer waveguides. Further development of the material system indicates promising improvement of the photo-sensitivity and surface roughness.

Chapter 2. Materials

Next generation of on-board optical waveguides needs more flexibility and higher compactness. The existing optical material market is rapidly expanding, though commercial availability still is a major drawback. Main challenges are still durability, transmission loss and fabrication complexity. This work aims to bring an extra dimension in the current planar PCB boards. Therefore, a novel photostructurable polymer and a unique fabrication method were developed. This chapter gives an overview of the material requirements, the existing materials, development of novel materials and material characterization.

2.1 Optical materials for waveguides

Long-haul communication deploys single-mode fibers using fused silica as the standard material. For integrated optics, on the contrary, there exists no obvious choice for the best material that fits all the components and applications. Specific component and application, therefore, defines their own material selection criteria. This section emphasizes on requirements for board-level interconnects.

2.1.1 Material requirements

Waveguide materials for integrated optics need to meet several main requirements in order to guide the light signal efficiently.

Low absorption at optical communication wavelengths: The material must show low optical losses at a wavelength of 850 nm or 1.3 and 1.55 μm for data communication applications. For optical waveguides of board level dimensions (20 – 60 cm) a material absorption of below 0.5 dB/cm is required.

Surface quality: In optical waveguides for light guiding, in particular single mode guiding, scattering loss is a dominant factor for transmission loss. Hence, surface

modulation or large-scale irregularity introduced by waveguide processing should be negligible.

Flexibility: The flexibility of optical waveguide material accounts for the possibilities of embedding or burying waveguides in arbitrary surface. Compatibility to integration of optoelectronic components is also an important requirement for optical material.

Adjustable Refractive index: The tunability of the material refractive index is desirable for complex structure with different core sizes e.g. splitter, combiner. Furthermore, one single material can be used as core and cladding with sufficient index contrast.

2.1.2 Processing requirements

Materials for optical waveguides in optical PCB must be compatible with established PCB manufacture technology such as thermal or chemical resistance.

Deposition: The material must be able to form a uniform layer over the substrate by casting techniques such as spin-coating, doctor blading.

Process compatibility: Various waveguide fabrication processes have been reported in the past. When a preferred process is chosen, the optical material should be compatible with that process, show low surface roughness and perfect reproducibility. Compatibility with printed circuit board manufacturing, direct patterning, and large-area scalability includes casting, no oxygen inhibition, adhesion properties, UV-curability.

Good adhesion: The optical material layers should show good adhesion to the rigid PCB board as well as to each other since a waveguide stack consists of different cladding and core layers. Delamination is a frequent reliability problem when stacking different types of material layers.

Chemical resistance and thermal resistance: Reliability of optical polymer waveguides is important for the fabrication process and during operation in opto-

electronics circuitry and components. Apart from high temperature, material should be resistant against chemicals such as acetone, isopropanol, and etchants during manufacturing and operation.

Cost: As for all applications, the cost is one of the major factors, which determines the speed of introduction of the application into the market. For high-end low throughput applications, this constraints is however less prominent.

2.1.3 State of the art polymer materials

Numerous materials used to fabricate optical waveguides for optical communications include Si-based materials (e.g. silicon-on-insulator [23], silicon-organic hybrid [24]), III-V semiconductors (e.g. InP [25], GaAs [26,27]), glasses (e.g. silica [28] , chalcogenides [29,30]), crystal (e.g. lithium niobate [31]) and polymer (e.g. epoxy [32], acrylate [33]). Each type of material possesses its advantages and disadvantages depending on the application.

Table 2.1 List of commercially available polymers for optical integrated waveguides

Commercial polymer [research report]	Group	Suppliers	Transmission Loss [dB/cm]
EpoCore/EpoClad [42]	Epoxy	micro resist technology GmbH	0.2 @850 nm
SU-8 [43]		MicroChem	0.03 @1310 nm
OrmoCore/OrmoClad [44] (ORMOCER®)	organically modified ceramic	micro resist technology GmbH	0.23 @1310 nm
Acrylate [45]	Acrylate	AlliedSignal	0.2 @1310 nm
Halogenated Acrylate [45]		NTT	0.07 @1310 nm
Polyguide™ [46]		DuPont	0.2 @1310 nm
Truemode™ [47]		Exxelis Ltd	0.04 @850 nm
LightLink™ [48]	Polysiloxane	MicroChem	0.3 @1310 nm
OE-4140 UV [49]		Dow Corning	0.04 @850 nm
Ultradel™ 9120D [50]	Fluorinated	Amoco	0.4 @1310 nm
Fluorinated Polyimid [45]	Polyimid	NTT	0.3 @1310 nm

P2ANS [51]	PMMA	Hoechst Celanese	1.0 @1310 nm
Topas® [52]	cyclic olefin copolymers	TOPAS Advanced Polymers	0.5 @850 nm
Cyclotene™ [53]	Benzocyclobutene	Dow Chemical	0.8 @1310 nm

Polymeric materials have shown great potential in integrated optics, interconnects thanks to their desirable properties such as cost effectiveness, high flexibility, large refractive index tunability, high refractive index compared to glass, good adhesion to various substrates, satisfying thermal and chemical stability. Their thermo-optic, and electro-optic properties contributed to high-speed low-voltage electro-optic modulator [34], power-efficient thermo-optic tunable filters [35] and optical switches [36,37]. Their processing flexibility allows hybrids with silicon [38], silica [39] and sol-gel glass [40,41] which combines superior properties of each material.

Various commercially available polymers have been used to fabricate optical integrated waveguides. Table 2.1 lists some of these materials together with basic properties and the related research work.

2.2 Host guest systems

In cooperation with the company *micro resist technology GmbH* [54] a novel photo-structurable host-guest polymer system has been developed.

2.2.1 Internal diffusion versus external diffusion

In case of polymer material a sufficient and adjustable refractive index contrast are the main challenges for polymer materials. The concept of this work is to develop a host guest system, in which the diffusion of guest monomer into the host oligomer matrix should tackle these challenges.

Figure 2.1 compares two approaches for the host-guest systems utilizing internal diffusion and external diffusion.

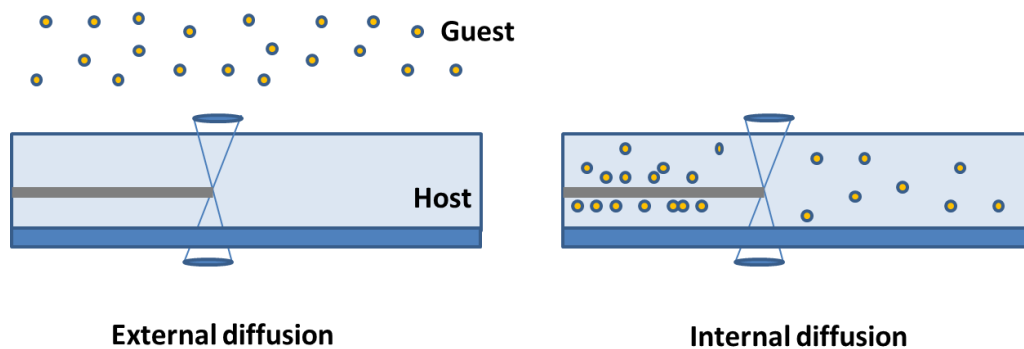


Figure 2.1 The principles of external diffusion (left) and internal diffusion (left)

For **internal diffusion**, the resist contains a mass fraction of a non-volatile monomer in addition to the oligomer. The laser writing includes the monomers into the oligomer network. The resulting decline in the concentration of free monomer molecules leads to an in-plane diffusion process of monomers from the unexposed regions to the exposed waveguide core areas. As the monomers have a lower refractive index than the oligomer, the lack of monomers in the core region compared to the surrounding material results in a higher refractive index and thus forming the waveguide cores.

External diffusion has a similar principle as internal diffusion. The main difference lies in the fact that a monomer is not mixed in the host resist. This gaseous monomer is only externally diffused into the resist after laser writing. By this way, no monomers are incorporated in the waveguide core causing unwanted reduction of its refractive index.

Table 2.2 shows the host-guests systems tested in our work. Four different host oligomers and three guest monomers were used.

Table 2.2 Host –guest systems using various oligomer and monomer combinations

	Polares 01	Polares 02	Polares 03	Polares 04
Diffusion	external	internal	external	external
Guest/Host wt.%		18.4:81.6	71:29	5.6:94.4
Viscosity [mPas]	11211	23609	9196	17145
Index n_D (25 °C)	1.5458	1.5470	1.5405	1.5463
Initiator	Cyracure	Deuteron+ITX	Cyracure	Deuteron+ITX
Photosensitizer	No	No	No	Yes

The resulting refractive index contrast between the laser-written region and the host matrix in internal diffusion was one order of magnitude lower than in external diffusion. Therefore, the external diffusion method was selected for our work. From here, only this method will be addressed.

2.2.2 Material components

To be able to fabricate single mode waveguides by 3D-DLW and subsequent diffusion of a low-index guest monomer into the photopolymer matrix, a novel epoxy-based photopolymer has been developed. Its main component is an oligomer based on a bisphenol-A diglycidylether. In addition to a photoinitiator, the photopolymer also contains γ -butyrolactone (GBL) solvent which allows for the forming of defect-free films by spin-coating.

The host photoresist: Successful structuring of a host-guest polymer system highly relies on the appropriate combination of host oligomer, photo-initiator, solvent and guest monomer [32]. This host-guest system must induce a permanent and high refractive index modulation while forming homogeneous and tack-free layers.

The host's main component is an oligomer based on a bisphenol-A diglycidylether with a refractive index of 1.59 at 589 nm (sodium D-line) and a glass transition temperature of $T_g = 55$ °C after the first prebake. In addition to a photoinitiator, the photopolymer also contains γ -butyrolactone (GBL) with a refractive index of 1.435

at 589 nm which serves as a solvent that allows for the forming of defect-free films by spin-coating.

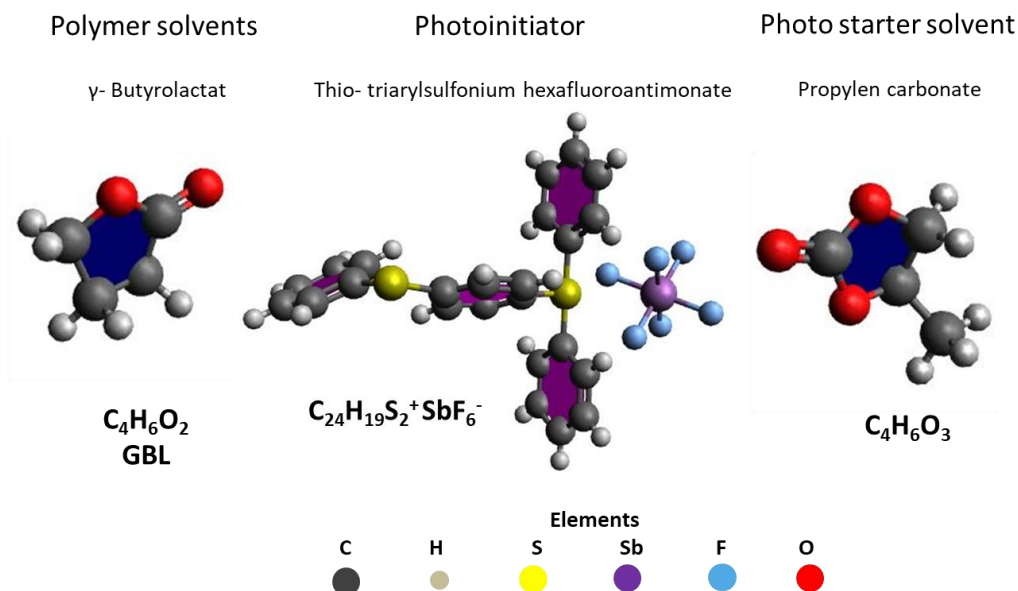


Figure 2.2 Annotated molecular structure of the host components: oligomer's solvent, photoinitiator (PAG) and photoinitiator's solvent [Credit: *SU8 Purnima Polamarasetty, Uwe Hollenbach*]

Figure 2.2 shows the molecular structure of the solvent of the oligomer (GBL), photoinitiator and its solvent (propylen) in 3D using Avogadro molecule editor [55]. The organic solvent GBL weight percent influences the host matrix viscosity [56] and its index of refraction. Furthermore, the residual solvent in the resist after prebake affects the curing of the resist [57].

Various photoinitiators were tested the frame of this thesis. Here, triphenyl sulfonium salt is used as an example for demonstration of crosslinking. Its absorption peak for UV is at 310 nm. The resist is based on a bisphenol-A diglycidylether, whose molecule contains 8 epoxy groups in average, see Figure 2.3. The octafunctional unit is formed by pre-linking the epoxy monomer via CH₂-methylen bridges. The oxirane or epoxy ring can be homopolymerized or reacted with active hydrogen containing compounds such as amines, phenols or acid. The high functionality of the oligomer promotes the formation of covalent bonds within

the oligomer (intermolecular crosslink) itself and between the oligomer (intramolecular crosslink).

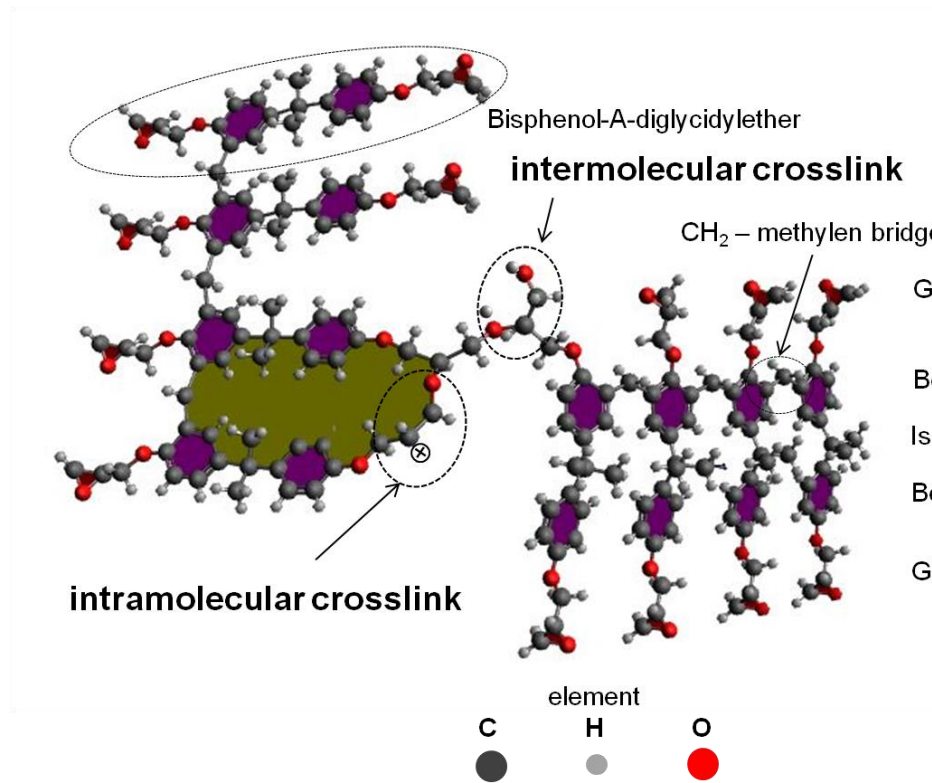


Figure 2.3 Molecular structure host oligomer and its crosslink schemes annotated in 3D using Avogadro molecule editor: Two epoxy oligomers were shown with an octafunctional unit of bisphenol-A diglycidylether containing glycidyl groups, benzene rings and isopropyl group. Intramolecular crosslink, intermolecular crosslink and CH₂-methylene bridge were illustrated

Epoxy resist claims various advantages for the host such as oxygen-insensitivity, negligible shrinkage during cross-linking (as compared to e.g. acrylates) and low toxicity. Moreover, it possesses excellent chemical resistance properties, outstanding adhesion and versatility in cross-linking. This octafunctional unit also provides low molecular weight, high transparency, highly uniform coating and low edge bead [58].

Table 2.3 Reactive Components of the Coating Agent (Host resist) *Propylencarbonat (Solvent of PAG)

Polares01-XP	Epoxy-Oligomer	Solvent (GBL)	PAG	PC*
$n_D = 1,5442$ (theor.), $n_D = 1,5458$ (exper.)	$n_D = 1,5998$	$n_D = 1,4360$	$n_D = 1,5975$	$n_D = 1,4190$

The host polymer Polares01-XP consists of several reactive components with different refractive indices. A refractive index of $n_D = 1,544$ is calculated from the proportions of the chosen composition. The experimentally determined refractive index of the solution is 1.5458 ($\Delta n = 0.0016$). The deviation from the calculation value is in the error margin of the index determination (Table 2.3).

The guest monomer: The guest monomer must have low molecular weight, high volatility, non-toxicity and copolymerisation compatibility with the epoxy matrix. Additionally, it should possess little shrinkage and high index contrast compared to the host epoxy matrix. Another equally important criterion for guest monomer is maintaining the optical performance of the photopolymer surface (e.g. roughness) after diffusion and stabilizing steps. Table 2.4 lists the three main monomers tested in this work and their basic specifications. An aliphatic guest monomer (D1) with molecular weight of 102.13 g/mol has been found satisfying all these requirements. In terms of surface quality after diffusion, there was no change detected in D1 monomer while D2 created a wavy surface (wrinkle) and D3 caused the surface sticky.

Table 2.4 Monomer tested for diffusion

Monomer	D1	D2	D3
Formula Weight [g/mol]	102.13	136.42	215.6
Density [g/cm ³]	1.024	1.042	1.13
Refractive Index n_D	1,446	1,482	1,436

Monomer D1 is soluble in chloroform, methanol. Its boiling point is 122 °C at 70 mm Hg. For demonstration purpose, a glycidyl monomer and its incorporation in the crosslinked network was modelled in Avogadro as shown in Figure 2.4 (left).

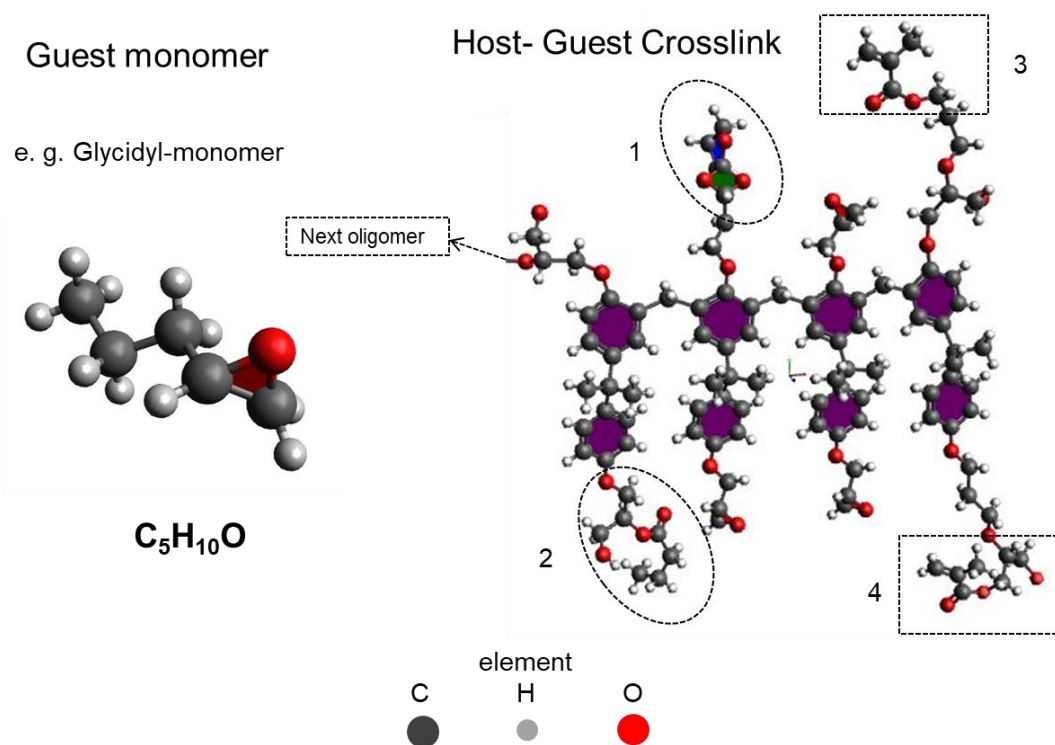


Figure 2.4 Molecular structure of an exemplary guest monomer (left) and crosslink between host oligomer, GBL solvent and monomers; 1,2: crosslinks with GBL; 3,4 crosslinks with monomers

This monomer can crosslink with the oligomer for instance through oligomer's glycidyl group. The incorporation of monomer and GBL into the oligomer matrix is shown in Figure 2.4 (right). Since refractive indices of solvent ($n_D = 1,436$) and monomer ($n_D = 1,446$) are lower than that of host oligomer ($n_D = 1,599$), the crosslink will reduce the photoresist refractive index. A quantitative analysis will be reported in the following material characterization section.

2.3 Material characterizations

This epoxy resin based material exhibits very good optical, mechanical and thermal characteristics. The relaxation behavior and the refractive index can be adjusted by different reactive diluents or by post-exposure bake (PEB). External

diffusion of gaseous low index monomer is another possibility to change the materials characteristics locally, as it occurs mainly in the uncured matrix and hardly in the locally exposed, cross-linked pattern. I.e. the measured refractive index of the two-photon cross-linked volume before and after external diffusion barely changed in the whole spectrum.

2.3.1 Gravimetric analysis

The mass percent of solvent, i.e. solvent weight proportion in total solutions or in total solids alters the viscosity of the resist formulation and influences the maximal thickness achieved by spin coating. Compared to the other components of the resist formulation, the solvent has a relatively low refractive index so that solvent residues, which are, still present in the resist layers after a prebake have a strong impact on the refractive index of the entire layer.

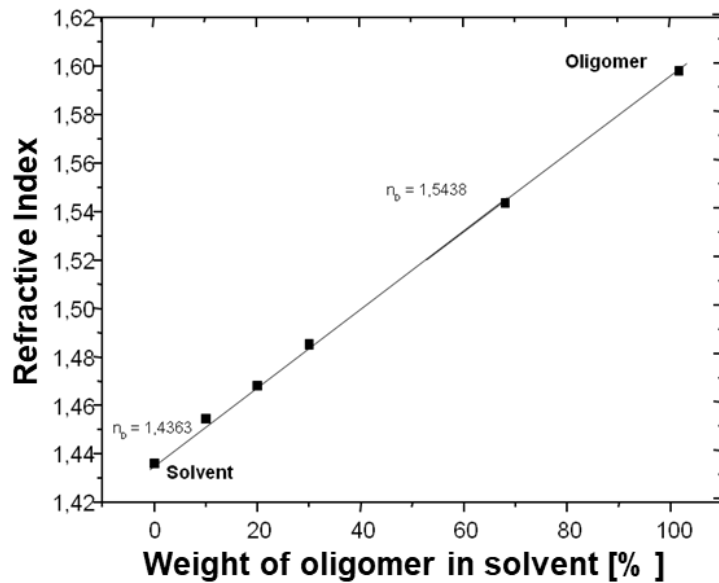


Figure 2.5 4 Refractive index of an epoxide oligomer solution as a function of the solids content: The refractive index was experimentally determined using an Abbe refractometer up to an oligomer content of 68%. The value of the refractive index for the pure epoxy oligomer ($n_D = 1.5998$) was determined by extrapolation of the straight line (dashed line).

As an example, Figure 2.5 shows the change in the refractive index of an epoxide oligomer solution as a function of the solvent content or solid content. The fitting

slope shows that a fraction of 1% solvent in the oligomer layer results in a change in the refractive index of 0.0015. This results in a refractive index of 1.599 for the pure oligomer. The proportion of solution was determined gravimetrically. Gravimetric analysis considers the sample weights before and after prebake; the difference between the two masses gives the mass of solvent evaporated. This makes it possible to estimate the ideal prebake conditions for solvent-free or nearly solvent-free coatings.

2.3.2 Transmission loss

Absorption is of a great importance for polymer materials. Polymeric materials exhibit large absorptions in the ultraviolet due to fundamental excitations of their electrons. Electronic and vibrational absorptions are major causes of optical loss. Electronic absorptions in colorless polymers are very unlikely to contribute significantly to optical losses in the major telecommunication windows near 1300 nm [59].

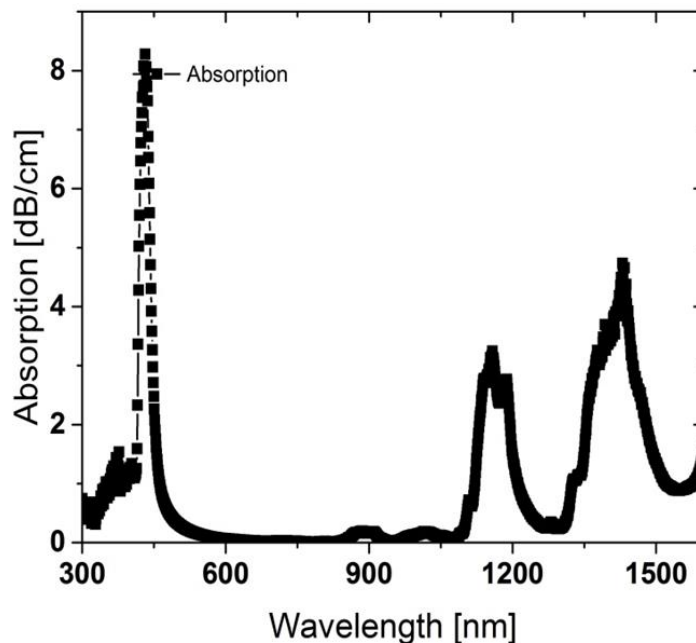


Figure 2.6: Absorption spectrum of the uncured liquid photopolymer: extremely low absorption at 780 nm for local 2-photon absorption and high absorption at 390 nm for UV cure one-photon absorption. Material transmission loss at 850 nm, 1310nm and 1550 nm are 0.04 dB/cm 0.30 dB/cm and 0.85 dB/cm respectively.

Figure 2.6 depicts the measured transmission spectrum of the uncured photopolymer material in liquid. The material is almost transparent at 780 nm and highly absorptive at 390 nm for UV cure. The absorption loss at 850 nm, 1310 nm and 1550 nm are 0.04 dB/cm 0.30 dB/cm and 0.85 dB/cm respectively.

2.3.3 Dispersion

The impact of monomer diffusion on the refractive index of both cured and uncured resist was investigated (Figure 2.7). To determine the dispersion curves of the differently treated resist layers, the Cauchy equation was fitted to refractive index values determined via m-line spectroscopy. Equation (1) and (2) present the Cauchy's equation for the cured photoresist after diffusion (core) and uncured resist after diffusion (cladding) respectively:

$$n_{core}(\lambda) = 1.572 + \frac{7.28 \times 10^{-3}}{\lambda^2} + \frac{4.522 \times 10^{-4}}{\lambda^4} \quad (1)$$

$$n_{clad}(\lambda) = 1.555 + \frac{9.27 \times 10^{-3}}{\lambda^2} - \frac{1.355 \times 10^{-6}}{\lambda^4} \quad (2)$$

where n is the refractive index and λ is the wavelength in micrometers. This dispersion equation was derived by fitting the Cauchy equation to five measured points across the 0.4 – 1.5 μm spectrum plotted as curve 3 and 4 in Figure 2.7.

In Figure 2.7, UV cure at 365 nm wavelength lowers the refractive index of uncured resist slightly by 0.003. Contrary to the usual behavior of the SU-8 resists, the PEB temperatures reduce the resist index below the index level of the pre-cured layer. This reduction of the refractive index cannot be explained by a condensation of the polymer layer. Presumably, additional molecular bonds, which occur to the proper inter- and intramolecular bondings, form the predominant contribution to the reduction of the refractive index. In our case, this is owing to the incorporation of GBL [56] into the cross-linked oligomer matrix.

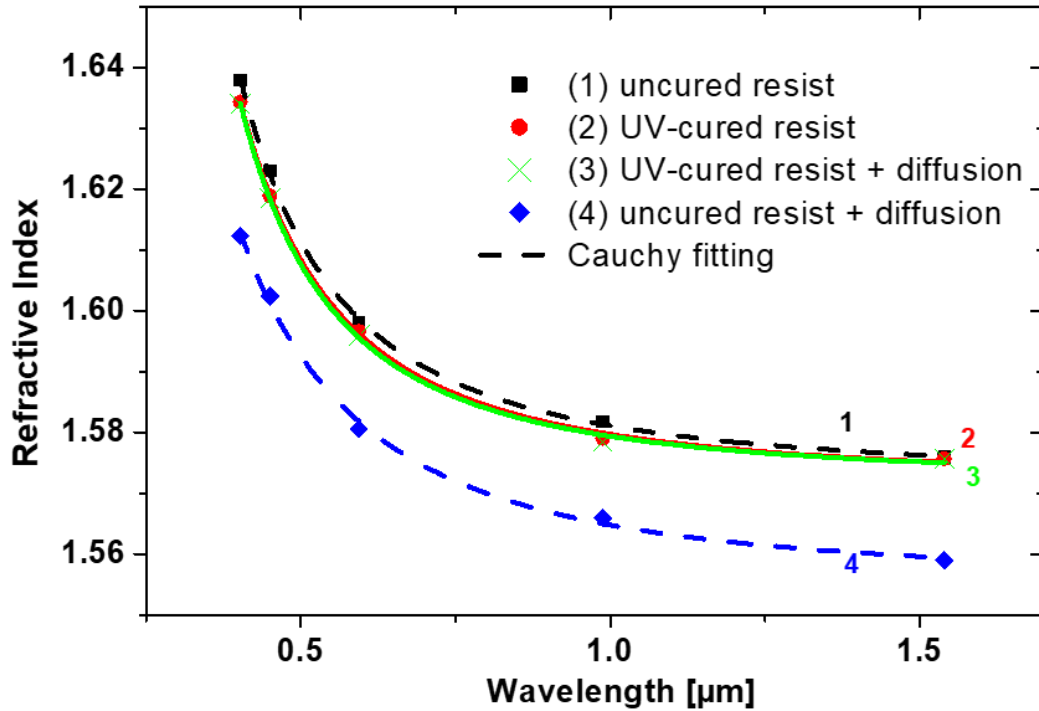


Figure 2.7 Refractive indices of the resist measured at 1.540, 0.988, 0.594, 0.450 and 0.402 μm wavelengths, and their Cauchy fitting dispersion curves. The refractive index of the uncured resist (black, 1) reduces slightly after UV cure at 365 nm and hard bake at 50 $^{\circ}\text{C}$ (red, 2), but decreases more significantly if a low-index monomer was diffused into the photoresist matrix before UV cure and hard bake (blue, 4). The index of previously cured resist (red, 2) hardly changes after the monomer diffusion process (green, 3).

However, the photo-induced index contrast is not sufficient for optical waveguides. Hence, external diffusion of an aliphatic guest monomer was utilized which results in a significant decline of the refractive index by 0.016 (line 4, blue). This reduction is attributed to the lower index of the guest monomer $n_D = 1.445 \pm 0.0005$ relative to the host oligomer $n_D = 1.59 \pm 0.0005$. This experiment also reveals that the index of the cured resist (line 2, red) barely changed after the diffusion process of the guest monomer (line 3, green). In other words, the gaseous monomer hardly diffuses into the polymerized, crosslinked resist. This difference in index contrast generation in the uncured and cured resist is the pre-condition for fabricating 3D buried waveguides via multiple photon lithography.

2.3.4 Prebake temperature

The approach of the process optimization is to keep a considerable amount of the solvent in the resist before exposure. This will allow for high mobility of photo-acid and monomers and therefore polymerization at a low temperature [57,60]. The dispersion curves for the prebake from 50 °C to 140 °C are shown in Figure 2.8.

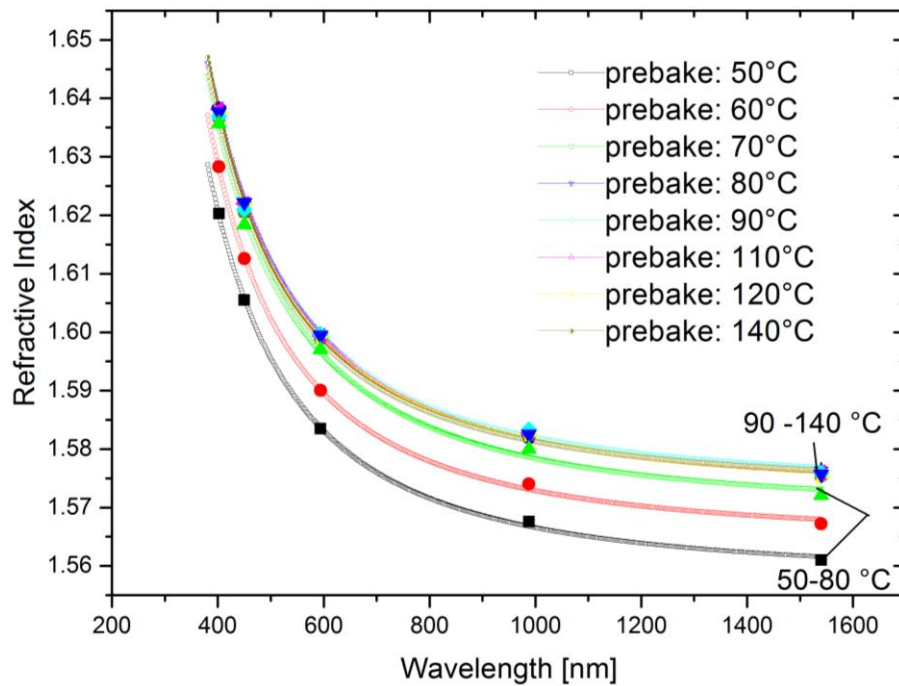


Figure 2.8. Impact of prebake temperature on the resist refractive index

The prebake temperature increases the resist refractive index by evaporating the solvent (GBL). Lower proportion of solvent remaining in the layer leads to higher refractive index. Prebake at 80 °C increases the resist refractive index by 0.016 compared to prebake at 50 °C. From a PB temperature of 80 °C and above, the refractive index is constant. That means that GBL proportion in the layer stays unchanged.

2.3.5 Photosensitizer

A photosensitizer improves the sensitivity of polymer materials at ultraviolet or visible wavelength by absorbing electromagnetic radiation and transferring it to adjacent molecules. This section addresses the impact of adding a photosensitizer to the host guest system. Figure 2.9 (a) represents the absorption spectra of the corresponding photo acid generators (PAG) and the sensitizer. The latter improves the absorption at 390 nm by three orders of magnitude in comparison with the former. SEM (scanning electron microscope) micrographs helped quantify the surface roughness of the waveguide core with and without sensitizer as plotted in (b, c). Various single lines at the writing speed of 100 $\mu\text{m/s}$ and increasing laser powers from front to back were written through two supporting blocks attached to the wafer. The development bath in PGMEA (Propylene glycol monomethyl ether acetate) subsequent to laser writing removed the unexposed resist to disclose the surface roughness, i.e. the periodic surface modulation along the laser scanning direction. This modulation was attributed to the combination of the oscillation of the driving piezo and the change of crosslinking degree corresponding to different laser power. Increasing the material absorption at 390 nm wavelength should reduce this roughness significantly towards the intrinsic oscillation of the translating piezo of $\lambda/20$ [61]. As a result, the added sensitizer reduced the surface roughness from $\lambda/2$ to less than $\lambda/15$. This improvement will reduce further the insertion loss of the multi-layer structure in our host-guest system. Moreover, the energy efficiency of the photoresist improves significantly as illustrated in Figure 2.9 (d). Specifically, the new resist requires less than a third of the laser power to achieve the same feature size.

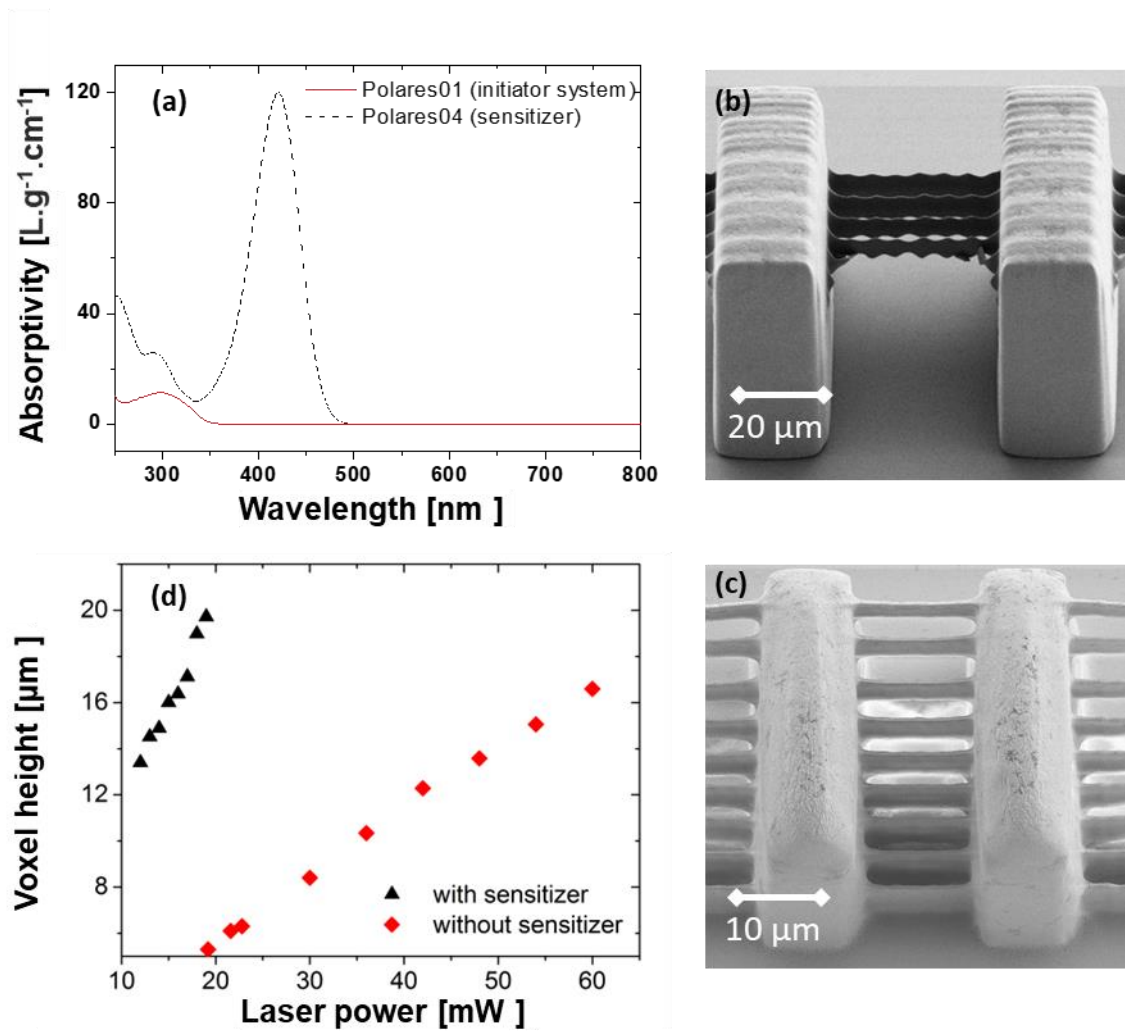


Figure 2.9 (a) Absorption spectra of the corresponding photo acid generators and the sensitizer; Surface roughness of the cured resist after chemical bath of the resist without sensitizer (b) and with the sensitizer (c); (d) Voxel height of waveguide core as a function of laser power of the resist with (black) and without sensitizer (red);

The additional sensitizer requires storage at low temperature before spin coating. However, with dominant improvement of the sensitivity and surface roughness, it is worth adapting the fabrication flow for this potential material.

Chapter 3. Fabrication

In order to enable free-from three-dimensional buried waveguides, it is necessary to think about a new fabrication approach. This chapter describes femtosecond direct laser writing, external diffusion and other steps of the fabrication flow in details.

3.1 Planar waveguide patterning techniques

The basic principle of waveguide patterning is to create the guiding region (core) that has sufficiently higher refractive index than the surrounding region (cladding). The most common waveguide fabrication technologies include, hot embossing, DLW, Etching, Laser ablation, Injection Molding, diffusion (ion-implantation/Ion exchange), Reactive Ion Etching and electron beam irradiation pressure dispensing, direct laser writing and photolithography (citation to be added).

For developing a new material and device, rapid iteration and easy redesign are of great importance. Hot embossing, injection molding involve molds or stamps to transfer a master design to the waveguides, which is time consuming for design modification. They are also limited in terms of processing area and pattern shapes (e.g. undercut). Other non-photolithographic methods such as ion exchange, etching engage numerous steps, and have low yield [59]. Photolithography, an optical means for transferring patterns defined by a mask onto a substrate, is low cost, high yield, and high scalability. Nevertheless, it suffers from mask proximity effects [62].

Polymer materials offer high flexibility in shape, size, and complexity for optical waveguides. However, in most fabrication methods, two different materials are needed for core and cladding. Furthermore, the feature height is limited to the casting thickness of the core layer. Finally, for multilayer arrays, number of process steps increases with number of waveguide layers [63].

3.1.1 Three dimensional waveguide fabrication method

In contrast to traditional planar waveguides with uniform cross section, planar trajectory and index profiles, three-dimensional (3D) waveguides provide high compactness and complexity with arbitrary size, index profile and free-form trajectory. This third dimension could pave the way for new optical functionalities and interconnection platforms. Furthermore, it can improve the packaging density significantly. Hence, the number of research groups focused on 3D waveguides has been growing. Single mode 3D waveguides have been fabricated inside various glasses such as boro-aluminosilicate glass (EAGLE²⁰⁰⁰) [15], bonded phosphate glass (Schott IOG-1) [16], chalcogenide glass [64], or Corning 0215 [65]. Formation of a micro-plasma due to nonlinear absorption permanently modifies the refractive index of the glass in the focal volume. Moving the sample with respect to the laser beam axis in a computer-programmed path creates a free-form waveguide. Nevertheless, this technique provides only limited control over the core dimension and refractive index profile, which is mandatory for complex devices. Organic polymer materials, which are cheaper and easier to integrate, have also been used with femtosecond lasers [20] and continuous wave lasers. [66] The former allows for high confinement of polymerization, i.e. smaller feature size. In contrast, the latter requires less energy. Nevertheless, sufficient refractive index contrast in embedded polymer waveguides is still a great challenge. Unlike freeform waveguides for chip-scale interconnects [18,19], here, an acceptable index contrast must be achieved without wet developing unexposed structures. Several approaches have been demonstrated using the difference between radical and cationic monomers [20] or between thermal cure and photolytic cure [21]. Unfortunately, the main drawback of these approaches is that the polymerization can continue via thermal or one-photon processes which in turn leads to reduced structural stability and hence high optical losses (e.g. 1.3 dB/cm, [21]). Alternatively, 3D freeform waveguides have been fabricated using a micro-dispenser system to dispense core monomer into liquid cladding monomer via a needle [22]. However, this approach is only suitable for multimode

waveguides as a result of the large core sizes. The following will focus on the novel fabrication technique utilizing external diffusion of a low-index guest monomer into the photopolymer matrix in order to increase the refractive index contrast. Specifically, we demonstrate the manufacturing of symmetric single-mode 3D waveguides with adjustable core dimensions in polymer via two-photon lithography.

3.2 Femtosecond direct laser writing

3.2.1 Three-dimensional two-photon lithography system

Figure 3.1 shows the basic schematic of a two-photon lithography system from Nanoscribe GmbH [67]. The laser emits ultrashort pulses of 100 fs at 780 nm wavelength with a repetition rate of 80 MHz, owing to frequency doubling from an Erbium-doped fiber laser at 1560 nm. An acousto-optic modulator (AOM) continuously modulates its power, which can scale up to 70 mW average power. The laser beam is expanded before being split into an objective and a detector setup. The former is an objective with a 63× magnification and a numerical aperture of 0.75. The latter detects sample interfaces and corrects its tilt angles via the intensity of the reflected light. A piezoelectric 3D scanning stage drives the sample tracking the programmed coordinates given from the computer, enabling the writing of free-form paths into the material. The microscope objective is shifted vertically along the optical axis (z-direction), relatively to the fixed focal position and the sample holder is translated laterally (x, y-directions). To avoid the depolarization effect which induces lateral de-shaping of voxels, a quarter wave plate was installed converting linear polarization into circular polarization of the light [68].

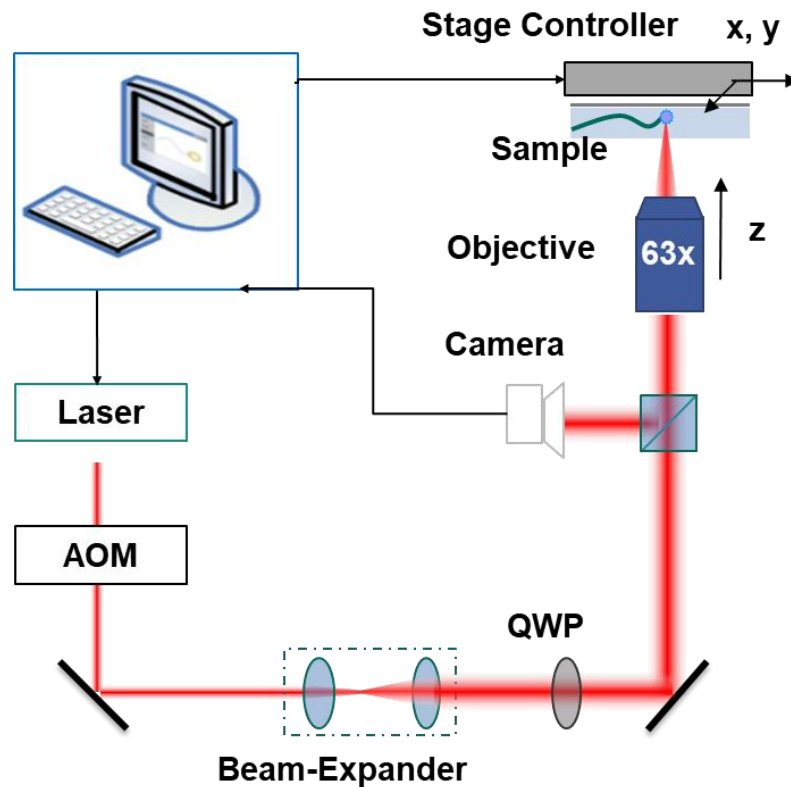


Figure 3.1 Nanoscribe setup

Shorter wavelength will proportionally reduce the diffraction-limit focal spot size. In addition, TPA efficiency is generally large at short wavelengths. However, the use of short wavelength is limited by the availability of laser source and to avoid resin degrading due to monomer or oligomer bond cleavage [69].

Ultrashort pulses and a high repetition rate assure a high peak power and a fast light-matter energy transfer. The numerical aperture is inversely proportional to the beam waist, the Rayleigh range and the working distance. Therefore, a compromise must be found for the objective configuration. The combination of numerical aperture and magnification of the objective guarantees a tight focus while allowing for non-contact writing in a thick layer of photoresist with a working distance of 1.5 mm.

3.2.2 Optical impairments

Optical impairments in two-photon lithography are spherical aberration, defocus, filamentation, self-trapping, self-focusing which influence feature cross section, refractive index contrast, focusing depth. In this work, a correction ring was used to correct the spherical aberration. The defocus factor was calculated to pre-correct it using a computer program for the trajectory coordinates. Numerical aperture of the microscopic lens was chosen carefully to achieve a suitable feature size and aspect ratio.

A higher NA would decrease the voxel height and voxel width, which increases resolution. At the same time, this decreases the working distance of the objective lens, limiting the writing depth of the buried structure [70].

The depth of laser focus inside the resist is calculated by taking into account the aberration correction and diffraction at the air/resist surface (see Figure 3.2). It is crucial to accurately drive the laser focal point along the resist depth due to the thin thickness of the resist. Therefore, one derived the defocus factor (D), namely the shift of the laser focal point due to the refractive index mismatch between air (n_1) and the photoresist (n_2), using Snell's law for marginal rays:

$$D = \frac{OB}{OA} = \frac{tg\alpha}{tg\beta}$$

Using Snell's law:

$$n_1 \cdot \sin \alpha = n_2 \cdot \sin \beta$$

and the numerical aperture (NA) of the microscope objective:

$$NA = n_1 \cdot \sin \alpha$$

D can be written as:

$$D = \frac{\sin \alpha \cdot \cos \beta}{\sin \beta \cdot \cos \alpha} = \frac{n_2 \cdot \sqrt{1 - \frac{NA^2}{n_2^2}}}{n_1 \cdot \sqrt{1 - \frac{NA^2}{n_1^2}}}$$

$$D = \frac{\sqrt{n_2^2 - NA^2}}{\sqrt{n_1^2 - NA^2}} \quad (2)$$

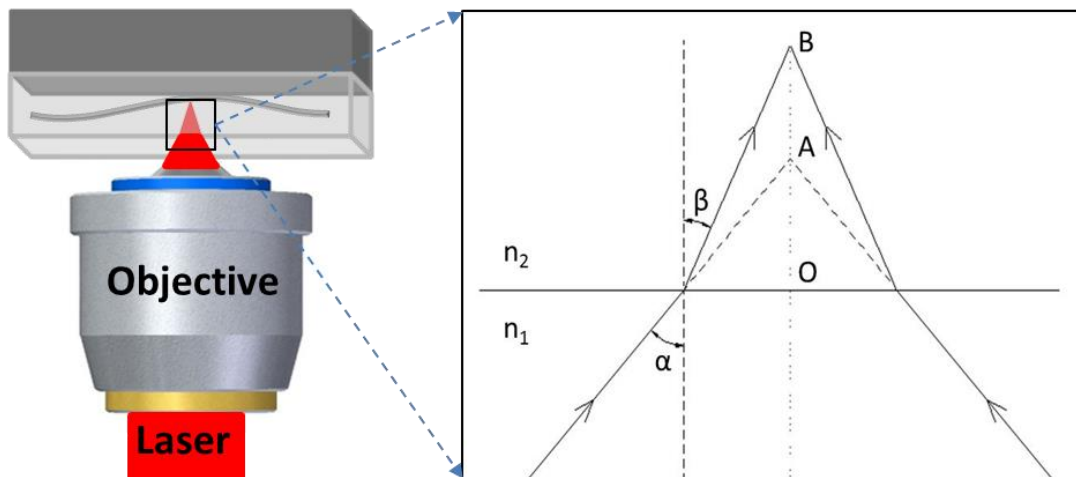


Figure 3.2 How the defocus factor was calculated (combine 2 pics)

Using this equation, the defocus factor of 1.67 calculated for this material is used to correct the z coordinates (optical axis) of the waveguide trajectory. In fabrication, D was adapted empirically.

In literature, this defocus factor was calculated and measured as well by not only using the marginal rays [71–73].

$$\Delta = \frac{f_d}{n} \left(\sqrt{\frac{n^2 - NA^2}{1 - NA^2}} - n \right)$$

3.3 Modification of voxel size

The possibility to manipulate the waveguide feature size is a prerequisite to structure complex devices. Despite the fact that the height of waveguides in traditional photolithography is limited by the thickness of the core layer, 3D laser lithography manages to control both waveguide width and height at the same time. Although multiple sweeping and the distance between single-sweep lines can control the width of the waveguide core, the height of the waveguide core cannot be less than the voxel height. Therefore, one must adjust voxel height in order to modify waveguide core dimensions.

The volumetric pixel (voxel) is the local focus volume where the laser intensity is sufficient for photopolymerization to occur via nonlinear multi-photon absorption. The ellipsoidal voxel has a high aspect ratio of at least 6:1 for this novel photopolymer, which increases with increasing exposure dose.

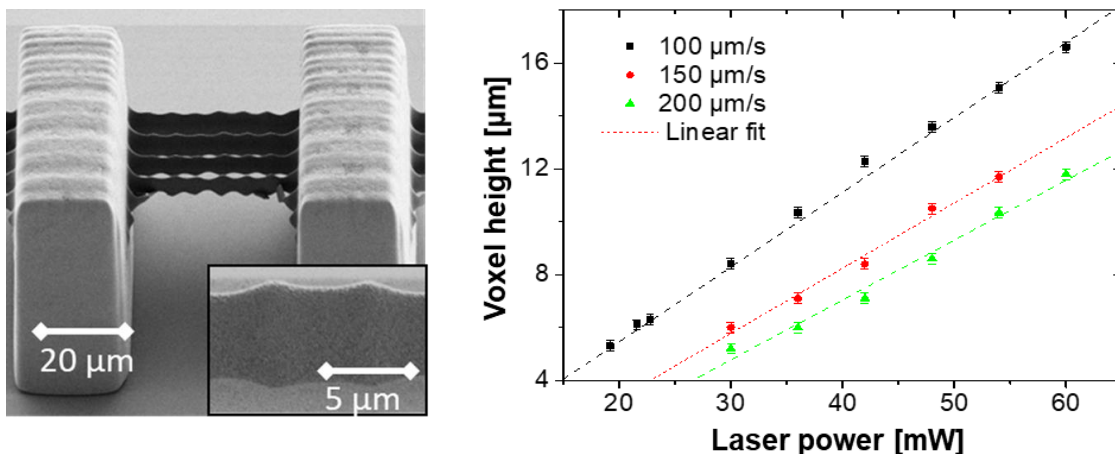


Figure 3.3 (a) Side-view SEM micrograph of single lines after developing the unexposed resist and closer view of the periodic height variation along the writing direction (b) Relation between input laser intensity and voxel height in direct laser writing. Margin of error from the voxel height measurement is $\pm 0.2 \mu\text{m}$. Linear fitting shows the possibility to adjust voxel height by adapting laser intensity at different writing speeds. Higher writing speed results in a smaller core dimension.

Although the number of sweeps and the distance between them can control the width of the waveguide core, the smallest height of the waveguide core is limited by the voxel height. The 3D confinement of two-photon polymerization, the laser power and writing speed define not only the voxel width but also its height. SEM (scanning electron microscope) micrographs helped to determine the voxel heights as shown in Figure 3.3(a). In between two blocks nine single lines at the writing speed of 100 $\mu\text{m/s}$ and increasing laser power from front to back were written. The subsequent development bath removed the unexposed resist to characterize the voxel heights. The first free-standing line from the front reveals the threshold laser power for two-photon polymerization of 18 mW at this writing speed. The further magnified view in Figure 3.3 (a) shows the periodic height modification along the writing path. The maximum roughness amounts to 0.4 μm with a period of 5 μm in the front line. This height variation reduces with increasing laser power as shown in the lines towards the back. This effect is attributed to the combination of the oscillation of the driving piezo and the change of crosslinking degree corresponding to different laser power. The piezo oscillation, whose magnitude was measured to be 0.02 μm , leads to the modulation of scanning speed, varying the exposure doses along the writing direction. In the first line, the laser power is just above the threshold for crosslinking to occur; therefore the laser intensity at the boundaries of the voxel is not sufficient for crosslinking. At the bumps, where degree of crosslinking is higher, the resist is more resistant to developer compared to neighboring regions. Once the laser power is well above the crosslinking threshold (in the back line), the impact of the piezo stage oscillation becomes dominant.

Figure 3.3 (b) plots the measured voxel height according to the writing speeds of 100, 150 and 200 $\mu\text{m/s}$ and the laser intensity from 18 to 60 mW. The voxel height varies from 5 μm to 20 μm . The fitting reveals a linear dependence of laser power and voxel height. A systematic study on the scaling law of voxels in two-photon polymerization has been reported [22], where a nonlinear dependence of voxel

width and height on laser intensity was shown instead. However, when closely investigating these relations, a trend to a linear dependence with high laser power and high repetition rate could be identified, which agrees well with our experimental results.

Two typical spatial beam-shaping methods for femtosecond direct laser writing are using a slit [10] or two cylindrical lenses [11] in front of the objective. We tested the former approach for its simplicity. A slit with a width of 250 μm is inserted closely in front of the microscope objective as depicted in Figure 4.2 (a, b). The slit is oriented parallel to the dominant writing direction (x direction)

A ZEMAX (Optics Studio) simulation was performed in order to compare the Gaussian beam energy distribution at the focal plane without and with the slit as shown in Figure 3.3 (c) and Figure 3.3 (d) respectively. It can be seen that while the transverse width in x-direction is hardly changed, the one in y-direction is significantly increased. The polymerized voxel size is proportional to the square of the laser intensity when the laser intensity is higher than the polymerization threshold. [74] The voxel width in y direction is expected to be roughly doubled according to the simulation. In order to precisely quantize the change of voxel size, straight single-sweep lines were written at the interface between the polymer resist and the silicon wafer. After completing the crosslinking with a thermal treatment, the unexposed volume was developed with the standard developer propylene glycol monomethyl ether acetate (PGMEA). Scanning electron microscope (SEM) pictures revealed a voxel width of 2.32 μm in case of using a slit and a voxel width of 1.17 μm without a slit as shown in Figure 3.3 (e, f).

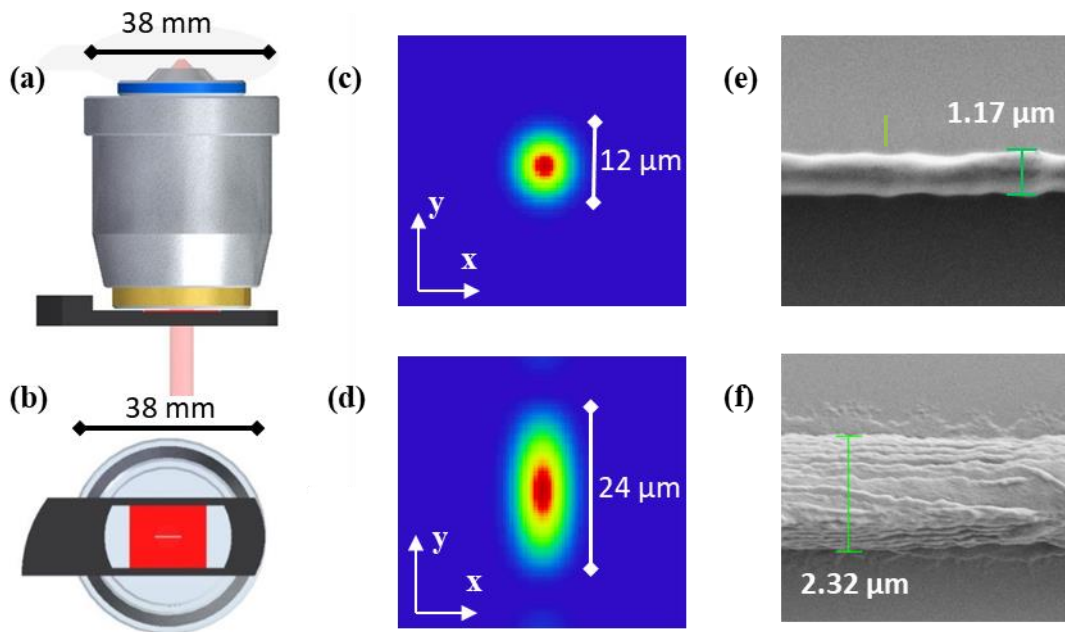


Figure 3.4. Side view (a) and top view (b) of the optical setup with a field aperture placed closely in front of the microscope objective to modify the spatial beam shape in the focus plane. The slit is oriented parallel to the writing direction (x direction). Physical optics propagation (POP) simulation results from ZEMAX show the intensity distribution in false color of the laser beam at focus plane without a slit (c) and with a 250 μm slit (d). SEM picture of a single-sweep written line at the surface of the silicon wafer show a voxel width in transverse y-direction without (e) and with (f) a 250 μm slit; the unexposed volume (the cladding) was totally removed by developing with PGMEA.

The results from SEM pictures are in good agreement with the simulation. A surface roughness of the cross-linked volume was observed near the surface of the silicon substrate as illustrated in Figure 3.4 (f). This is attributed to the $\sim 26\%$ reflection of the laser beam (at 780 nm) when it encounters the refractive index difference between polymer resist and the silicon substrate. This periodic roughness along beam propagation direction (z) has a period of around 200 nm which correlates approximately to a quarter of laser wavelength. However, at a distance further than 20 μm away from this interface, there was no impact of this interface reflection on the surface quality of the written structure.

3.4 Fabrication steps

In this work, we report a novel fabrication technique utilizing external diffusion of a low-index guest monomer into the photopolymer matrix in order to increase the refractive index contrast. Specifically, we demonstrate the manufacturing of symmetric single-mode 3D waveguides with adjustable core dimensions in polymer via two-photon lithography. The fabrication of free form 3D waveguides and waveguide arrays uses a femtosecond laser to expose the waveguides in the resist layer. A monomer external diffusion process is followed by the UV-exposure to stabilize the structure thermally and chemically. The fabrication comprises four basic steps as illustrated in Figure 3.5 : Casting, 3D-DLW followed by thermal treatment, external monomer diffusion, and flood UV exposure with hard bake.

After being spin-coated on a 2-inch silicon wafer, the gel-like polymer was solidified on a hot plate for several hours (Figure 3.5 a). The resist exhibits high adhesion to silicon wafers without adhesion promoter. The proper choice of temperature and time for this soft bake controls the solvent concentration and guarantees a tack-free surface.

Two-photon lithography following a programmed trajectory initiated cross-linking to form the waveguide core. Post exposure bake speeded up the cross-linking in the exposed volume (Figure 3.5 b).

Figure 3.5 c depicts the external diffusion of a gaseous low-index monomer into the uncured cladding in a closed chamber. As proven in proof of concept in Chapter 2, the refractive index of the core remains unaffected during this process. The incorporation of guest monomer ($n_D = 1.445$) into the host oligomer ($n_D = 1.59$) matrix reduces the refractive index of the cladding which yields a high index contrast between the core and the cladding for light guiding. The diffusion depth can be varied by changing the temperature and duration of the diffusion process.

The UV flood exposure at 365 nm crosslinks diffused monomer and host oligomer by means of single-photon absorption. Finally, hard-baking the sample should fully cures the cladding and stabilizes the embedded waveguides (d).

This fabrication process possesses various advantages over other waveguide fabrication methods. It requires only one layer of a single material. Multi layers of waveguides can be inscribed in a single writing step without any stacking or alignment effort. Finally, this rapid prototyping technique no longer involves masks, contact or any wet chemical process steps such as wet etching.

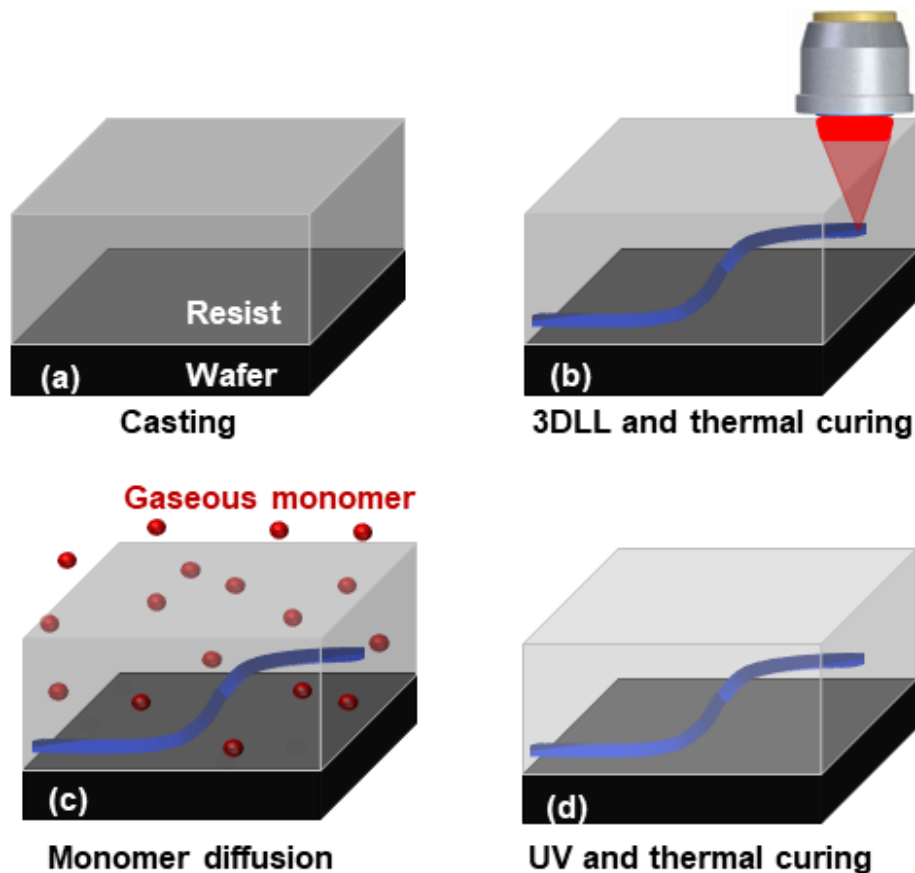


Figure 3.5 Fabrication process

However, several challenges occurred, so that more than 550 samples were necessary to cope with these issues. Frequently structures collapsed or peeled off from the substrate. Furthermore, the correct exposure doses had to be found in order to achieve the structure dimensions accurately. Additionally, the enormous amount of filigree structures (> 15,000) that had to be individually written by the laser increased the processing time beyond 50 hours. During this work, samples

used to compare different fabrication parameters at a certain time will be called identical samples. They are samples from the same batch and went through the same fabrication flow from the oligomer mixing until the testing step.

In the following, detailed description of each fabrication step, discovered challenges and the final solution are reported.

3.4.1 Spin coating

We found that the adhesion of the waveguide material is much less to glass wafers compared to silicon wafers. Usually the layers peeled off after dicing or 3-4 weeks after preparation. Even adhesion promoters plus surface processing (e.g. reactive ion etching RIE) did not prevent peel off. It is known that the peel strength of resist material to glass substrates can however be increased by a factor of 3.5 using interlocking features [75]. However, we opted to use silicon wafers as a substrate due to high adhesion and the fact that higher index contrast to polymer helps to find the right interface (e.g. polymer/silicon) easier via infinite focus. The down side is higher reflection close to the wafer (less than 20 μm), which can be avoided.

Spin coating of the photopolymer on a silicon wafer with the rotation speed of 500 - 5000 rpm (round per minute) enabled the generation of defect-free layers with thicknesses ranging from 20 μm up to more than 250 μm .

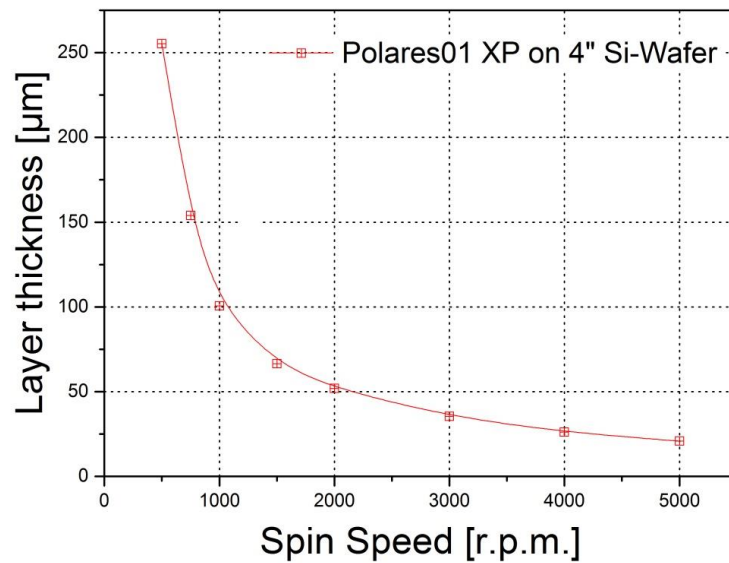


Figure 3.6 Spin curve of the host oligomer

Layers with a thickness higher than 400 µm were produced in a modified coating process. By this spin-free process, bubble-free layers (thickness > 400 µm) with a thickness variance of $\pm 5\%$ were achieved in combination with longer relaxation times after coating and a step-by-step prebake temperature program

3.4.2 Prebake process

The requirement for prebake process is a tack-free surface of the resist with satisfactory flatness, homogeneous and no bubbles. Prebake process adjusted solvent concentration from 5.3 % to 9% weight for the thickness of 100 µm to 400 µm resulting in a tack-free film layer. The weight proportions were measured by gravimetric method. Furthermore, this solvent concentration ensured sufficient mobility for external monomer diffusion for refractive index tuning between written waveguide cores and surrounding cladding material.

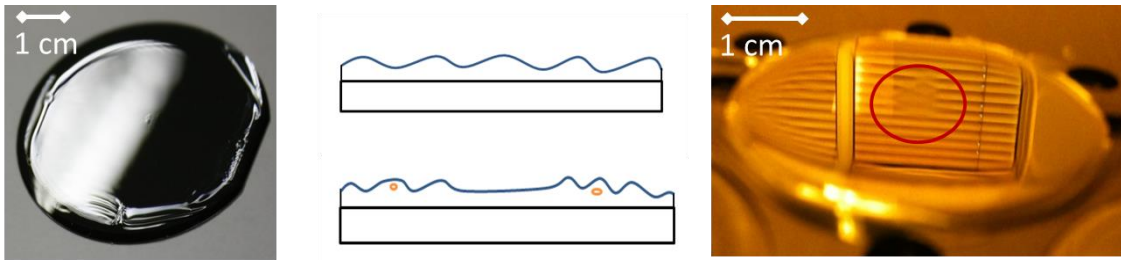


Figure 3.7 Second prebake at 55° for 1 hour could remove striations and wrinkles.

Striations are radically oriented lines of thickness variation in the as-coated film. Their occurrence is attributed to the evaporation driven surface tension effects. Our solution was to apply second prebake at 55 °C for 1 hour to remove the striations and wrinkles completely.

3.4.3 Waveguide writing

Waveguide writing defined all free-form structures in a single step with a commercial 3D laser lithography system, avoiding any alignment or stacking between layers. High peak power and short transition time of the femtosecond laser initiated two-photon absorption for 3D confinement of photo-polymerization. Moving the sample with respect to the laser beam in a computer-programmed path inscribed free-form waveguide cores.

Process parameters

The laser power and writing speed were adapted according to material photosensitivity and refractive index modulation. The writing speed varies from 0.1 mm/s to 1 mm/s, and the input average laser power ranges from 5 mW to 40 mW producing different doses for the crosslinking process. Number of sweeps, i.e. intact writings, and distance between each sweep define the waveguide core shapes, leading to symmetrical guiding mode fields. The written patterns need to induce a permanent refractive index profiles so that to avoid further photo curing or thermal curing. Another equally important target at this step is to minimize surface roughness, namely the modulation of waveguide dimensions along the written structure.

Experiments

Using the Photonic Professional system (Nanoscribe GmbH [67]), 2-inch and 4-inch samples on Silicon wafers were written in clean room environment and subsequently characterized with microscopic or SEM photos.

First definite focus was used to find wafer/resist interface at different points (> 5x5 grid points). Interpolation and fitting from these points determined the wafer surface and correct the wafer/resist tilt. The structures were written from wafer to air surface. For complicated structures, the writing sequence was built so that no written-patterns blocked the others. The laser powers at acceleration part and deceleration part were empirically adapted to the writing speed. However, the best uniformity was achieved by dicing these parts off.

Writing speed is the combined velocities of motor driving stage which moves the sample holder and the piezo controller which translates the microscope objective in z axis (optical path). Highest laser pulse power creating local explosions formed the markers in the resist layer. Point distance, which is the distance between the trajectory points, was tested to minimize sharp curves and writing speed variation along the trajectory.

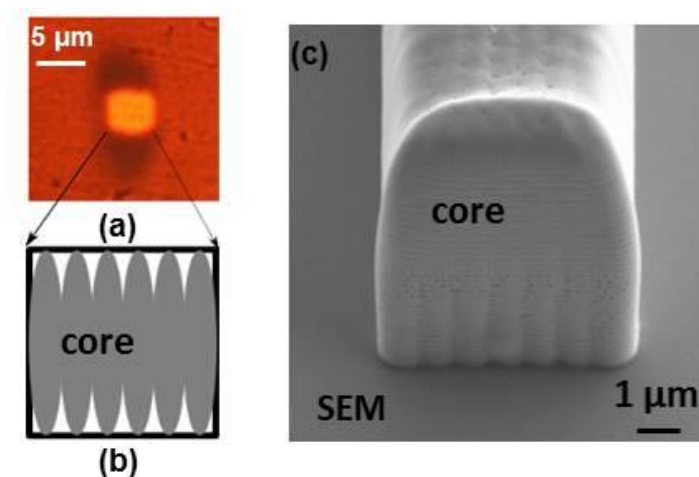


Figure 3.8 (a) Microscope picture of the end facet of a waveguide (b) schematic of multi-sweeping (c) SEM pictures of a waveguide core with multi-sweeping.

Owing to a high aspect ratio of the voxel, we exploited the multiple-sweeping, specifically the parallel writing of several in-contact lines, to fabricate a symmetric waveguide as depicted in Figure 3.8. The smooth surface shown in Figure 3.8 (a,c) is attributed to the proximity effect which rounds out the gap between the inline voxels. In this SEM (scanning electron microscope) image, the cladding was not cured but rather developed by wet etching to reveal the waveguide core surfaces.

Issues

Major challenges in this step are structural uniformity, controller vibration, and local explosions along the trajectory.

Hybrid stage controller versus non-hybrid controller: Two writing controller setups of hybrid mode and motor mode were tested for our applications. The hybrid mode combines the motor stage controller and piezo controller to drive the sample laterally (in x and y). The stage translated the programmed trajectory while the piezo constantly trace the real time movement and correct it to the designed trajectory. This mode assured high positional precision. However, constant adaptation of the translating coordinate while writing at a high speed of beyond $50\mu\text{m/s}$ caused two problems.

The first problem is the oscillation of the piezo controller. Hybrid mode only allowed low speed writing in the range of $20 - 50 \mu\text{m/s}$, which is not suitable for centimeter long waveguides. Correction using acceleration and power adaption did not improve the dose homogeneity. In addition to the writing precision, the piezo controller oscillation contributed to the modulation of core dimensions along the writing trajectory. This effect will be discussed in details in the next chapter.

The second issue is the calculating power required of the machine at high writing speed for the close-loop tracing and correction. This is a critical issue since the system crashed and interrupted the writing process. The supplier could not solve this issue, leading to the selection of the option 2 – the motor stage mode.

As opposed to the hybrid mode, the stage mode used only a DC motor controller to drive the sample holder laterally (in x and y). Its positional precision is an order of magnitude less than the piezo controller is, but the writing discontinuance was avoided.

Stop and go: Since board-level waveguides are centimeter long, scanning layer after layer to build the 3D structure as in typical 3D printing requires stitching and is time consuming. With a lateral scanning field of $300\ \mu\text{m} \times 300\ \mu\text{m}$ in the piezo controller mode or $150\ \mu\text{m} \times 150\ \mu\text{m}$ in pivoted galvo mirrors mode, at least 9 stitches would be needed to complete waveguide structure. This leads to mode field mismatch and hence transmission loss. In addition, the exposed volume is at least 3 orders of magnitude smaller compared to unexposed volume. Hence, avoiding layer scanning reduced the passive writing time (stage moving while laser is off) significantly.

The waveguide were written by connecting the coordinates following a certain trajectory as shown in Figure 3.9. Symmetrical waveguide core were formed by sweeping the laser spot to connect the coordinate points along a programmed trajectory (a). The connection points are visible along the written structure in case of parallel sweeping (b). Lower writing speed induced a higher dose at the connection points, forming a larger cross-linking volume there.

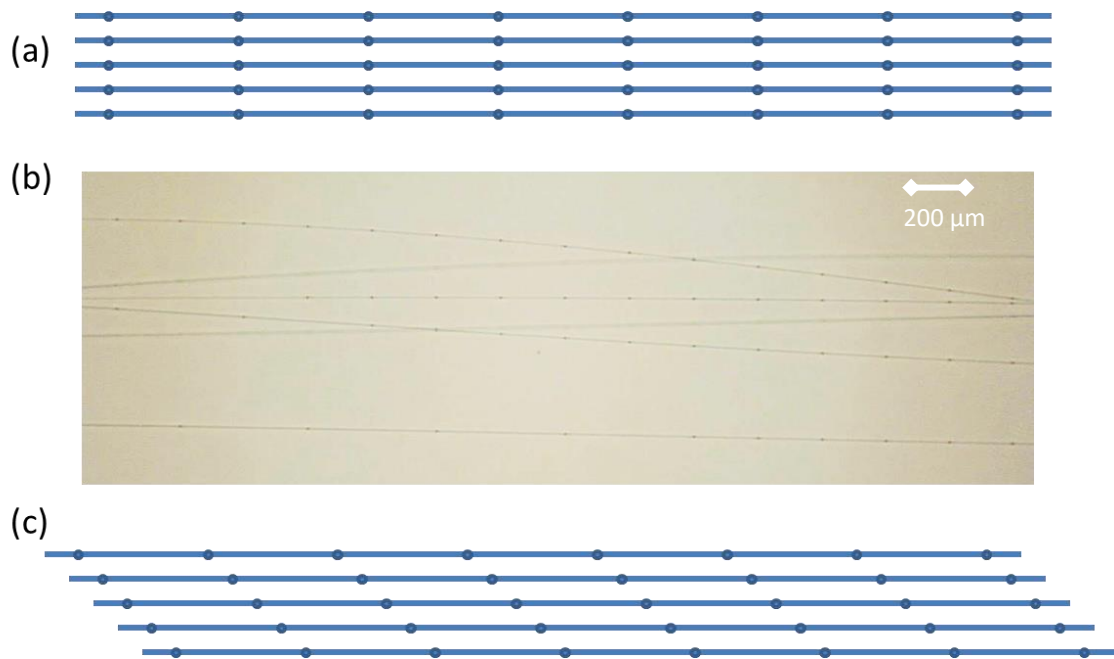


Figure 3.9 Stop and go issues at connection points in writing trajectory (a) schematic of parallel sweeping where connection points were in line at the same z- coordinates (b) lower writing speed caused a higher dose at the connection points (c) by shifting the sweeping lines one after the other, these connections are no longer visible

This periodical increase of the waveguide core will raise the transmission loss and deteriorate the guiding modes. To tackle this effect, the coordinates of connection points were shifted among the sweeping lines. As a consequence, the connection points were no longer visible. The offsets were optimized using microscopic analysis and transmission loss.

3.4.4 Post exposure bake

The mobility of photo-acids generated by two-photon absorption at room temperature is low. Therefore, an extra thermal processing is required to increase the interaction possibility of photoacids and oligomers. Heating up the sample boosts the reaction kinetic of the cross-linking mechanism by increasing the molecular motion and hence accelerates the crosslinking process [76]. The fast polymerization during the post exposure baking (PEB) limits photoacid diffusion into non-exposed areas because of entrapment of the catalytic protons. This so-called cage effect ensures the high resolution of the SU-8 structures. At the same time, polymerization slows down during the PEB due to a decrease in the

concentration of the unreacted epoxy groups and decreased mobility of the monomers as a consequence of the increasing cage effect [60].

Process parameters

Parameters to be determined in this step is baking temperature, baking time, cooling times and number of baking steps. An optimized recipe should minimize inner stress; assure proper crosslinking rate and suitable refractive index profile.

Experiments

Samples were baked to a temperature higher than room temperature on hot plates or in an oven following several steps. The cooling down step gradually turned the samples back to room temperature. The number of steps and the waiting time at each step depend on the temperature and sometimes sample's thickness.

In our work, baking in hot plates was proved much faster relative to baking in ovens. More importantly, hot plates provided better surface quality, homogeneity and structural stability.

Issues

Typical issues in photolithography during this step are peel-off and wafer deformation due to haste heating or cooling. By increasing number of steps or extend the waiting time, the ramping time the peel-off and deformation could be easily avoided. More critical issues occurred in our work is structure instability.

Impact of PEB parameters on instability: Immediately after laser writing, the samples were baked to different temperature following the table below:

Table 3.1. fabrication flow of post exposure baking

Temp. 1	Waiting time	Temp 2	Waiting time	Temp 3	Waiting time	Cooling down to RT
40	5'	60	5'	80	10'	4h

The up ramping time followed the rule of thumb of 1.5 minutes for 1 degree. For instance, the hot plate took 30 minutes to heat the sample from 40 °C to 60 °C. This recipe was used to different steps of baking from 50 °C to 70 °C as illustrated in the pictures below.

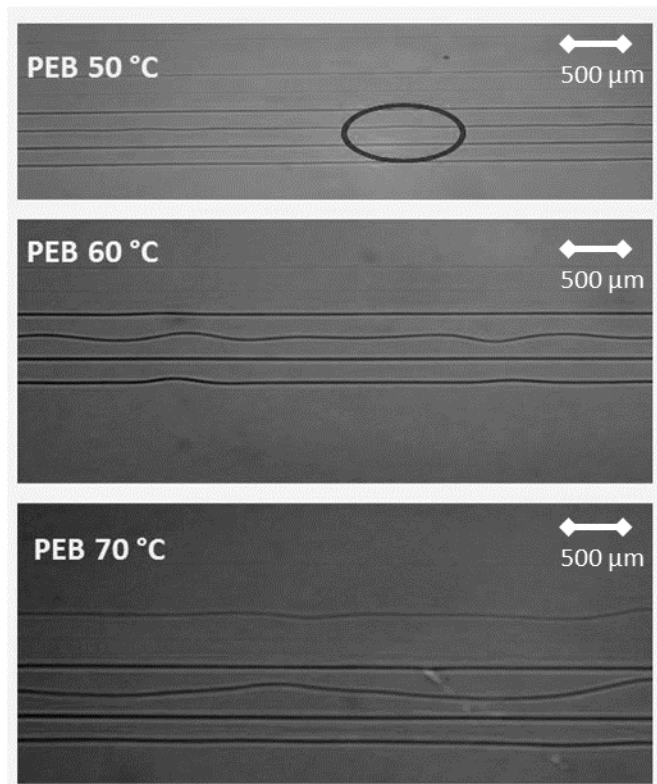


Figure 3.10 Impact of post exposure baking temperature on stability of inscribed structures. 410- μ m thick samples were baked to temperatures between 50 °C and 70 °C, differing in shifting and bends.

Baking the samples at various temperatures indicated the impact of post exposure baking temperature on structural stability. In Figure 3.10 one sample is shown at different temperatures during the increase of the baking temperatures. The pictures after each step revealed the increasing drifting and bends of the

waveguides with higher baking temperatures. At 50 °C, the waveguides are still straight and equidistant, though some random micro bends can be observed. At 60 °C the bends are more visible and the drifting of the waveguides out of their original positions start to appear. At 80 °C the waveguides start to tangle and their elongation is clearly seeable.

Heating four identical samples independently to these temperatures showed similar results. Extending the cooling time and the number of cooling steps did not improve the structural stability.

3.4.5 External diffusion

After the PEB, waveguide cores were buried in the resist layer. However, the core-cladding index contrast does not suffice for effective light guiding. Hence, a guest monomer with lower refractive index relative to the cladding needs to enter the oligomer matrix to reduce its index of refraction. Additional requirements are profile homogeneity, acceptable diffusion rate and permanent induced index contrast.

Process parameters

Once a suitable monomer was selected in the proof-of-concept tests, diffusion process parameters to be determined are diffusion temperature, pressure and duration. Diffusion occurs as the movement of particles from a region of high concentration to a region of low concentration. Here, the rate of a randomly moving gaseous monomer replacing a vacancy in a solid resist can be expected to be extremely low. Hence, keeping diffusion duration acceptable is a challenge for the resist thickness up to 1 mm.

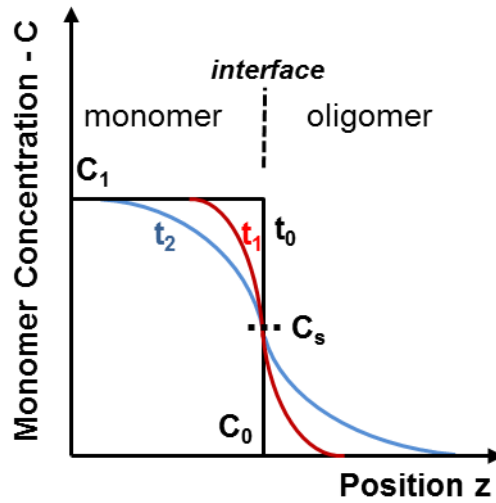


Figure 3.11 Concentration profile of monomer at the gaseous monomer and solid oligomer interface

Fick's first law explains that the net flow of atoms is proportional to the negative of the concentration gradient:

$$J = -D \frac{dC}{dz}$$

Where J is the flux of atoms [$\text{atoms} \cdot \text{m}^{-2} \cdot \text{s}^{-1}$] indicating the number of atoms passing through a unit area in a unit of time. D is diffusivity or diffusion coefficient [$\text{m}^2 \cdot \text{s}^{-1}$] and C is the concentration [$\text{atoms} \cdot \text{m}^{-3}$]. The diffusion coefficient depends on size and shape of the monomer molecule, interaction with the oligomer and its viscosity.

The corresponding diffusion equation (Fick's second law) for 1D case is:

$$\frac{dC(z, t)}{dt} = -D \frac{d^2C}{dz^2}$$

The rate of compositional change is equal to the diffusivity times the rate of the change of the concentration gradient. In this case, a solution can be derived:

$$\frac{C(z, t) - C_0}{C_s - C_0} = 1 - \text{erf} \left[\frac{z}{2\sqrt{Dt}} \right]$$

The derivation from Fick's law is:

$$z_i \sim (D \cdot t_i)^\gamma$$

which calculates the diffusion depth z_i as a function of diffusion time t_i , where D is the diffusion coefficient and γ is 0.5. One of the aims of our experiments explained in next section is to verify and increase this γ for higher diffusion efficiency.

Experiments

The diffusion experiments were carried out with a gaseous monomer (monofunctional oxetane derivative, $n_D = 1.4346$). An externally heatable pressure filter with space for three wafers and a diameter of 2 inches was used as a diffusion chamber at mrt. The diameter is approximately 12.5 cm (space for 4 Si wafers). The wafers lie on a screen, which is about 0.3 cm above the surface of the glass beads with monomers. The total height of the chamber is about 2.5 cm. In comparison, a chemical reactor was counter-tested at KIT. The chamber is larger, directly heatable using water flow and additionally allows a pressure setting, which allows the control of further process parameters.

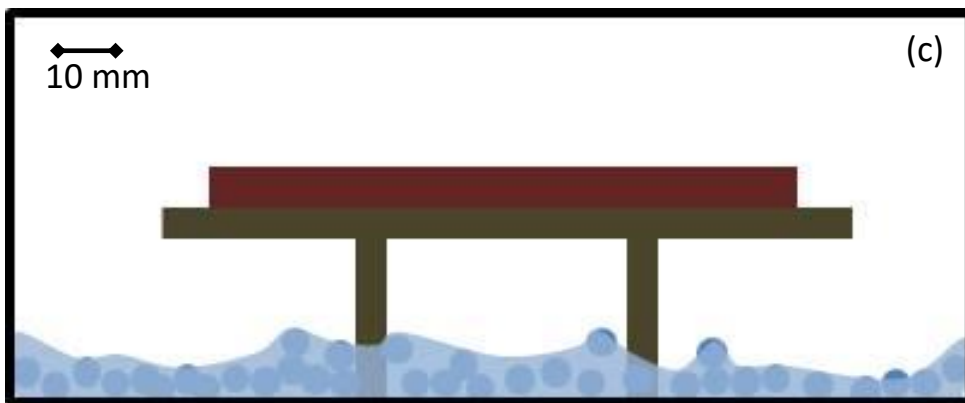
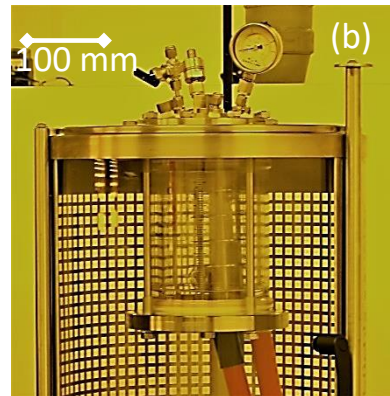
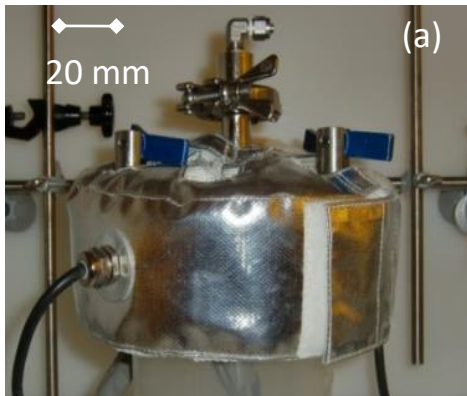


**Figure 3.12 (a) Diffusion chamber at mrt; (b) Diffusion chamber Ecoklav at KIT;
(c) Diffusion setup scheme**

The diffusion chamber is a 2-liter glass vessel. Glass balls and approximately 100 ml of liquid monomer were added at the bottom of the chamber. The function of glass balls with average diameter of 1.5 mm was to increase the evaporation surface of the monomer. Three samples were placed one above the other on a sample holder. For the diffusion carried out at 70 ° C, the pressure was measured to be about 0.1 - 0.2 bar during diffusion. Only the bottom wafer showed high diffusion depth. The upper wafers reached only less than 10 microns. One explanation would be that the concentration of monomer in the atmosphere far away from the monomer surface is too low.

Issues

At this point, the bends and drifting after PEB were eliminated. However, major issues occurred in this diffusion process are still structure instability (i.e. bends and drifting of the patterned waveguide cores), elongation and swelling. As a starting point, samples with thicknesses of approximately 400 μm were used to test the diffusion process.

Bends and drifting: Before going through the diffusion step, all the samples were assured that the structural stability is maintained using microscopic photos and measurements. As plotted in Figure 3.18, for the samples of 400- μm thickness, a diffusion time of 72 hours at 70 $^{\circ}\text{C}$ was required to reach a sufficient diffusion depth. As shown in Figure 3.13, straight waveguides with a pitch size of 200 μm and a length of 3 cm were written in layers of 50- μm apart. After the diffusion, the strong bends and drifting were severe, in particular with the waveguides written closer to the air surface, which twisted together. This effect was named *Hair Swimming in the Soup*, or HaSS in short. The honey-like surface of the resist during and after diffusion also accounts for this name. Similar to bends and drifting during PEB, the degree of HaSS also reduced with lower diffusion temperature and with lower diffusion time.

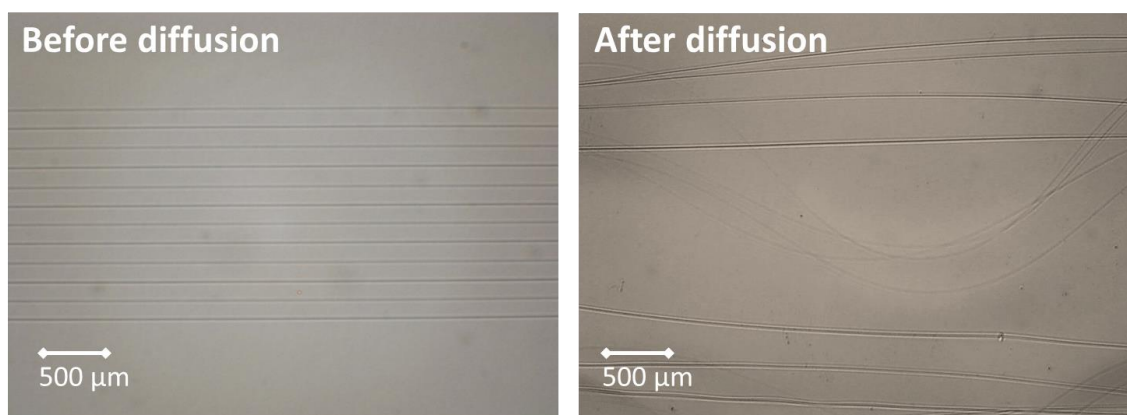


Figure 3.13 The so-called hair in the soup (HaSS) effect: top views of waveguides before and after external diffusion at 70 $^{\circ}\text{C}$ for 72 hours. The sample was 400 μm thick and the waveguide core dimensions are larger than 6 μm .

To have further details of this HaSS effect, some samples were completely cross-linked and diced for the end facet views. From the back-illuminated microscopic photos in Figure 3.14, the waveguide cores appeared to rotate and drift in all possible directions.

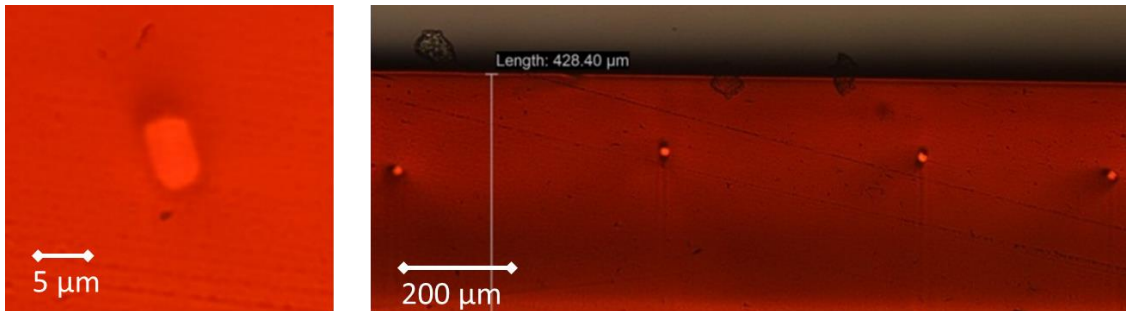


Figure 3.14 Rotation of the core and the moving of the waveguide cores which are supposed to be inline

All these rotation, bends, drifting were random. There was no systematic pattern of these effects. An assumption to explain HaSS effect is the combination of the inner stress produced by thermal treatments and the softening of the resist during the diffusion process. Since the resist was honey-like during this process, its free flowing, in particularly at temperature when the local temperature at different portions of the wafer could be different, could also play a role in making HaSS so randomly.

Elongation: Figure 3.15 plots the schematic of the elongation of the written waveguides during the diffusion process. The waveguide length was extended relative to the design value. The core dimensions of the waveguides were measured to be in the range of $5 \pm 0.5 \mu\text{m}$. That means the waveguide cores grew in volume during the diffusion process.

One possible explanation is that the core material was flexible due to incomplete cross-linking, and thanks to the softening of the cladding matrix plus the inner stress, was stretched and elongated. Furthermore, there seems to be the continuation of the cross-linking. Doing PEB at $40 \text{ }^\circ\text{C}$, far below the T_g of $55 \text{ }^\circ\text{C}$ solidify this assumption.

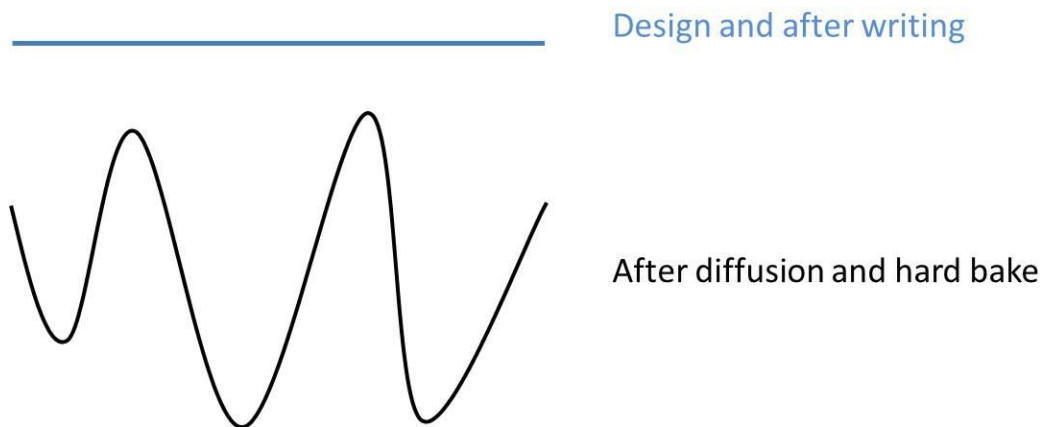


Figure 3.15 Elongation of the written waveguide during the diffusion process.

However, a further question remains. Is this continuation a reason for HaSS? To clarify this point, T-shaped markers were written at the resist surface with over dose. The local burns/explosions along the markers assured no possible continuation of the cross-linking. The free flowing marker in Figure 3.16 confirmed that the cross linking continuation did not contribute to HaSS.

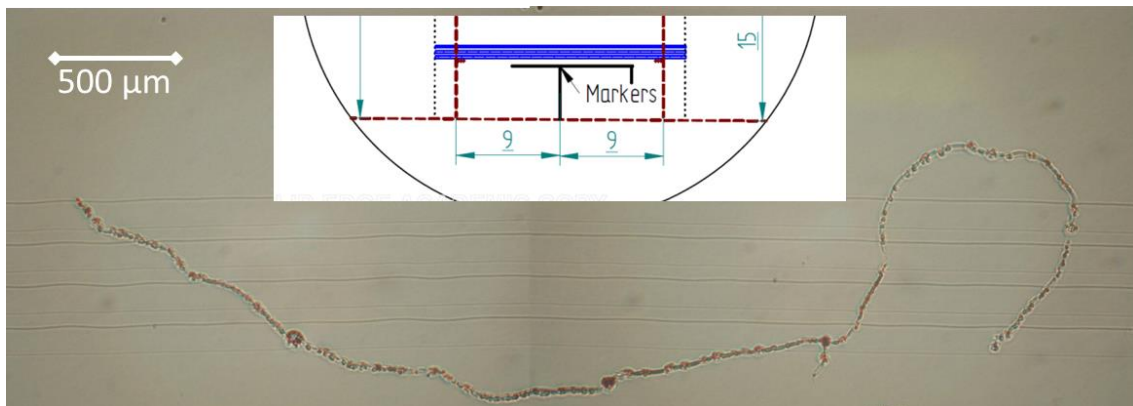


Figure 3.16 The free flowing of over-exposed markers eliminates the possibility of the polymerization continuation causing the bends and drifting. The markers were written at the top surface of the resist which worsens the HaSS

The elongation of the marker was not detectable owing to the material hardening of the burns/ explosions. On the other hand, with waveguide cores written close to the wafer, i.e. up to 30 μm above the wafer, the HaSS was not observable. There

was no elongation either. This observation asserted the critical role of inner stress and material softening in the HaSS effect.

Swelling: Diffusion of polymer was previously utilized to fabricate waveguides where monomer was first diffused into and subsequently removed from the polymer [77]. In the developed process, the removing step is not necessary, but the swelling changed the depth of the written waveguides. Hence, the swelling needs to be quantified and pre-corrected.

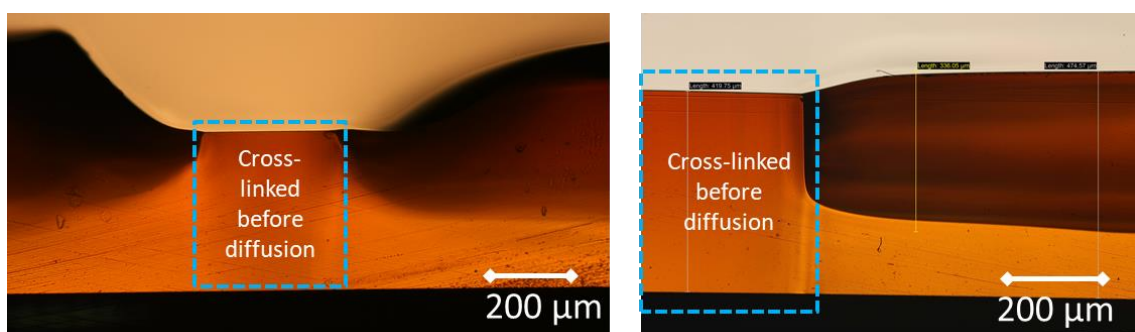


Figure 3.17 Swelling in the diffused region compared to cured region. The region cured before diffusion did not swell since there is no diffusion.

Figure 3.17 shows the thickness growth of the diffused region. The cured region, where no diffusion occurred, was used as a reference to quantify the swelling. Subfigure (a) shows a swelling of 39 % with 122 h diffusion at 60 °C while the swelling in subfigure (b) is 13 % with 60 h diffusion at 60 °C.

Solutions: The derivation from Fick's law $x_i \sim (D \cdot t_i)^\gamma$ calculates the diffusion depth x_i as a function of diffusion time t_i , where D is the diffusion coefficient and γ is 0.5. Diffusion rate of a monomer into a solid oligomer matrix can be expected to be significantly low. In our experiments, we kept the liquid monomer inside the diffusion chamber. Consequently, the liquid monomer constantly evaporated gaseous monomer during the diffusion process. Figure 3.18 illustrates diffusion depth as a function of time and temperature in this case. The diffusion rate increases with increasing temperature. For instance, γ increases to 0.69 at room temperature and to 0.86 at 70 °C. Diffusion depth of 400 μm was achieved with 72 h diffusion at 70 °C using samples of 800 μm thickness.

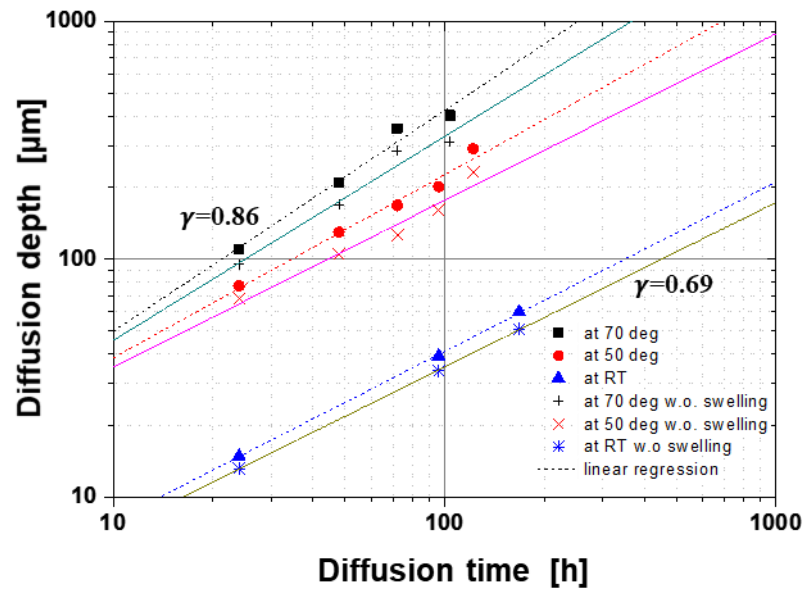


Figure 3.18 Diffusion depth as a function of diffusion time and temperatures with swelling (dotted lines) and after subtracting swelling (continuous lines)

Comparing the thickness of diffused photopolymer and non-diffused photopolymer layer derives the swelling factor of the photopolymer at different temperatures. The linear regression helps design the pitch size and layer thickness.

Figure 3.19 shows the vertical index variation along the diffusion depth at different diffusion conditions beside the core structures. The refractive index increment from surface to bottom of the fabricated photopolymer layers (125 μm thick) after diffusion is 0.0074 that is half of the core-cladding index contrast. However, this variation surrounding a waveguide core is 5-fold reduced which explains the symmetrical guiding mode field. Considering the 25- μm pitch between waveguide layers, the higher RI contrast between waveguide core and cladding towards the top layer only changed the mode field diameter by 1.6 %, which was analyzed by beam propagation method (BPM, BeamPROP™).

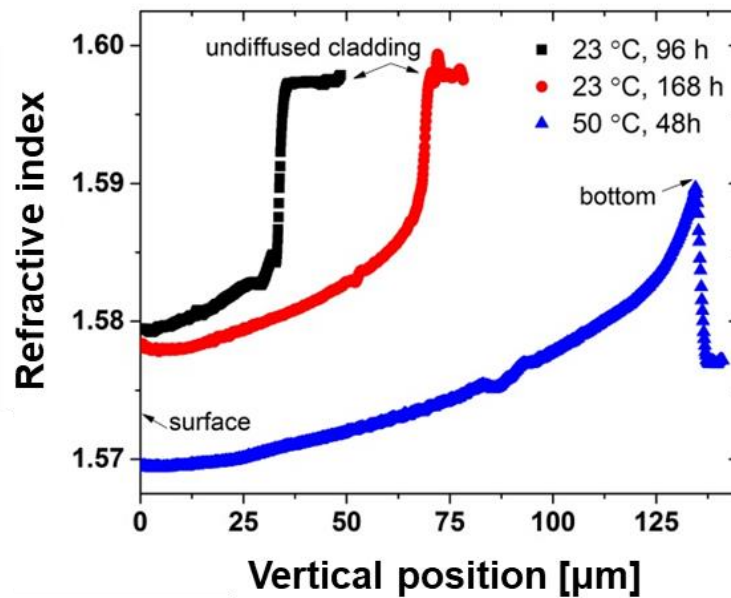


Figure 3.19 Vertical distribution of refractive index for waveguide cores and cladding measured by refracted near field method

Due to the tradeoff between diffusion depth and structural stability, a functional resist layer thicker than 100 microns could not be achieved without significant bends and drifting. Restraining the diffusion temperature to room temperature (23 °C), assured structure instability. At this low temperature, the inner stress was minimized. However, the softening of the resist increased with longer diffusion time. The diffusion at ambient temperature was thus limited to 7 days.

3.4.6 Flood exposure and hard bake

The aim of these final fabrication steps is to stabilize the whole resist layer. On other words, flood exposure and hard bake need to induce the refractive index contrast permanently. The homogeneity of the refractive index also needs to be considered here. Since a thermal process is involved, surface quality and wafer deformation are also indicators for a suitable recipe.

Process parameters and experiments

Appropriate flood exposure dose at 365 nm should be tested to avoid over or under exposure. Baking time and temperature defines the hard bake process.

Because these parameters are tightly related, they are addressed and optimized together.

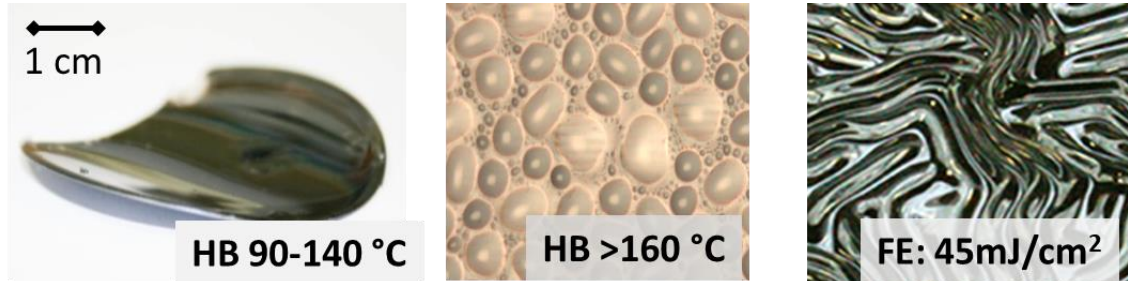


Figure 3.20 From left to right: wafer deformation due to over baking; surface bubbles due to over baking; furrows due to under exposure

Figure 3.20 illustrates the impact of exposure dose and hard bake temperature. Hard-baking temperatures directly to over 90 °C produced wafer deformation. This is due to the difference of thermal extension coefficients between polymer and Silicon. Surface bubbles were observed when the hard bakes were done at 160 °C or higher. Since this did not happen with lower monomer concentration at the resist surface, it was attributed to the residual monomer on the resist surface. Acetone treatment could remove the bubbles and return a smooth surface of the resist. Table 3.2 reveals the hard bake tests with different scenarios.

Table 3.2 Wafer deformation according to different hard bakes

Solvent concentration %	Dose mJ/cm ²	HB °C (Hard bake)	○ Deformation ● No Deformation
12.30	350	RT-140 °C 20 min	○
11.80	350	RT-120°C 20 min	○
11.80	350	RT-120°C 20 min	○
5.00	350	RT-80 °C 10 min	○
2.00	350	RT-80 °C 10 min	○
7.40	200	RT-80 °C 10 min	○
5.00	200	RT-50 °C 10 min	●
7.37	300	RT-50 °C 15 min	●
7.48	3000	RT-50 °C 15 min	●
5,00	2500	No hard bake	●

Extreme under-exposure, e.g. 10 % of the dose, produced burrows at the resist surface. Because this dose is only sufficient to cross link a small portion of the top surface, the difference in the physical properties of the cross-linked top layer and uncross-linked bottom layer created surface tension and hence the burrows. Utmost overexposure, e.g. 10 fold of the dose, turned the resist yellow. However, even this high dose could not cross link the resist by itself. Without a subsequent hard bake, the resist could be dissolved in the developer. This experiment proved the essential of hard bake. On the other hand, with hard baking at high temperatures ($> 140\text{ }^{\circ}\text{C}$), even without exposure to light (no flood exposure), the PAG starts to decompose and subsequently thermal cure happens.

Therefore, **flood exposure** at 365 nm with the dose of 0.5 J/cm^2 and a hard bake at $140\text{ }^{\circ}\text{C}$ proved to be the optimum parameters. To avoid wafer deformation during the following hard bake, samples were gradually cooled down to room temperature from $50\text{ }^{\circ}\text{C}$ before heating up again to $140\text{ }^{\circ}\text{C}$.

Shadowing: Waveguide cores behave as a lens for the UV light during the flood exposure due to their gradient index near the core border. It explains the focusing shadows below each waveguide core described in Figure 3.21. This interpretation was again confirmed by the tilting of the shadows following flood exposure coming at different angles.

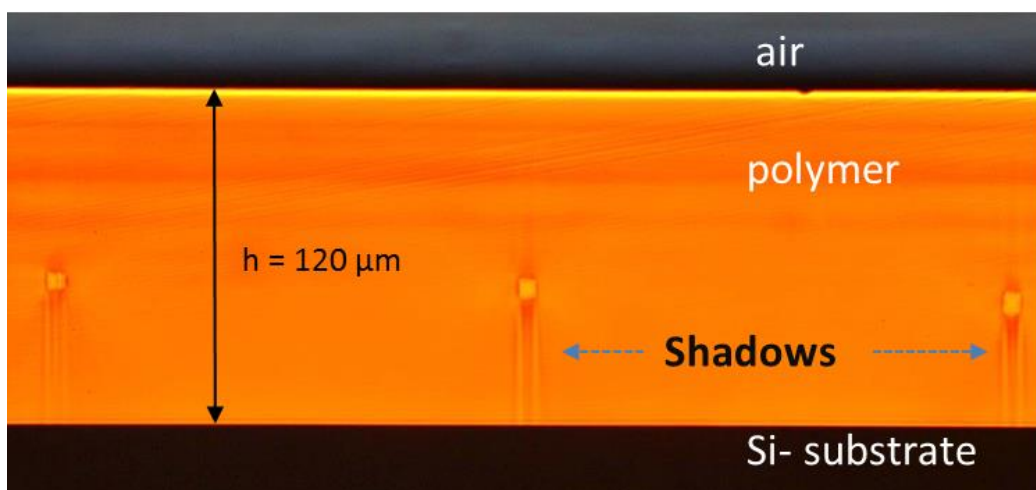


Figure 3.21 Shadowing effect below the written waveguides at two different exposure angles

The shadowing was minimized by performing the flood exposure at discrete steps at different tilt angles of the samples, e.g. exposing the samples at tilt angles of -10° , 10° and 0° with 170 mJ/cm^2 dose each time.

We employed differential scanning calorimetry (DSC) to analyze physical properties of the photopolymer such as softening and curing completeness. The results served to optimize the fabrication process. The DSC method measures quantitative heat flow into or from a sample as a direct function of time or of the reference temperature. The resist layers were removed from the substrate using a razor blade. Figure 3.22 plots the DSC measurement of the photopolymer before and after diffusion. The diffusion occurred at room temperature for 168 h, prior to flood exposure at 365 nm wavelength and hard bake. At a high enough temperature, the resin underwent curing represented by a large exothermic peak. The beginning and the completion of the cure process are the temperatures at which the heat flow deviates from and return to a linear response respectively. The green curve in Figure 3.22 (3) describes the first heating cycle of the uncross-linked host oligomers after the pre-bake. The relaxation area appears in the temperature range of $50^\circ\text{C} - 90^\circ\text{C}$. The peak related to the curing disappears in the subsequent second heating cycle (blue curve - 4), indicating the curing completeness at temperatures above 150°C . The black curve shows the heat curve of the host-guest system after external diffusion of the monomer (168 hours at room temperature). In this case, the curing region widens to a temperature range of $40^\circ\text{C} - 110^\circ\text{C}$. The repeated heating cycle also confirms no further curing at least above 150°C .

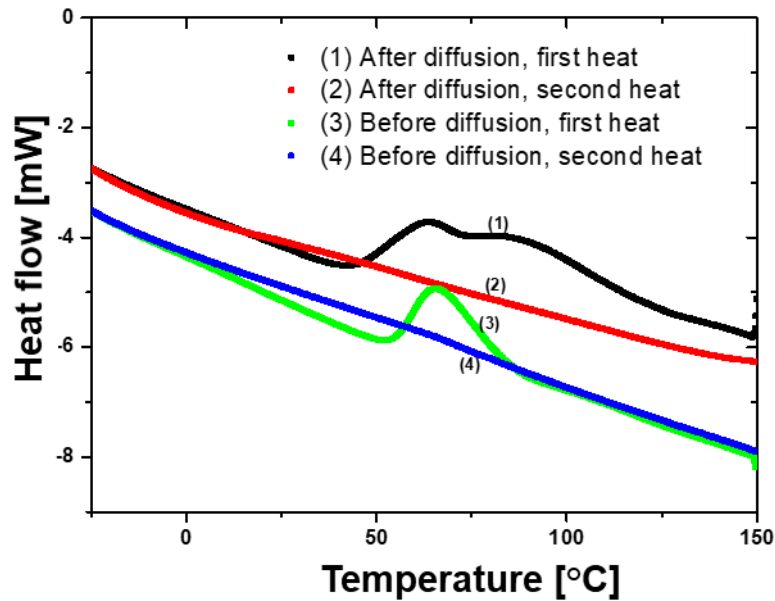


Figure 3.22. DSC measurement for analyzing curing and softening process of the photopolymer before and after diffusion: The samples were heated up from -20 °C to 150 °C at a constant heating rate of 10 °C/min; Diffusion of monomer broadens the exothermic peak from both sides of the temperature range.

Interestingly, the starting temperature of the curing increased with higher temperatures in a previously performed hard bake. This held for both materials pre- and post-diffusion. For instance, hard baking the post-diffusion sample at 100 °C for 10 minutes raised the beginning temperature of the curing process to 65 °C (instead of 40 °C) at the next heating cycle.

3.4.7 Conclusion

There exist several relations between the fabrication steps. The production of layers with a thickness higher than 400 μm was achieved in a modified coating process. This spin-free process, in combination with longer relaxation times after coating and a progressive prebake temperature program provided bubble-free layers with a thickness variance of $\pm 5\%$. Samples experiencing a temperature higher than 120 °C prior to diffusion hardly allowed the monomer diffusion. Similarly, even a small UV dose of 5mJ/cm² (1 % of full dose) prevented following external monomer diffusion. This is attributed to the curing and hardening of the photopolymer layer prior to diffusion. At high temperatures (≥ 140 °C), even

without exposure to light, the PAG starts to decompose and subsequently thermal cure happens. Interestingly, omitting PEB after laser writing reduced the minimal waveguide core dimensions to half since the monomer could penetrate into the uncompleted cross-linked volume.

To maintain the structural stability, PEB was kept at 40 °C and diffusion was carried out at room temperature. The final recipe is shown in the table below.

Table 3.3. Fabrication flow for 3D buried polymer waveguides.

Step		Parameters	Values
1.	Spin coating	Resist type	Polares 01- XP
		Layer Thickness	100-150 μm
2.	Prebake	Temperature	95 °C
3.	DLW (Nanoscribe)	Writing laser power	Average: 21.6 mW
		Writing depth	$\sim 60 \mu\text{m}$
		Writing speed	100 $\mu\text{m/s}$
4.	Soft bake / Core PEB	Temp./Time	40 °C / 60 min
5.	Diffusion With MOM monomer	Temp./Time	Room Temperature / 168 h
6.	Flood exposure	Dose / mJ/cm^2	500 mJ/cm^2
7.	Hard bake /Cladding PEB	Temp./Time	50 °C / 10 min
			Cooling down 140 °C / 10 min

3.4.7.1 Advantages and limitations of the fabrication method

This fabrication process possesses various advantages over other waveguide fabrication methods. It requires only one layer of a single material. Multi layers of waveguides can be inscribed in a single writing step without any stacking or alignment effort. This technique no longer involves masks, mold, stamp, contact or any wet chemical process steps such as wet etching. Hence, it is rapid to prototype

or redesign. In addition, the long wavelength chosen for TPA has less absorption and less scattering, which gives rise to the deep penetration of light. Finally, femtosecond pulses with high peak power initiates intense nonlinear processes without thermally damaging the resist due to low average power.

The main limitation of this fabrication technique is limited thickness to 100 μm due to structural instability at high temperature. Long diffusion duration of 168 hour retrains industrial lead-time even it is a purely passive process.

Chapter 4. Optical structures

This chapter discusses the characterization of the different optical structures fabricated to demonstrate applications of the newly developed method explained in Chapter 3.

In order to analyze the waveguide performance, we determine its index profile, guiding modes, mode field diameter, numerical aperture and transmission loss.

Main properties of optical waveguides are analyzed including sidewall roughness, area index profile, near field pattern, far field pattern, transmission loss, bend loss, and polarization dependent loss. Further characteristics of optical functions such as waveguide array, fan-ins/fan-out are also explained in detail. The reliability, typically the main challenge of embedded polymer waveguide via direct laser writing, concludes this section.

4.1 Single optical waveguides

4.1.1 Surface roughness and end facet and surface microscope analysis

This section characterizes top view, end facet view and surface profile of the waveguides using microscope picture and SEM micro graphs. These inspections were carried out before and after each fabrication process to regulate processing parameters such as laser power, writing speeds, heating temperature and time. Microscope pictures reveal the structure layout (top view), diffusion depth, feature sizes and rough index contrast (end facet view) while SEM micrographs showed the side wall roughness, feature size with high precision.

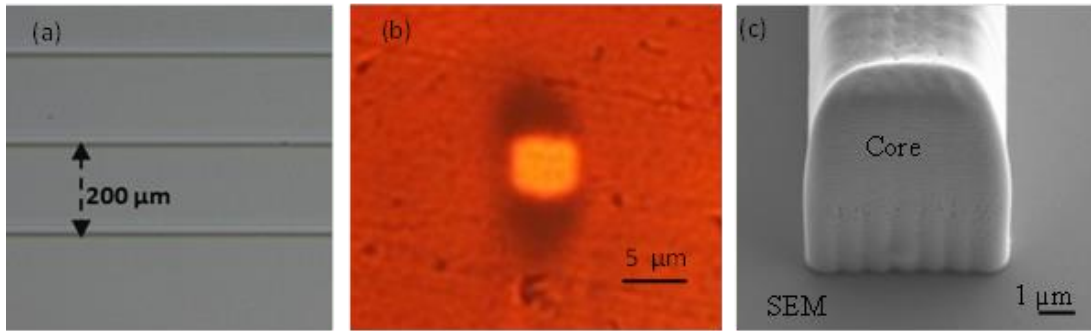


Figure 4.1 a) top view and (b) end facet view of waveguide with core dimensions of 5.7 μm; (c) SEM picture of the core after developing the uncross-linked cladding matrix with end facet view

Figure 4.1 (a) shows a front-illuminated top view of the waveguides. This step helps identify position, core-cladding contrast and homogeneity of the written structures. In addition, defects such as bends, burns or drifting (out of original position) could also be detected and subsequently minimized. Back-illuminated end facet view of the waveguide in Figure 4.1 (b) shows the physical core size, symmetry and a high positive contrast between the core and the cladding. The darker area above and below the core predicts the refractive index modification therein. This modification was revealed in SEM picture in Figure 4.1 (c).

The structure in Figure 4.1 (c) was partly written through the wafer surface so that the cured volume was attached to the wafer and remained after the chemical developing bath. The interaction between the wafer and the laser beam formed a standing wave on top of the wafer. The periodic modulation of the core structure in the vertical direction (i.e. perpendicular to the wafer plane) is attributed for this interaction. Seven separated sweeping lines are visible as well as the so-called proximity effect between them. This effect is attributed to the crosslinking of the gap between neighboring sweeping lines to form a continuous core structure.

4.1.2 Index profile

The refractive index profile of a waveguide determines its performance in mode propagation including the number of modes and the mode field diameter. As the waveguide structures are deeply buried in the resist layers, characterization methods for planar devices such as ellipsometry and prism coupling are not suitable here. Therefore, the refracted near field (RFN) technique has been used measuring the change in the power of refracted rays has been used. RNF is a high-resolution measurement method with step sizes of $0.1 \mu\text{m}$ and an index precision of 10^{-5} . BK7 glass and matching oil were used for referencing the measured material refractive index.

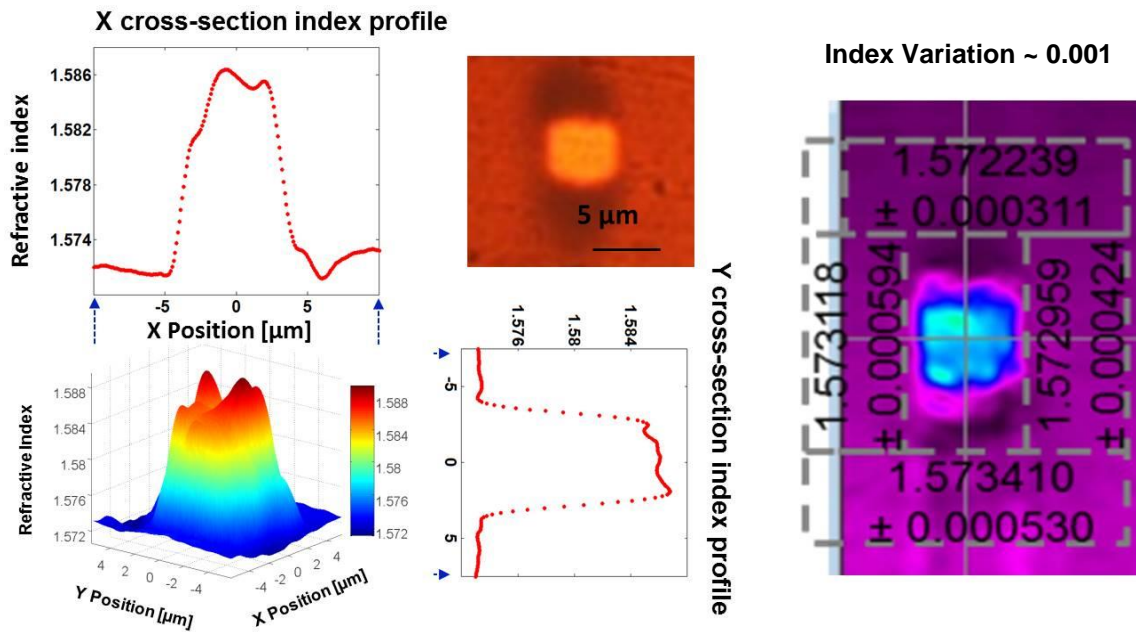


Figure 4.2 Area refractive index profile of a sample waveguide at the end facet measured with refracted near field method in 3D graph (a) and its cross section at $x=0$ (b). The peak index contrast between core and cladding at 678 nm is 0.013

Figure 4.2 plots the two-dimensional refractive index profile of the core and the cladding at 678 nm. The 3D graph shows a homogenous and symmetrical core with the size of $7.4 \mu\text{m}$. A smooth index transformation from the core to the cladding is a typical challenge of embedded waveguides. For instance the negative dips at the

core/cladding borders were observed in other methods [32]. These jumps degrade the guiding mode field and result in transmission loss of the waveguides.

The refractive index of the core fluctuates in a small range of 0.003 but decreases more significantly at the boundaries to the cladding. On the one hand, the high total index step of 0.013 assures single-mode guiding at communication wavelengths. On the other hand, the gradient index at the outer part of the core increases the light confinement. Refractive index distribution of the cladding around the core is homogenous with deviations of only 0.001. This variation is due to the exponential distribution of monomer concentration along the diffusion depth.

4.1.3 Near field pattern

The near-field intensity distribution is the first proof of light guiding along the core structures. It shows the confinement level of guiding light, which depends on index contrast, waveguide geometry.

To analyze the intensity distribution, the mode field diameter, the symmetry and the beam position of the guided modes in the fabricated waveguides, a Hamamatsu near field pattern (NFP) measurement system was used. The measurement system uses expansion optics with a high magnification (500×) and a digital CCD camera to acquire high resolution NFP image from the output facet of a waveguide after coupling monochromatic light to its input facet using an appropriate single mode fiber (Figure 4.3). The measurements are done with high-resolution with a scaling factor of 100 nm / pixel @ 850 nm on a Si-CCD chip camera and 130 nm / pixel at 1310 nm and 1550 nm on a Ge-CCD chip camera (*Camera InGaAs, Hamamatsu C10633-23*). A close view of part of the setup is shown on Figure 4.3 with the important components.

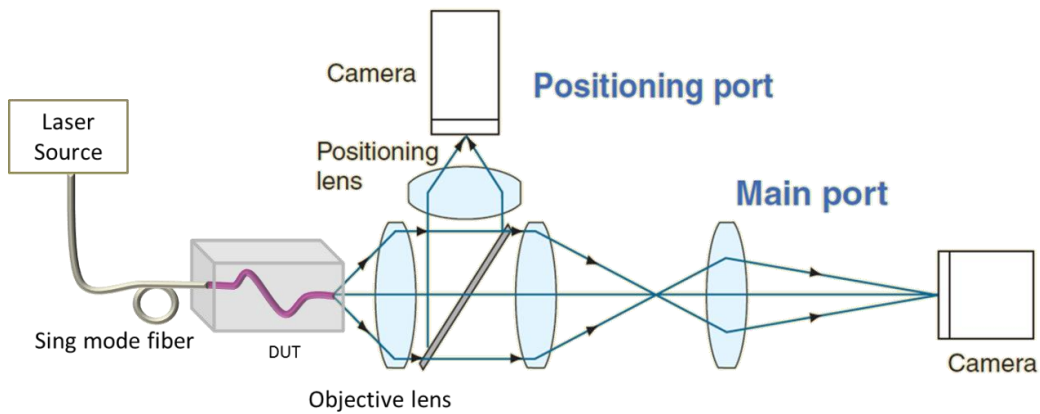


Figure 4.3 Near-field measurement system by HAMAMATSU. * Adapted from www.hamamatsu.com

In general, the near field and far field are distinguished by the numerical value of the Fresnel number NF . It is obtained from the ratio between the waveguide cross section (aperture area) and the wavelength multiplied by the measurement distance. The Fresnel number is applied in diffraction theory and defines the ranges of Fraunhofer diffraction by $NF < 0.01$ and Fresnel diffraction by $0.01 \leq NF \leq 100$ and $NF > 100$ define the range of geometrical optics.

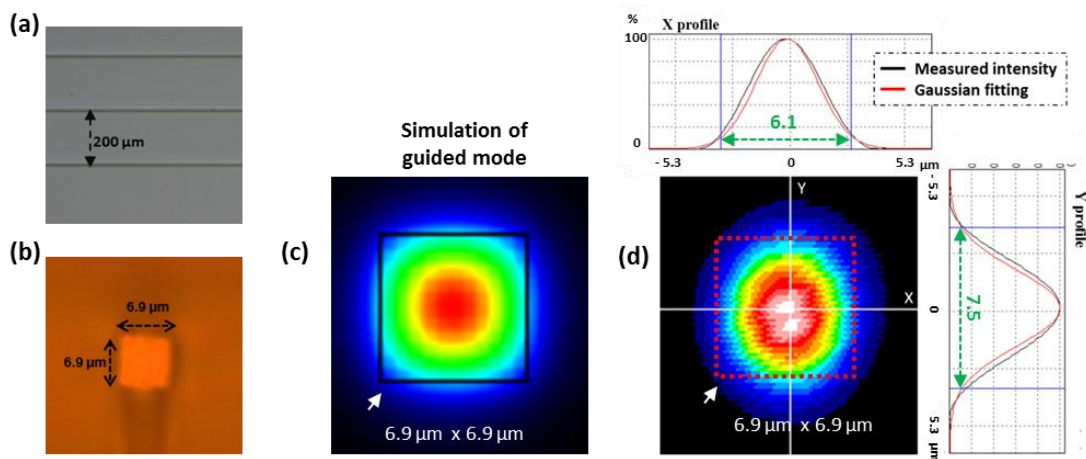


Figure 4.4. (a) Top view of a sample with 3 waveguides at a distance of 200 μm . (b) End facet view of a waveguide (written at speed of 200 $\mu\text{m}/\text{s}$ and input laser power of 42 mW); core dimensions are 6.9 μm x 6.9 μm . (c) BeamPROP simulation of intensity distribution of guided mode for this sample waveguide. (d) Measured near field profile illustrated with false color presents single guided mode at 1310 nm wavelength coupled from Corning SMF-28e single-mode fiber (central plot).

Figure 4.4 plots top view (a), end facet view (b), BeamPROP (RSOFT) simulation of single guided mode intensity distribution (c) and measured near field intensity profile (d) from sample waveguides with core cross section of $6.9 \mu\text{m} \times 6.9 \mu\text{m}$ and 2 cm length. The refractive index contrast between the core and the cladding is visible in subfigure (b).

The simulation results agree well with the measured NFP profile. A frame showing the physical dimensions of the waveguide core evaluates the confinement of the mode field. The resulting two-dimensional false color intensity distribution shows single mode guided light with a wavelength of 1310 nm launched from a standard single mode fiber (Corning SMF-28e). Both X and Y intensity profile present Gaussian distribution. The derived mode field diameter (MFD) at typical $1/e^2$ intensity points of the horizontal and vertical profile cross sections are $6.1 \mu\text{m}$ and $7.5 \mu\text{m}$ respectively. A small ellipticity is attributed to the weak differences between the profile gradients in horizontal and vertical direction.

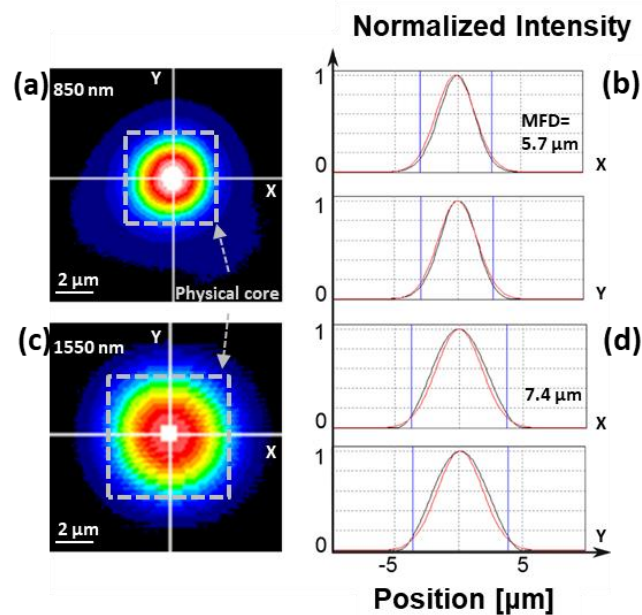


Figure 4.5 Near field pattern of the waveguides measured at transmission wavelengths: Near field intensity profile in false color measured at 850 nm in comparison with the physical core, and its cross sections in x and y at 850 nm (a, b) and at 1550nm (c, d). The $1/e^2$ mode field diameters are both $5.7 \pm 0.3 \mu\text{m}$ at 850 nm and both $7.4 \pm 0.4 \mu\text{m}$ at 1550nm. Black curve: measured intensity profile; red curve: Gaussian fitting.

Figure 4.5 presents the near field patterns and their cross section profiles for transmission wavelengths of 850 nm (a, b) and 1550 nm (c, d). Beam propagation method from BeamPROP™ was utilized to simulate and optimize the waveguide core dimensions. The actual cores in comparison with the near field patterns reveal the light confinement of the guided single mode. All intensity profiles fit well with Gaussian distributions with a mode field diameter derived at 1/e² intensity of 5.7 μm and 7.4 μm at 850 nm and 1550 nm respectively. These cross section profiles show highly symmetrical mode fields with diameters comparable with single-mode optical fibers. The near-perfect Gaussian profiles of the intensity sections along the main axes are also to be assessed positively. However, this is only true if the mode guide is strictly single-mode. Compared to the optical waveguides produced within the project and the previously described dimensions of their mode field diameters, the standard single-mode fibers.

4.1.4 Far field pattern

Measurements of the far-field intensity distributions (FFP) provide values for specifying the numerical aperture (NA). The NA is defined as half the opening angle of the divergent laser radiation that propagates in the free space at the end of the core structure.

$$NA = n_{air} \cdot \sin\left(\frac{\theta}{2}\right)$$

A dedicated optical system and a digital CCD camera acquire a 2D image of the beam spread angle of a semiconductor laser. The center of the acquired image represents the optical intensity at 0° versus the optics axis.

$$\Delta n = n_{core} - n_{sub} \Delta n = \frac{NA^2}{2n_{sub}}$$

$$\Delta n = n_{core} - n_{sub}$$

In addition, the NA value may help to calculate the standard V parameter that defines the value of single mode design limit ($V \leq 2.4$, for a step index fiber).

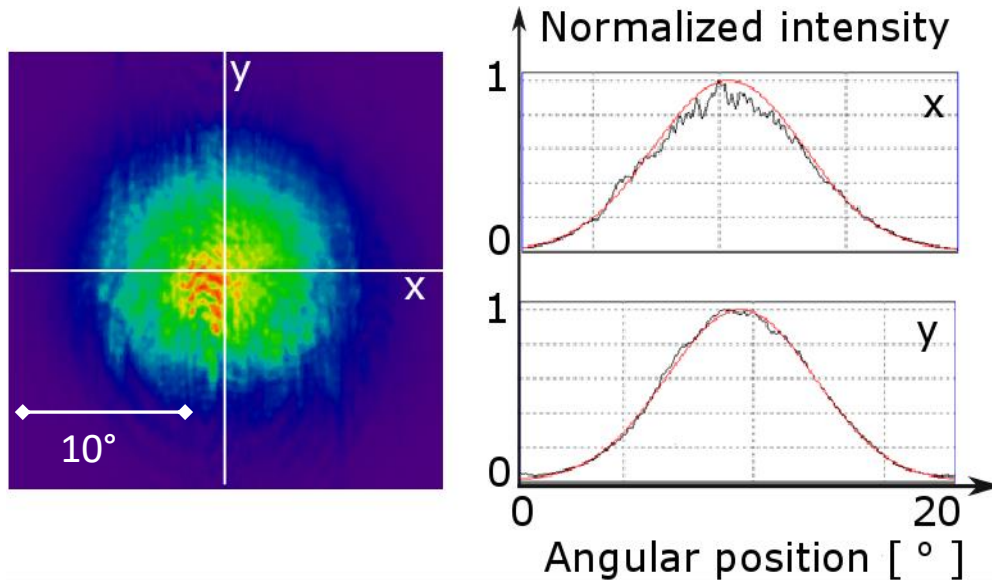


Figure 4.6 Far field pattern measured at 850 nm and its intensity profile cross sections.

Figure 4.6 depicts the far field pattern of a waveguide coupled from a Corning HI780 fiber at 850 nm and its cross section profiles. The full divergence beam amounts to 17 °. The resulting numerical aperture amounts to 0.148 ± 0.01 and is comparable to the numerical aperture of the single mode fiber at 850 nm.

4.1.5 Transmission loss

Polymer materials commonly have higher absorption in the spectral ranges relevant to optical communications compared to silicon. Scattering contributes dominantly to the overall attenuation in optical waveguides compared to material absorption [78]. Hence, it is important to determine its transmission and the coupling losses of the waveguides. We applied the cutback method and the overlap integral method to determine these values.

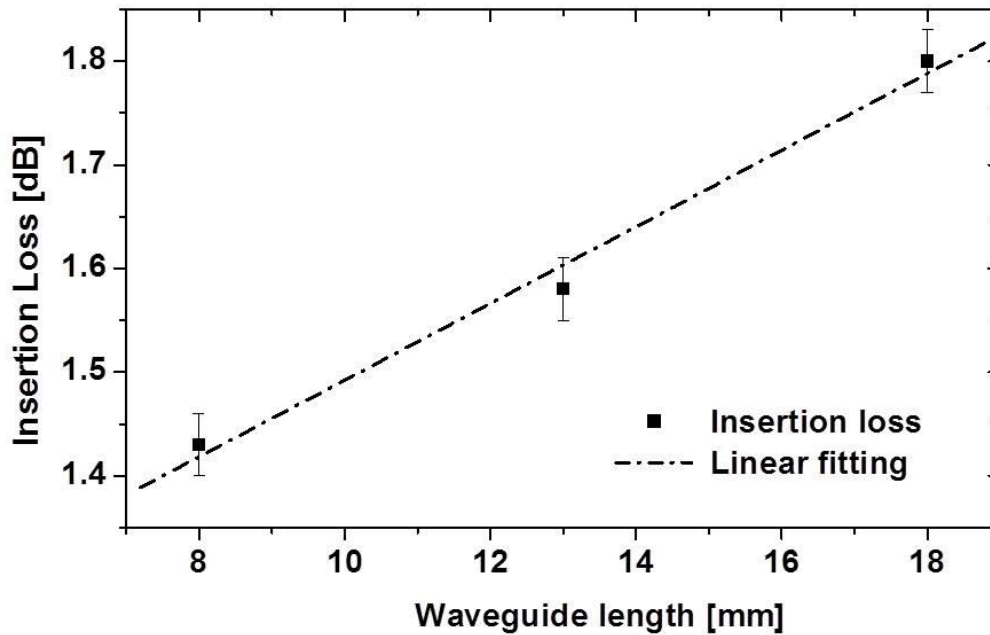


Figure 4.7 Insertion Loss at 850 nm

The cutback method exploits different insertion losses at various waveguide lengths to determine the transmission loss. In this experiment, two Corning HI780 single-mode fibers couple the 850 nm light in and out of the waveguide by butt coupling. Insertion losses at 8 mm, 13 mm and 18 mm lengths, plotted in Figure 4.7, were linearly fitted. The slope of this line reveals the transmission loss of 0.37 dB per cm, while its zero-intersection shows the total coupling loss of 1.12 dB.

Alternatively, the coupling loss was derived using the overlap integral. Two main contributions of coupling loss, which are mode field mismatch and numerical aperture mismatch, were calculated as 0.07 dB and 0.42 dB respectively for each fiber-waveguide coupling. The total coupling loss for both input and output of the waveguide is 0.98 dB. This result is consistent with the cutback method, since the coupling loss difference of 0.14 is attributed to the imperfect coupling.

There are some reasons to expect a lower transmission loss by further improvement. The surface roughness, a main contribution to attenuation apart from material absorption, was in the order of $\lambda/2$ for waveguides with core

dimensions of 5 μm . It drops significantly to an intrinsic oscillation of the translating piezo of $\lambda/20$ by increasing the material absorption at 390 nm wavelength. Furthermore, single-photon absorption experiments of a similar photopolymer based on the same epoxy oligomer has been used to fabricate single-mode polymer waveguides with transmission loss lower than 0.2 dB per cm at 850 nm wavelength [23]. Analogous measurements at 1310 nm resulted in a transmission loss of 0.95 dB/cm [79]

4.1.6 Bend loss

Bends are an essential building block of 3D waveguides. As opposed to straight waveguides, curved waveguides show more radiation loss. An intuitive explanation is: The phase front of the guided mode is turning around the center of the bend, because the group velocity of the phase front cannot exceed the speed of light, the phase fronts bend and cause radiation. Radiation losses increases exponentially with decreasing bend radius [19]. Extensive experiments have shown that surface roughness is the main cause for high propagation losses [21, 22]. However, the bends are designed for single mode propagation to avoid excessive bending losses and polarization conversion losses.

The S-shaped bend is a bend waveguide connecting two lateral displaced parallel straight waveguides. The radius of curvature along the bend varies gradually to realize the lateral displacement and connection. Considering from the nature of the bending, the insertion loss of the S-shaped bend includes two parts: pure bending loss and transition loss. The eigenmodes of a bend waveguide are leaky modes. Power will gradually attenuate when light propagates through a bend waveguide.

Marcatili and Miller firstly derived the pure bending loss of a circular waveguide:

$$\alpha(R) = 8.686 C_1 \times e^{(-C_2R)} \text{ [dB/m]}$$

where C_1 and C_2 are two constants depending on the waveguide structure and on the shape of the optical mode [7, 8], and R is the curvature radius. The transition loss is induced by a mode mismatch of a connection of two waveguides with

different curvature radii. Therefore, an S-shaped bend connected by two circular arcs has a minimum pure bending loss, but a great transition loss.

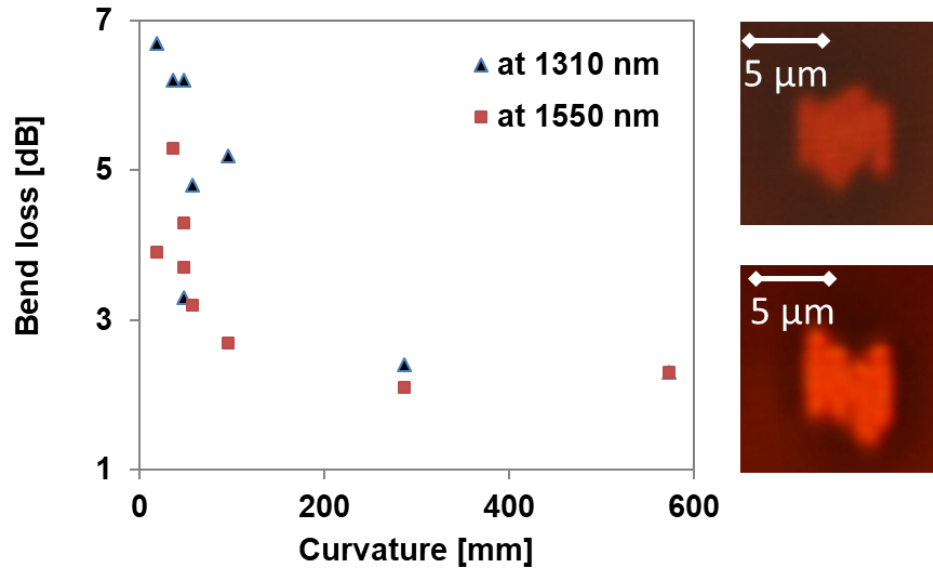


Figure 4.8 Bend loss vs. Radius of curvature at 1310 nm and 1550 nm for waveguides of 2mm length with sine function. Right: end facet images of 2 waveguides in the sample wafer showing shifted voxel

Using cosine function, waveguides were fabricated with lateral offset from 10 to 500 μm . These offsets were translated to radius of curvature by approximating the derivative in numerical differentiation. The high bend loss shown in Figure 4.8 is attributed to the core deformation causing by the stage instability.

4.1.7 Polarization dependent loss

Polarization dependent loss (PDL) is defined as the variation of transmitted optical power of the device when the input takes on all polarization states. Figure 4.9 illustrates this definition and shows how PDL can be theoretically measured. The Poincaré sphere visualizes all states of polarization on its surface wherein the right-hand circular (RHC) and left-hand circular (LHC) states and linear polarizations rotated through 360° are mapped. Components S_1 , S_2 and S_3 indicate the coordinate system of Stokes vectors at the center of the sphere. After all possible polarization states are fed to the device under test (DUT), the ratio

between the maximum (T_{max}) and minimum (T_{min}) output optical power determine the polarization dependent loss as: $PDL = 10 \log \frac{T_{max}}{T_{min}}$ [dB].

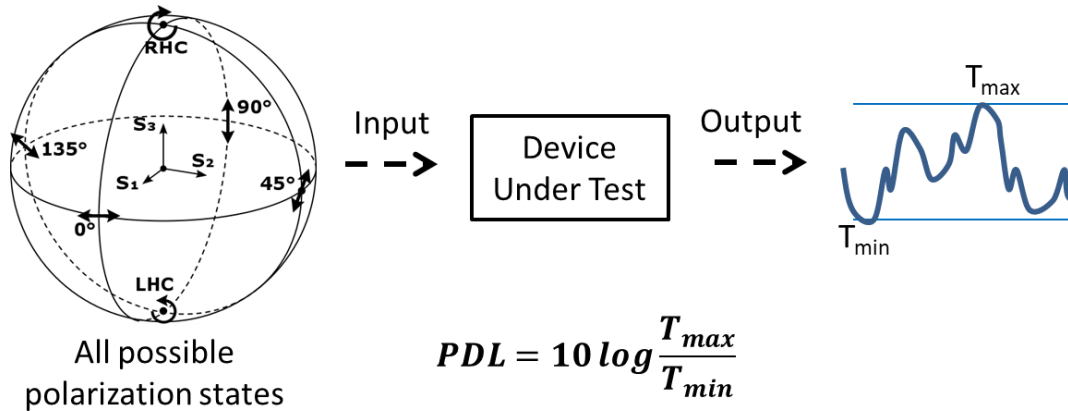


Figure 4.9 Illustrated definition of PDL through Poincaré sphere

It is indispensable to identify PDL parameter for optical waveguides, especially by means of a new fabrication method using novel material. Maximum PDL is desirable for some components such as integrated optical polarizer utilizing calcite on a glass substrate [80]. Nevertheless, in other devices and optical systems, a high *PDL generates* signal distortion leading to system degradation in , for instance, dense wavelength division multiplexing (DWDM) systems [81].

The polarization dependent loss (PDL) of the waveguides is a difficult parameter to control during the fabrication process. Its impact on various integrated waveguides has been analyzed to optimize fabrication process e.g. in III-nitride optical waveguides [82], polymeric rib channel waveguide [83,84], or polymeric optical waveguide circuits using silicone resin [85]. Kobayashi et al. has reported that PDL in a buried or rib waveguide is usually less than 1 dB due to different confinement factors of the guiding for two polarization modes (TE and TM modes) [86]. In an integrated waveguide, the major contributors to this loss are waveguide geometry, stress birefringence, refractive index profile; while in a transmission system it is primarily associated with medium-medium boundary such as glass-air interface, oblique internal reflections, fiber bending, and dichroic media. Because identifying the stress birefringence and 2D refractive index profile

for each development cycle is troublesome and time consuming; only the waveguide geometry and homogeneity were controlled during our processes using microscopic photos and mode field diameters i.e. near field patterns.

4.1.7.1 Measurement methods

Two main groups of PDL measurement methods include scanning methods and fixed-states methods. The polarization scanning technique is suitable for PDL measurements at specific wavelengths. On the other hand, for a broad wavelength range the fixed-states methods such as Mueller Method (4x4 matrix) or Jones Matrix Method (2x2 matrix) possess clear advantages thanks to their high speed and simplicity [87]. Recently, Sagues introduced a novel method for high wavelength-resolution measurement of PDL using swept optical single sideband modulated signals [88].

This work used Jones Matrix Method at 808 nm and scanning methods at 1310 nm to measure PDL of the fabricated waveguides.

The Jones matrix method measures the device's polarization response to three orthogonal input states of polarization at a wavelength of interest. Eigenvectors of the Jones-Matrix transformed into different output polarizations are measured by the polarimeter as azimuth angle and ellipticity. This polarimeter internal PDL limit the measurement accuracy, while its signal-to-noise ratio restricts the measurement resolution. The common polarization inputs are linear states at 0° (linear horizontal polarized), 90° (linear vertical polarized) and 45° (linear $+45^\circ$) [89].

Polarization scanning method directly determines maximum and minimum transmission of the device under test (DUT). The DUT is exposed to a large subset of the entire Poincaré sphere through a pseudo-random variation of retardance, usually the distributed retardance of optical fiber loops in motion. A longer polarization scan, meaning more input polarization states, reduces the uncertainty of the PDL measurement. This method has the advantage of low system noise,

weak wavelength dependence, and low internal PDL since the beam remains confined in a single-mode fiber.

4.1.7.2 Experiments and Analysis

The 808nm (Topica) and 1310nm (Thorlabs) stabilized laser diodes were used as light sources for polarization dependent loss measurements. The light was firstly coupled into the waveguides through an optical fiber, which is polarization maintaining fiber at 808nm for Jones Matrix method, and is a standard single mode fiber at 1310nm for polarization scanning method. An objective lens was used at the output coupling. The input fiber and the output lens were precisely aligned and butted against the waveguide facet through the observation of the mode picture on a monitor.

Through analyzing the average azimuth and ellipticity data, PDL value can be calculated for Jones matrix method and by calculating the absolute difference value of maximum power and minimum power to get PDL value for Maximum Minimum method. For very high precision PDL measurements, the number of averaging for a polarization measurement must be augmented to reduce statistical errors and noise.

Since the optical elements will also contribute a small amount of PDL they would disturb a highly precise PDL measurement. Measurement errors come from light source fluctuation, double reflections (<0.02 dB, connector (<0.06 dB) and cable (<0.02 dB) contributions [90]. Therefore, a reference measurement is necessary to minimize the influence of the polarizer module and the connected fibers. The device under test must be removed to conduct reference measurement. The PDL value deduced from the eigenvalues of the Jones-Matrix were 1dB and 0.6dB for scanning method.

At 850 nm, for 18 mm-long waveguides, measured PDL fluctuated between 0.42 dB and 1.01 dB. The average PDL was 0.32 dB/cm. At 1310 nm, polarization scanning method revealed PDL in the range between 0.1 dB and 0.5 dB/cm. Average PDL accounts for 0.33 dB dB/cm.

4.2 Multilayer waveguide arrays

Using the process flow described in Chapter 3, we fabricated 4×2 waveguide arrays with a $25\text{-}\mu\text{m}$ pitch size. Figure 4.10 depicts the end-facet view (a), refractive index profile in 3D (b) and near field pattern (c) of an array. The end-facet picture taken by a microscope indicates a high visual contrast between the cores and the cladding thanks to the high refractive index contrast of $0.016 - 0.018$. The refractive index profile as 2D scan measured by the refractive near field method (RNF) shows a gradient index distribution of the core. Thanks to the nature of diffusion, the monomer concentration is higher closer to the top of the layer i.e. closer to the diffusion interface. That explains the lower refractive index of the cladding approaching the top surface. Near-field measurement reveals symmetrical mode field with diameter of $5.5 \pm 0.21\ \mu\text{m}$ at $1310\ \text{nm}$ wavelength.

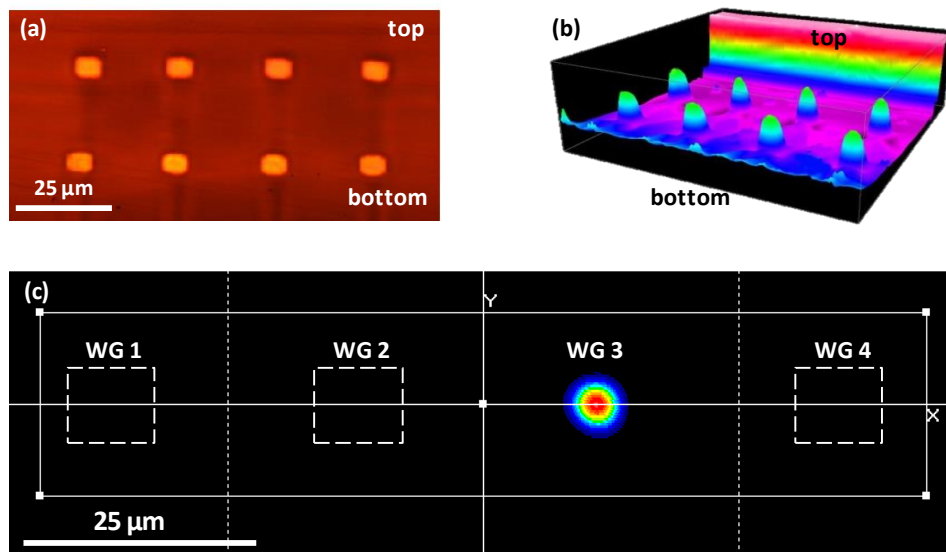


Figure 4.10. Characterizations of a 4×2 waveguide array: (a) End facet microscope picture shows high contrast between waveguide cores and cladding, and satisfying alignment accuracy between top and bottom layer; (b) qualitative isometric view of refractive index profile measured by refracted near field portrays homogeneity of the cladding; (c) Near field pattern introduces guiding mode in a waveguide core and invisible crosstalk to neighboring waveguides (dotted frame marks the positions of the neighboring waveguide cores)

As the stacking and alignment are not necessary in our process, laser writing aligns waveguide layers precisely within a single patterning step as shown in Figure 4.10.

(a) Qualitative 3D refractive index profile plotted in subfigure (b) presents clear contrast between waveguide cores and cladding. Furthermore, the homogeneity achieved by using a single layer of material results in a cross talk as low as -34 dB between neighboring waveguides. As seen from subfigure (c), not only the guiding mode field is clear and symmetrical but also the neighboring mode fields (with pitch size of 25 μm) are not visible.

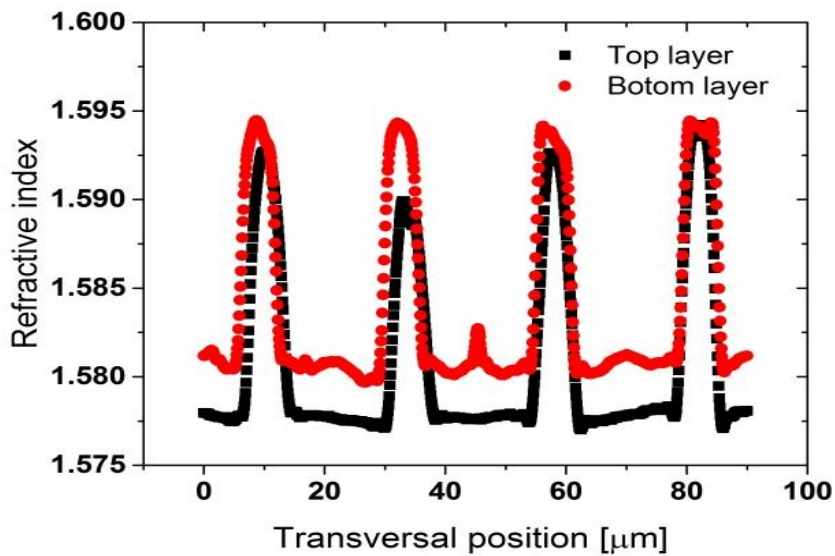


Figure 4.11 Transversal distribution of refractive index for waveguide cores and cladding measured by refracted near field method

Figure 4.11 demonstrates the horizontal index profile between waveguides across the core structure centers. The highest displacement between the top and bottom waveguide layers measured by RNF was 1.2 μm . Its average value is 0.67 μm . Thanks to the laser beam high position accuracy of $\pm 0.1 \mu\text{m}$, the major lateral offset of waveguide position is accounted for the material softening and inner stress during diffusion process.

4.3 Fanin Fanouts

Multicore fibers (MCF) allow high data traffic and more power in optical links. As the MCF cores locate both vertically and horizontally, a device to couple this MCF

into a linear array of single fibers or fiber ribbon is required. Usually, the fan-in/out polymer waveguide consists of multiple planar waveguides (fabricated by using conventional photolithography) that are stacked layer by layer. In this case, it is a challenge to realize the pitch conversion in the vertical direction [91].

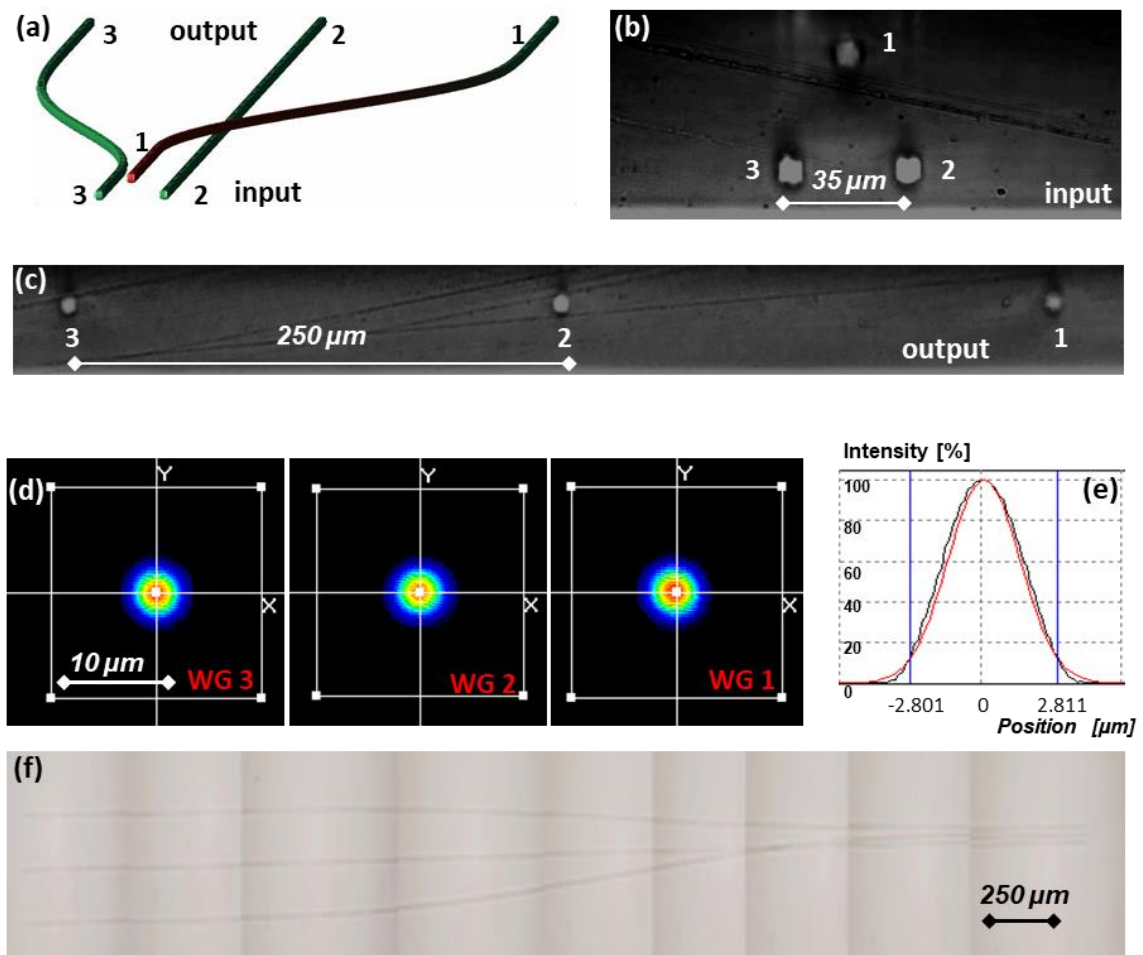


Figure 4.12 (a) Schematic of an optical 3-core fanout for pitch conversion in both vertical and horizontal direction; End facet microscope picture of the input (b) and output (c) of the prototype; Two-dimensional pitch of 35 μm is converted to a linear pitch of 250 μm ; (d) Near field profiles at the output facets which were measured separately; (e) Horizontal cross section of near field profile of the waveguide 1 and its Gaussian fitting curve (red) (f) Top view microscope picture by aligning a series of photos

In this work, we fabricated single-mode 3-core fan-outs using contactless laser inscription as depicted in Figure 4.12. The device converted the 2D 35- μm pitch at the multi-core input to a linear pitch of 250 μm at the output array. With the

structure length of 2 cm, the straight waveguide (WG2) exhibits a minimum insertion loss of 4.2 dB at 1310 nm when coupled to two single-mode fibers. WG1, whose output is horizontally shifted by 215 μm (in relation to the input), bears an additional loss of 2.5 dB. The output of WG3 is moved by 267.5 μm and 30.3 μm in horizontal and vertical direction respectively and therefore adds further 2.1 dB insertion loss. Figure 4.12 (d, e) illustrate the guiding mode field for each output of the fan-out and one of their cross sections. The average mode field derived at $1/e^2$ intensity stands $5.61 \pm 0.21 \mu\text{m}$ at 1310 nm and $5.74 \pm 0.21 \mu\text{m}$ at 1550 nm. Compared to the physical dimension of $6.9 \pm 0.1 \mu\text{m}$, the guiding modes are well confined thanks to the high index contrast and the graded-index profiles.

The future work is to produce 7-core fan-in/fan-out with pitch size of 35 μm . The challenge is to increase the diffusion depth to more than 100 μm without degrading the structural stability.

4.4 Reliability

The fabricated waveguides indicate excellent thermal, mechanical and chemical stability. Baking samples up to 200 °C did not affect its near field pattern and transmission loss. Subsequent analysis of waveguide positions revealed neither bends nor shifts. Storing samples in a laboratory environment without any protection for more than one year did not degrade their optical performance. Furthermore, sequential chemical baths with acetone and PGMEA did not detach the resist from the silicon wafer.

To test the thermal stability, microscopic pictures and near-field patterns were compared before and after baking the samples at 160° and 200°. On the microscopic picture, change or deformation of the waveguides and their distance could hardly be observed. For the mode propagation of 850nm (NearIR) laser light we observe slight change in the intensity required for the optimized state between the first and second baking process. Figure 4.13 shows the measurement results.

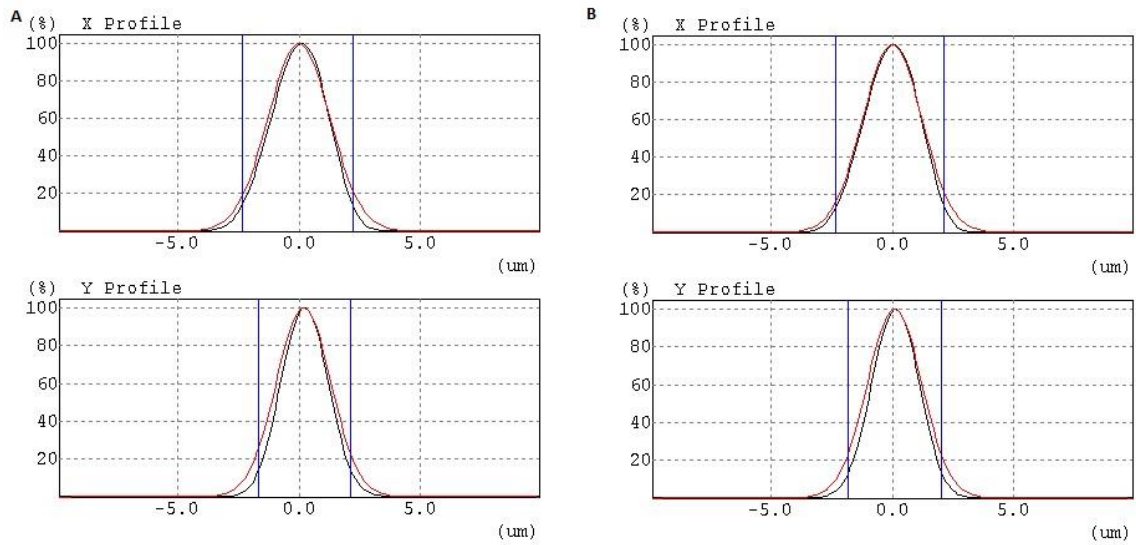


Figure 4.13 The beam profiles of WG#6, Group#2 after first bake (A) and second bake (B). The intensity of the laser used is 0.79mw, 0.89mw respectively. The beam profiles are almost identical.

Neither the dimensions of the waveguide and the distances between them nor the transmission loss in the polymer was changed.

Chapter 5. System integration

This chapter discusses the optoelectronic integration of the fabricated waveguides and the concept of decoupling pitch size vertically and horizontally.

5.1 Concept

Significant challenges are emerging for board level optical interconnections across multiple packaging layers [92]. Two-dimensional arrays of optical interconnects are capable of providing high bandwidth, low power, and low noise connectivity between integrated circuits, boards, and racks. The horizontal pitch size is limited by the chip size of the laser source e.g. VCSEL which is in the range of $250\ \mu\text{m}$. To date, the distance between vertical waveguide layers is defined by the vertical pitch size. In this section, in the one hand we introduce a concept to tackle this issue by decoupling vertical pitch size from horizontal pitch size using total internal reflection (TIR) mirrors via laser ablation. On the other hand, our fabrication technique introduces a third dimension to improve the design freedom and compactness. Laser ablation and LIFT (laser induced forward transfer) micro bumps offer low temperature processing, high flexibility and low cost.

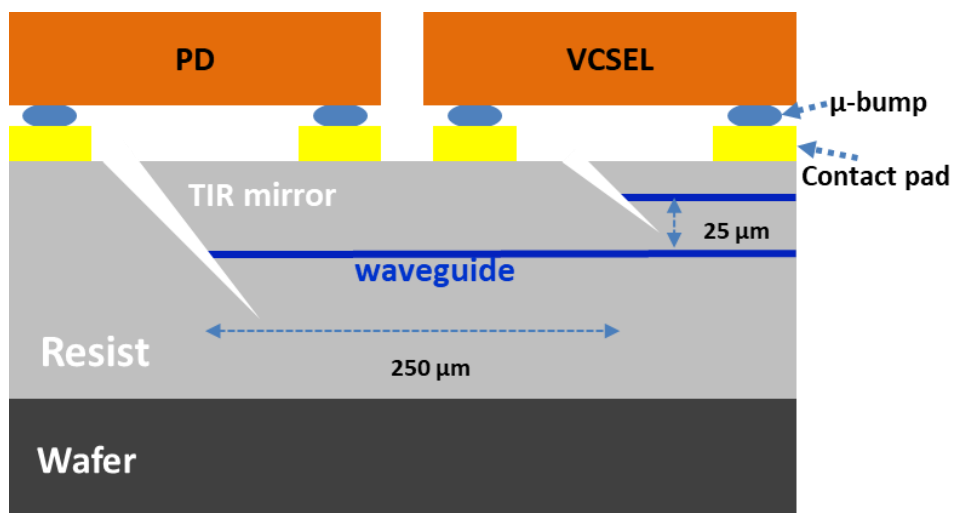


Figure 5.1 Concept of decoupling the vertical pitch size from horizontal pitch size to increase the interconnect density

Figure 5.1 demonstrate the bi-directional schematic of this decoupling concept. Two laser-ablated mirrors decouple two waveguide layers of a 25- μm pitch size to a transmitter or a transceiver array with significantly larger pitch size e.g. 250 μm . The main driver for this concept is the various mirror depths at several micron difference defined at high precision. The air gap created by ablating the material at a desired depth and angle create the index step from polymer to air. This index step and large enough incoming angle from the waveguide guiding light turn the polymer/air surface into a TIR mirror. This mirror reflects light from/ and to the embedded resist layer.

5.2 Fabrication method

Figure 5.2 shows the fabrication process including 6 major steps: casting of photopolymer, waveguide array inscription by two-photon lithography (2PL), patterning the bonding pad using image reversal lithography, LIFT micro bumps, laser ablation of TIR (total internal reflection), flip-chip thermo-compression bonding OE components.

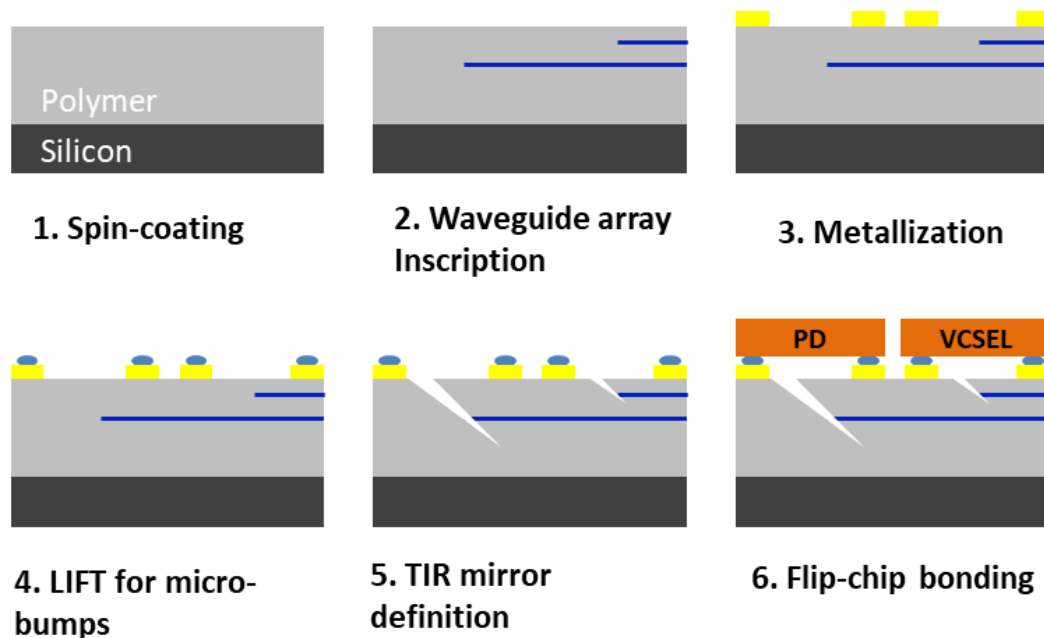


Figure 5.2 Process flow for optoelectronic integration of multi-layer waveguide array

Each section below will explain in detail the method used for each step, the technical background and their advantages.

5.2.1 Multi-layer waveguide description

The waveguide array was inscribed into a single layer of one material employing the combination of femtosecond laser writing and external diffusion. A subsequent flood exposure at 390 nm and hard bake assured permanent refractive index modification of the structure. The wafer was then diced to the dimensions of 1 cm × 2 cm. This fabrication method involves neither stacking nor alignment effort.

5.2.2 Contact pad metallization using image reversal lithography

Among various candidates such as etching, lift off, image reversal lithography was the most suitable process to define the contact pads directly on the surface of the photopolymer thanks to its low violation to the material.

Bonding pads were defined directly on top of the photopolymer layer by means of the standard image reversal lithography using positive photoresist AZ5214E. The resulting negative side wall profile guaranteed a smooth lift-off process after sputtering 10 nm of Ti and evaporating 300 nm of Au. The detailed process flow and recipe is shown below.

Table 5.1: Fabrication recipe of image reversal lithography using AZ5214E

Spin Tiprime	3000 rpm
Softbake	3 minutes at 120 °C
Spin AZ5214E	40 seconds at 1800 rpm
Softbake	50 seconds at 110 °C
UV exposure with mask	20 seconds
Postbake	3 minutes at 120 °C
Flood exposure	30 seconds
Development	in AZ 400K:H2O ratio of 1:3 for 10 minutes
Flash oxygen plasma	30 seconds RIE
Sputtering Ti/Evaporation Au	10/300 nm

Attention must be paid for the baking steps. Cooling down the samples too quickly could cause delamination. At least 1 h for cooling down from 120 C to room temperature was needed. Hence, the developing time was increased to 10 minutes instead of 1 minute. Under-developing caused incomplete lift-off and extreme low adhesion of the bonding pads. Typically, the contact pads consist of 3 layers of Ti/Ni/Au. However, in our work, skipping the 50-nm Ni layer between Ti and Au did not degrade the performance of the contact pads such as adhesion and conductivity.

5.2.3 LIFT micro bumps

Traditionally, the most widely used bump material for FC bonding was lead (Pb) alloy solder, which is highly toxic and requires flux. Fluxless bonding for optoelectronic components is essential to avoid contamination of active areas. Lead-free and fluxless alternatives such as conductive adhesives, gold, copper, and indium based alloys involve a high temperature process [93,94]. Stud bumping [95,96], evaporation [97], electroplating [98], and stencil printing [99] are the common bumping techniques. These methods, however, suffer from drawbacks such as high processing temperatures, cost, manufacturing time and low flexibility [94,97].

LIFT is a laser-based bumping technique that can tackle aforementioned issues. LIFT focuses laser pulses through a transparent substrate (the carrier) onto the rear side of a thin film (the donor) [100]. These forward the donor material to the receiver substrate placed in close proximity. LIFT possesses four major improvements comprising low temperature processing, simplicity and flexibility, cost effectiveness and, thinner bump thickness.

Micro-bumps of indium with 80 μm diameter and 2 μm thickness were printed on the bonding pads. A commercial laser source Timebandwidth Duetto (12 ps, 355 nm) and a transfer fluence of 300 mJ/cm² was used for the LIFT experiments. The laser fluence used for transferring the metallic bumps was \sim 270 mJ/cm². For

stacking, first, an indium bump was LIFTed onto the receiver bond pad, then the donor was moved to a fresh area and another bump was printed on top of the previously printed one.

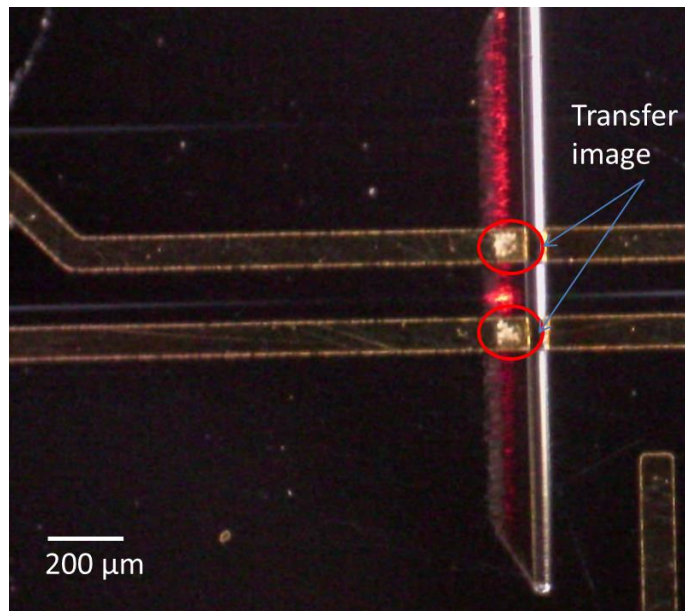


Figure 5.3 LIFT topview : LIFT bumps on top of connecting pads

Figure 5.3 shows the top view of a lifted micro bumps on Ti/Au pads. The position of the bumps was well controlled and the thickness of 2 μm was confirmed by Wyco measurement.

5.2.4 Laser ablation for mirror definition

There are plenty techniques for 45° mirror fabrication in polymers for instance dicing, laser ablation, direct grey-scale lithography, blade cut, RIE, tilted exposure. Since the precise control of the mirror depth is crucial for our concept, we chose laser ablation to define the TIR mirrors. In general, the energy of the laser beam is absorbed in a thin layer or small volume and the ablation process takes place through rapid fragmentation. Depending on the wavelength and the material, this can have the characteristics of ablative photo-decomposition, or rapid heating and vaporization. This micromachining technology has already been used in PCB manufacturing for the drilling of microvias in high density boards and trimming of embedded resistors.

Laser ablation is based on the controlled removal of material with intense laser pulses. In general, the energy of the laser beam is absorbed in a thin layer or small volume and the ablation process takes place through rapid fragmentation. Depending on the wavelength and the material, this can have the characteristics of ablative photodecomposition, or rapid heating and vaporization. KrF excimer laser ablation (wavelength 248 nm) is particularly well suited for structuring of polymers because of their excellent UV-absorption properties and non-thermal ablation behavior.

There are two different laser ablation mirror fabrication approaches: tilted laser ablation and distributed laser ablation. The distributed laser ablation is performed using a triangular shaped beam. Dynamic ablation with such a shaped beam results in a V-groove. By controlling the depth of the V-groove, we can control the angle of the sidewalls of the V-groove. The main drawback of the distributed laser ablation is the poor depth control since the depth of the groove defines the angle of the mirror facet. This issue becomes crucial for multi-layer waveguide array. On the contrary, the tilted laser ablation can independently control both the trench depth and facet angle by modifying laser beam angle, scanning speed and laser power. It is less sensitive to power fluctuations as well. Its setup consists of tilting the optics from the beam delivery unit on the laser set-up in such a way that the laser beam will incident the polymer surface under an angle, which can be controlled with an accuracy of 0.5 degree using a micro-screw. Scanning in the direction perpendicular to the waveguides ablates the trench forming the negative facet; (see Figure 5.5(a)). However, one disadvantage of this scanning approach compared to distributed laser ablation is a higher surface roughness.

In our approach, simply changing the angle of a turning mirror can tilt the excimer laser beam. Each facet is fabricated by sending the laser beam through a rectangular aperture that is projected on the sample. Laser pulses from an excimer laser (KrF, operating wavelength 248 nm, pulse duration 5-8 ns, pulse energy 189 μ J) were first passed through a rectangle mask, and a 10 \times demagnified image was

projected onto the sample. The sample was then scanned in a certain angle to the incoming laser beam at a speed of 600 $\mu\text{m/s}$ at 100 Hz repetition rate. The simplicity of this technique lies in the fact that the TIR mirror angle can be tuned just by adjusting the laser energy and the sample scan speed and the number of scans. The optimum combination of the number of passes and the laser tilt angle were tested to achieve a linear 45° slope.

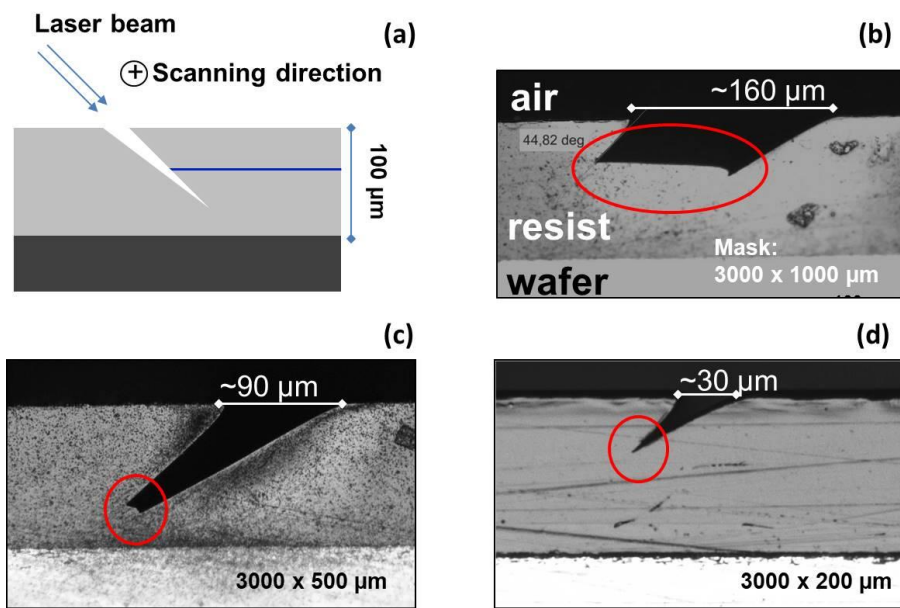


Figure 5.4 Laser ablation principle (a) and the resulting ablated mirrors by different mask width: 1000 μm (b) 500 μm (c) and 200 μm (d)

The width of the rectangular mask (along the scanning direction) shapes the ablated trench, in particularly the opening and the bottom width. Since the width of the VCSEL and the photodiode (PD) chip is typically 250-300 μm , the ablated trench opening should be substantially smaller than 150 μm for high stability of the chip after chip bonding. More important, the residual bottom step must be constrained to less than 1 μm to ensure a small vertical compactness for a 25 μm pitch size. Reducing the mask width from 1 mm to 0.2 mm improves the trench shape significantly (see Figure 5.4). With the 200- μm wide mask the trench opening was from 160 μm to less than 30 μm and the bottom step was eliminated. It can be seen that using the excimer laser, there is always a certain tapering of the

edges. The tapering effect is shown to be highly reproducible; therefore this effect can be compensated to achieve an angle of 45° at the negative facet.

Figure 5.5(a, b) show the variation of the ablation depth and in turn the mirror angle as a function of number of scanning steps obtained during the optimization cycle. The resulting parameter for the first and second layer was $36\ \mu\text{m}$ and $74\ \mu\text{m}$. The waveguide depth is $17\ \mu\text{m}$ for the top and $46\ \mu\text{m}$ for the bottom layer.

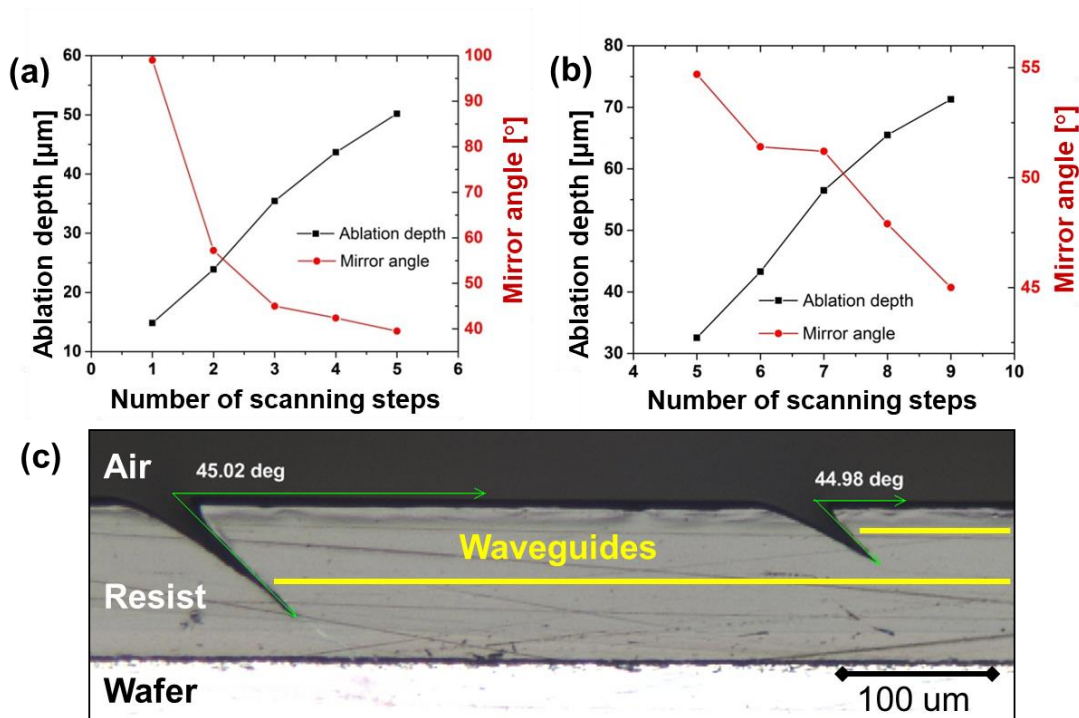


Figure 5.5 Ablation depth and negative facet angle as a function of scanning steps with laser tilt angle of 298° (a) and 294° (b); Side view of two layer 45° mirrors (c)

Figure 5.5(c) shows the side view of two layer 45° mirrors. The variation depth and negative facet angles were engineered to fit the two-waveguide layers.

5.2.5 Chip placing

The final step in the assembly was to flip-chip bond the OE components to the bumped receiver substrates employing thermo compression bonding technique. A semiautomatic flip-chip bonder (T 320-X) from Tresky was used to apply thermo-

compression bonding of these chips to the conducting bumps, thereby, establishing an electrical and mechanical interconnection between the chips and the substrates. Thanks to high contrast of the index, waveguides cores are visible which helps perform the alignment process. A contact load in the range of 6.25–25 gf/bump-stack was used for bonding the chips and the temperature between the pick-up tool and the chip was set to 190 °C to ensure welding of the chip to the substrate via molten indium bumps (melting point of indium ~157 °C). It is important to mention here that it was difficult to measure the actual temperature at the bonding interface with the present set-up of bonder. The temperature was therefore measured at the chuck that picks up the chip. However, due to non-perfect heat transfer to the bond pads on the other side of the chip, the actual temperature at the bonding interface is lower than 190 °C.

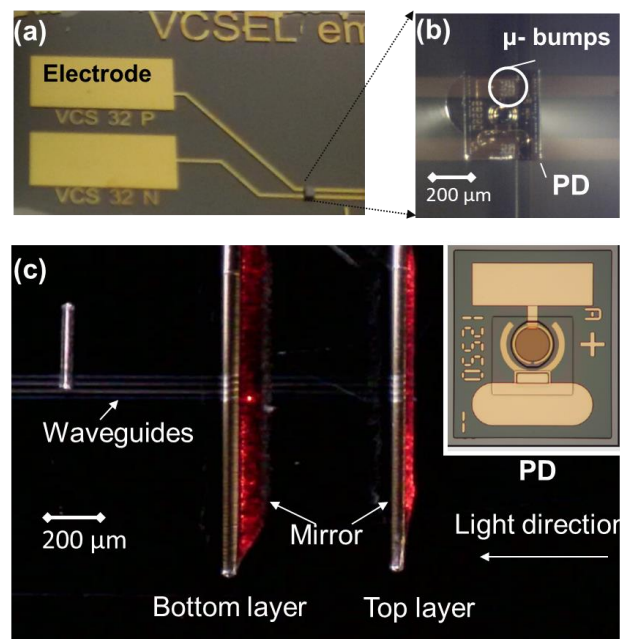


Figure 5.6 Flip chip bonding : (a) top view of a metalized resist sample; (b) μ -bumps and contact pads; (c) light coupling of two-layer integration

Figure 5.6 shows top view of a metalized resist sample with the photodiode bonded on top (a) and the zoom-in of photodiode revealing μ -bumps and contact pads (b). Figure 5.6(c) illustrates the two-layer integration results by the top view picture and a sample-guiding mode beside the PD layout in the inset. A single

channel InGaAs PIN photodiode from Albis (PDCS60T-XS) was used. Its dimensions are $300\ \mu\text{m} \times 350\ \mu\text{m}$ including a $60\text{-}\mu\text{m}$ optical aperture.

5.3 Characterization

Surface roughness, near field pattern of the guided light, insertion loss of the mirrors are characterized in this section.

5.3.1 Surface roughness by laser ablation

It was not possible to measure directly the flatness of the negative facet of the embedded mirror from top. Hence, the resist layer was peeled off from the wafer and subsequently flipped to reveal the surface of the negative facet.

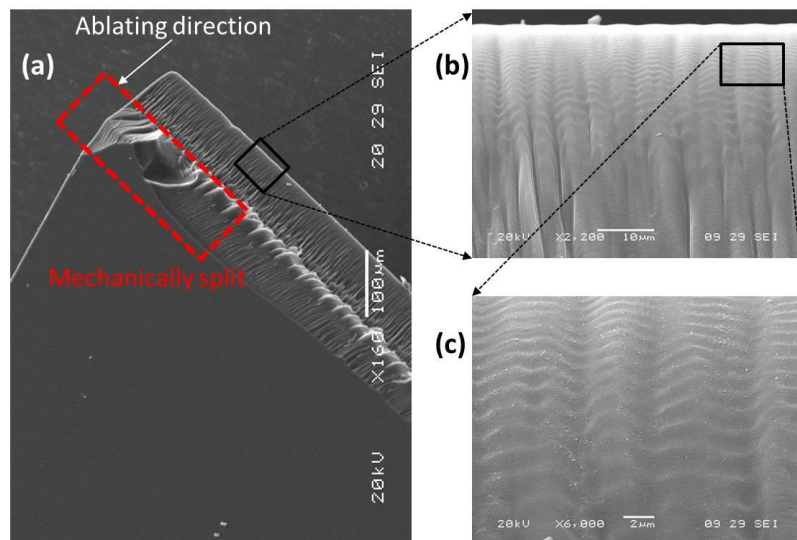


Figure 5.7 (a) Flatness of the negative facet of the TIR mirror captured through SEM micrograph and its zoom-ins (b, c)

Figure 5.7 shows the SEM photos of the negative facet of a mirror and its zoom-in micrographs. The mirror was made with 11 scanning steps at $600\ \mu\text{m/s}$ speed. The ablation depth is $60\ \mu\text{m}$; hence, the $100\text{-}\mu\text{m}$ resist layer has to be split mechanically. The whole resist layer could be ablated completely using 24 scanning steps. However, this changed the surface properties such as hardness and

roughness. It can be seen that the roughness at the bottom of the mirror is significantly increased. This increase is attributed to the interference between the laser beam and the reflected beam from the material surface.

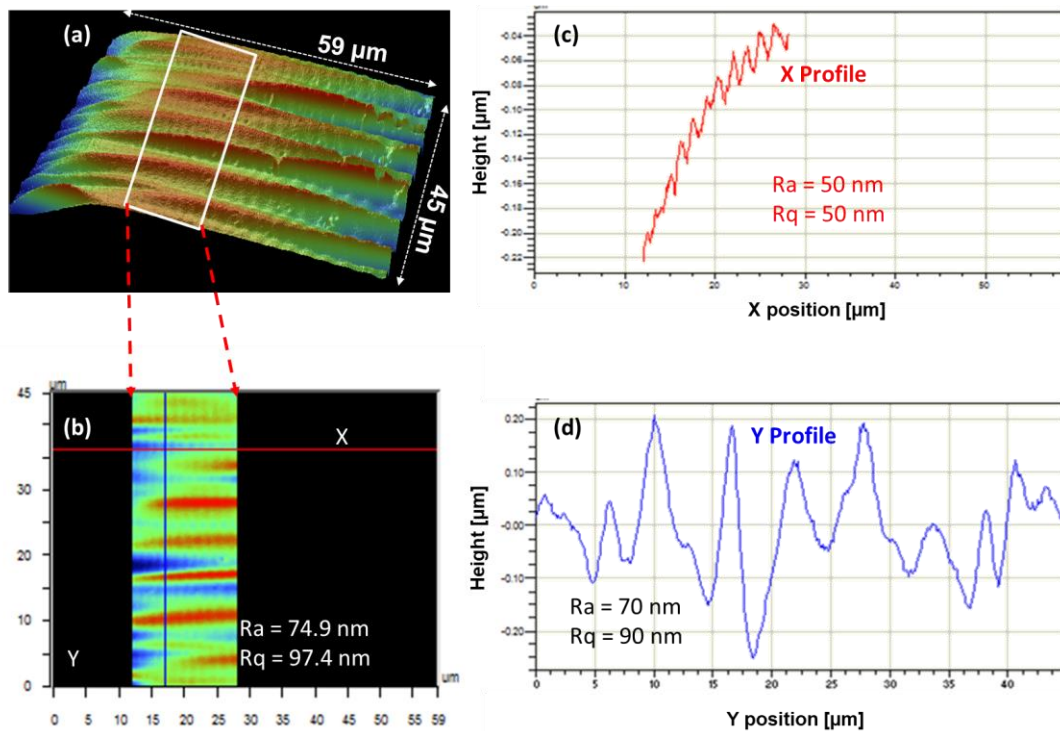


Figure 5.8 Surface roughness quantified by Wyco optical profiler. (a) the 3D surface profile of the negative facet; (b) L shape profile with a linear slope after the first 20 μm; roughness in vertical (c) and horizontal direction (d)

The mirror surface flatness was quantified using a non-contact optical profiler-Wyco NT8000. This optical profiler is a type of microscope in which light from a lamp is split into two paths by a beam splitter. One path directs the light onto the surface under test; the other path directs the light to a reference mirror. Reflections from the two surfaces are recombined and projected onto an array detector. When the path difference between the recombined beams is on the order of a few wavelengths of light or less interference can occur. The result is shown in Figure 5.8. Subfigure (a) plots the 3D surface profile of the negative facet while its vertical cross section (along ablation direction) shows an L shape profile with a linear slope after the first 20 μm. The next 20 μm (b) is the area of interest used as the mirror surface and was quantified in subfigure (c, d) with

average roughness of 50 nm and 70 nm in vertical and horizontal direction, respectively.

The roughness in both horizontal (scanning path) and vertical direction is periodic. These periodic modifications of the surface are accounted for the standing wave in vertical and stage movement in horizontal direction (scanning path).

5.3.2 Near field pattern

The light intensity profile after reflecting from the TIR mirror was measured to characterize the function of the mirror and prepare for the flip-chip bonding. Single mode light at 1310 nm was fed into a single mode fiber SMF28 and coupled to laser written waveguides. The optical signal reflected upwards to the top surface of the resist by the ablated mirror was captured by a multimode fiber with a 50- μm core size.

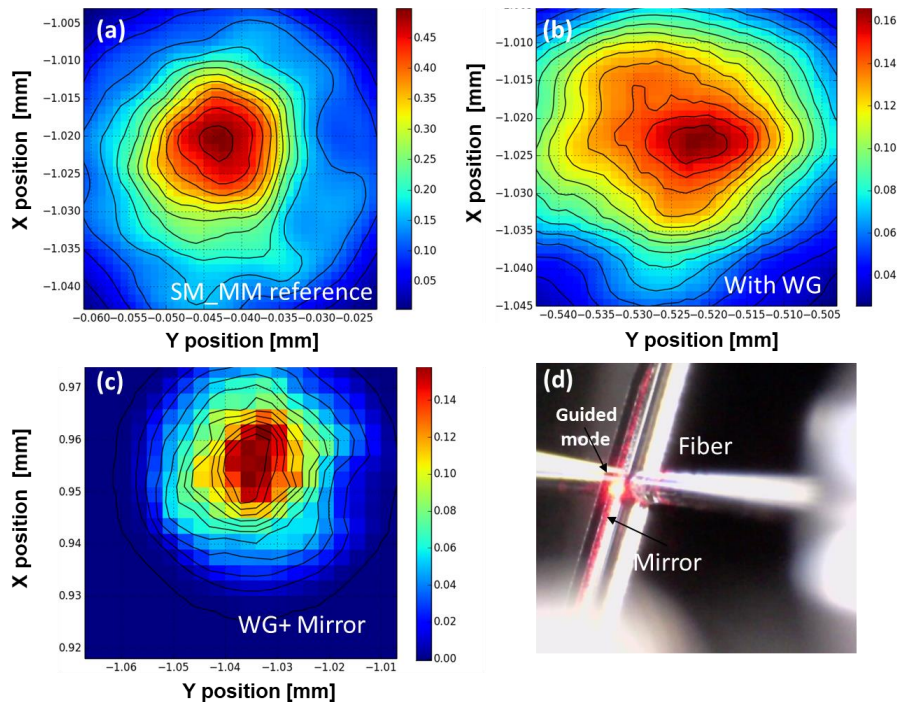


Figure 5.9 Near field scanning of the guided modes for (a) between single mode fiber and multimode fiber (SM-MM) as the reference, (b) device under test as a waveguide (c) device under test as a waveguide and a mirror; and the setup layout (d)

The intensity distribution measured by scanning the multimode fiber horizontally (in x and y) was compared to reference measurement of the SM fiber- MM fiber in direct coupling (Figure 5.9 a) and (Figure 5.9 (b)). The distance between the waveguide – mirror intersection and the resist top surface is in the range of 20 μm . The peak intensities at different vertical (z) position determined the direction information of the reflected beam for the optimization of the mirror. For these measurements, the distance between the waveguide – mirror intersection and the resist top surface is in the range of 20 μm .

The resulting near field pattern measured at + 5 μm from the resist surface in Figure 5.9 (c) shows that the reflected field was confined in the area with diameter less than 50 μm close to the resist surface. Hence, a photodiode with effective aperture larger than 50 μm is suitable as a receiver.

5.3.3 Insertion loss

In preparation for the insertion loss measurement, the mirror-coupling scheme was simulated using Lumerical (Lumerical Solutions, Inc.). Figure 5.10 shows the simulation setup and resulting guiding mode field and the insertion loss of the mirror. The simulation scheme shown in subfigure (a) includes a SMF 28 fiber at the input and a waveguide at the output. The mirror is located in between, and is 20 μm away from the fiber. In the scope of this simulation, a perfectly flat mirror was considered; the surface roughness of the mirror is hence neglected. The optional mismatch or alignment tolerance was also disregarded. Subfigure (b) shows the light intensity distributed along the optical path. The reflected light at the fiber-air-resist interfaces can be observed here. Subfigure (c) shows the near field pattern at the output of the waveguide. The resulting single mode signal at the output has a transmission loss of 20%, which is attributed to the reflection at the fiber-air-resist surfaces, the coupling loss between fiber and waveguide and the material absorption.

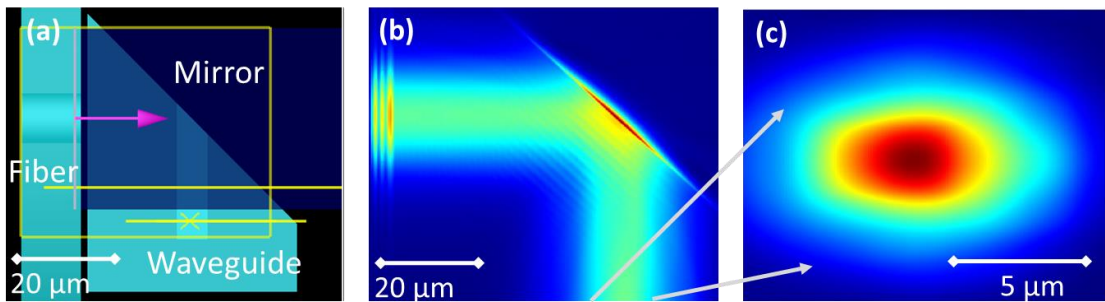


Figure 5.10 Simulation with Lumerical for the coupling loss between fiber and waveguide using total internal reflection mirror

Figure 5.11 shows the setup to measure the loss of the 45-degree mirrors implementing the optical link. One has to take into account that the precision of chip placing is limited to 5 μm which could result in a high insertion loss due to the small waveguide core size of 6.6 μm . In this work, we would like to demonstrate the concept shown in Figure 5.1 by investigating the insertion loss from the laser diode (sender-Tx) to the receiver side (Rx).

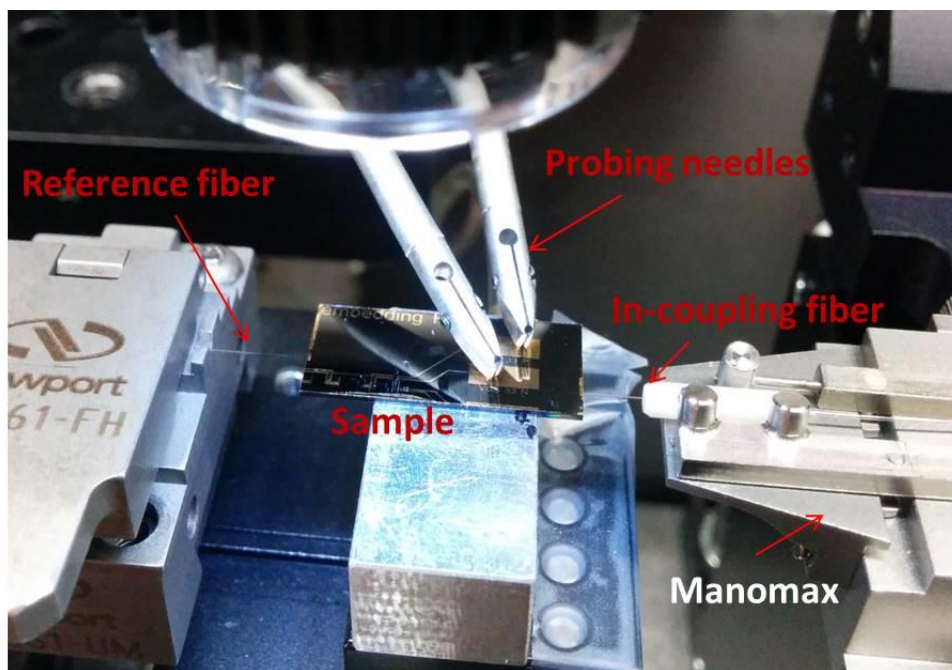


Figure 5.11 Insertion loss setup

The single mode fiber was mounted on the 6-axis NanoMax nano positioning stages for in-coupling to the waveguides. The multimode fiber was driven by a manual stage for recording the reference fiber-to-fiber measurement. An LDD TEC controller operated at 25 °C adjusted the laser source power at 1310 nm. Probes were launched on the Au pads for simultaneous recording of the electrical PD response. This results in the total loss (WG-fiber coupling loss+WG propagation loss+WG-mirror-PD loss) between fiber and PD of 3.5 dB

Chapter 6. Conclusion and outlook

6.1 Conclusions

Three dimensional free-form buried waveguides for board level interconnects have been realized by the marriage of a novel photosensitive polymer system and two-photon lithography. The polymer system comprises a host oligomer based on a bisphenol-A diglycidylether and an aliphatic guest monomer. External diffusion from the gaseous monomer into the host oligomer induced a sufficient and adjustable refractive index contrast for light guiding.

A high index contrast between the core and the cladding of 0.018 has been achieved. By adjusting the writing speed and laser intensity for the laser writing, it is possible to produce symmetrical square-shaped waveguides with adjustable core dimensions in the range from 5 μm to 20 μm . Fabricated waveguides exhibit a transmission loss of 0.37 dB/cm at 850 nm wavelength and 0.95 dB/cm at 1310 nm wavelength.

The fabricated waveguides indicate excellent thermal, mechanical and chemical stability. Baking samples up to 200 °C did not affect its near field pattern and transmission loss. Furthermore, sequential chemical baths with acetone and PGMEA did not detach the resist from the silicon wafer.

This fabrication technique allows fabricating waveguides in a layer thickness of 100 μm . This thickness limitation is due to structural instability at high temperature and long diffusion time. However, this fabrication process possesses various advantages over other waveguide fabrication methods. It requires only one layer of a single material. Its rapid prototyping possibility no longer involves masks, contact or any wet chemical process steps such as wet etching. The number of material layers and fabrication steps are independent of waveguide layers or

structural complexity. High index contrast offers a good confinement of the guided light inside the core.

Four by two waveguide arrays and three-core fan-outs were fabricated with compact pitch size of 25 μm , low cross talk of -34 dB and high precision. This process involves only a single layer, and need no stacking or alignment effort. Flexibility of three dimensional light guiding enabled optical functionalities such as 3-core optical fan-in/out.

Finally, we have shown the optoelectronic integration of the fabricated waveguides and the concept of decoupling pitch size vertically and horizontally. Two laser-ablated mirrors decouple two waveguide layers of a 25- μm pitch size to transmitter arrays or transceiver array with significantly larger pitch size of 250 μm .

6.2 Outlook

A potential application to demonstrate further the free-form possibility of 3D laser inscription is via 3D optical routers. This device could route optical signal to freely in 3D resulting in an arbitrary switching among input and output waveguides. Other optical functionalities such as 3D beam splitter, beam combiner could also be fabricated using this concept.

Built-in tapers at waveguide inputs and outputs would further increase the flexibility of the optical router with respect to coupling efficiency. Another potential application is printing Aerosol ink on the resist surface as contact pads for optoelectronic integration of buried waveguides. Micro mirrors were also ablated through the ink showing similar performance compared to image reversal lithography.

Bibliography

1. X. Wang, A. V. Vasilakos, M. Chen, Y. Liu, and T. T. Kwon, "A Survey of Green Mobile Networks: Opportunities and Challenges," *Mob. Networks Appl.* **17**, 4–20 (2012).
2. W. Van Heddeghem, S. Lambert, B. Lannoo, D. Colle, M. Pickavet, and P. Demeester, "Trends in worldwide ICT electricity consumption from 2007 to 2012," *Comput. Commun.* **50**, 64–76 (2014).
3. D. a. B. Miller, "Rationale and challenges for optical interconnects to electronic chips," *Proc. IEEE* **88**, 728–749 (2000).
4. M. Chateauneuf, M. B. Venditti, E. Laprise, J. Faucher, K. Razavi, F. Thomas-Dupuis, A. G. Kirk, D. V. Plant, T. Yamamoto, J. A. Trezza, and W. Luo, "Design, implementation, and characterization of a 2D bidirectional free-space optical link," in R. A. Lessard and T. V. Galstian, eds. (*International Society for Optics and Photonics*, 2000), pp. 530–538.
5. D. V. Plant, M. B. Venditti, E. Laprise, J. Faucher, K. Razavi, M. teauneuf, A. G. Kirk, J. S. Ahearn, A. Member, E. Laprise, J. Faucher, K. Razavi, M. Châteauneuf, A. G. Kirk, and J. S. Ahearn, "256-Channel Bidirectional Optical Interconnect Using VCSELs and Photodiodes on CMOS," *J. Light. Technol.* **19**, 1093- (2001).
6. H.-S. Lee, J.-Y. Park, S.-M. Cha, S.-S. Lee, G.-S. Hwang, and Y.-S. Son, "Ribbon plastic optical fiber linked optical transmitter and receiver modules featuring a high alignment tolerance.," *Opt. Express* **19**, 4301–4309 (2011).
7. A. Neyer, B. Wittmann, and M. Johnck, "Plastic-optical-fiber-based parallel optical interconnects," *IEEE J. Sel. Top. Quantum Electron.* **5**, 193–200 (1999).

8. J. S. Kim and J. J. Kim, "Stacked polymeric multimode waveguide arrays for two-dimensional optical interconnects," *J. Light. Technol.* **22**, 840–844 (2004).
9. U. Streppel, "New wafer-scale fabrication method for stacked optical waveguide interconnects and 3D micro-optic structures using photoresponsive (inorganic – organic hybrid) polymers," **21**, 475–483 (2002).
10. E. Zraggen, I. M. Soganci, F. Horst, A. La Porta, R. Dangel, B. J. Offrein, S. A. Snow, J. K. Young, B. W. Swatowski, C. M. Amb, O. Scholder, R. Broennimann, U. Sennhauser, and G. Bona, "Laser Direct Writing of Single-Mode Polysiloxane Optical Waveguides and Devices," *J. Light. Technol.* **32**, 3036–3042 (2014).
11. Y.-H. Pao and P. M. Rentzepis, "Laser-induced production of free radicals in organic compounds," *Appl. Phys. Lett.* **6**, 93–95 (1965).
12. J. Fischer and M. Wegener, "Three-dimensional direct laser writing inspired by stimulated-emission-depletion microscopy [Invited]," *Opt. Mater. Express* **1**, 614 (2011).
13. R. R. Gattass and E. Mazur, "Femtosecond laser micromachining in transparent materials," *Nat. Photonics* (2008).
14. C. Koos, J. Leuthold, W. Freude, N. Lindenmann, S. Koeber, G. Balthasar, J. Hoffmann, T. Hoose, P. Huebner, D. Hillerkuss, and R. Schmogrow, "Photonic wire bonding: connecting nanophotonic circuits across chip boundaries," in *SPIE MOEMS-MEMS*, G. von Freymann, W. V. Schoenfeld, and R. C. Rumpf, eds. (International Society for Optics and Photonics, 2013), p. 86130W.
15. A. Arriola, S. Gross, N. Jovanovic, N. Charles, P. G. Tuthill, S. M. Olaizola, A. Fuerbach, and M. J. Withford, "Low bend loss waveguides enable compact , efficient 3D photonic chips," *Opt. Express* **21**, 2978–2986 (2013).

16. S. Nolte, M. Will, J. Burghoff, and A. Tuennermann, "Femtosecond waveguide writing: a new avenue to three-dimensional integrated optics," *Appl. Phys. A Mater. Sci. Process.* **77**, 109–111 (2003).
17. E. D. Moore, A. C. Sullivan, and R. R. McLeod, "Three-dimensional waveguide arrays via projection lithography into a moving photopolymer," in *Proc. of SPIE*, S. Orlic, ed. (2008), Vol. 7053, pp. 705309-705309–7.
18. N. Lindenmann, G. Balthasar, D. Hillerkuss, R. Schmogrow, M. Jordan, W. Freude, and C. Koos, "Photonic wire bonding : a novel concept for chip- scale interconnects," **20**, 17667–17677 (2012).
19. M. R. Billah, T. Hoose, T. Onanuga, N. Lindenmann, P. Dietrich, T. Wingert, M. L. Goedecke, A. Hofmann, U. Troppenz, A. Sigmund, M. Möhrle, W. Freude, and C. Koos, "Multi-Chip Integration of Lasers and Silicon Photonics by Photonic Wire Bonding," in *CLEO: 2015* (OSA, 2015), p. STu2F.2.
20. J. Ishihara, K. Komatsu, O. Sugihara, and T. Kaino, "Fabrication of three-dimensional calixarene polymer waveguides using two-photon assisted polymerization," *Appl. Phys. Lett.* **90**, 033511 (2007).
21. V. Schmidt, L. Kuna, V. Satzinger, R. Houbertz, G. Jakopic, and G. Leising, "Application of two-photon 3D lithography for the fabrication of embedded ORMOCER® waveguides," in *Proc. of SPIE*, L. A. Eldada and E.-H. Lee, eds. (2007), Vol. 6476, p. 64760P.
22. R. Kinoshita, D. Sukanuma, and T. Ishigure, "Accurate interchannel pitch control in graded- index circular-core polymer parallel optical waveguide using the Mosquito method," *Opt. Express* **22**, 8426–8437 (2014).
23. Y. Vlasov and S. McNab, "Losses in single-mode silicon-on-insulator strip waveguides and bends," *Opt. Express* **12**, 1622–1631 (2004).
24. C. Koos, P. Vorreau, T. Vallaitis, P. Dumon, W. Bogaerts, R. Baets, B.

- Esembeson, I. Biaggio, T. Michinobu, F. Diederich, W. Freude, and J. Leuthold, "All-optical high-speed signal processing with silicon-organic hybrid slot waveguides," *Nat. Photonics* **3**, 216–219 (2009).
25. G. Carnicella, C. Ciminelli, P. Thijs, P. J. Veldhoven, H. Ambrosius, M. Smit, R. Nagarajan, C. H. Joyner, R. P. Jr Schneider, J. S. Bostak, T. Butrie, A. G. Dentai, V. G. Dominic, P. W. Evans, M. Kato, M. Kauffman, D. J. H Lambert, S. K. Mathis, A. Mathur, R. H. Miles, M. L. Mitchell, M. J. Missey, S. Murthy, A. C. Nilsson, F. H. Peters, S. C. Pennypacker, J. L. Pleumeekers, R. A. Salvatore, R. K. Schlenker, R. B. Taylor, T. Huan-Shang, M. F. Van Leeuwen, J. Webjorn, M. Ziari, D. Perkins, J. Singh, S. G. Grubb, M. S. Reffle, D. G. Mehuys, F. A. Kish, and D. F. Welch, "Low-loss passive waveguides in a generic InP foundry process via local diffusion of zinc," (n.d.).
 26. H. Inoue, K. Hiruma, K. Ishida, T. Asai, and H. Matsumura, "Low loss GaAs optical waveguides," *IEEE Trans. Electron Devices* **32**, 2662–2668 (1985).
 27. R. J. Deri and E. Kapon, "Low-loss III-V semiconductor optical waveguides," *IEEE J. Quantum Electron.* **27**, 626–640 (1991).
 28. D. Yoon Oh, K. Y. Yang, C. Fredrick, G. Ycas, S. A. Diddams, and K. J. Vahala, "Coherent ultra-violet to near-infrared generation in silica ridge waveguides," *Nat. Commun.* **8**, 13922 (2017).
 29. J. Chiles, M. Malinowski, A. Rao, S. Novak, K. Richardson, and S. Fathpour, "Low-loss, submicron chalcogenide integrated photonics with chlorine plasma etching," *Appl. Phys. Lett.* **106**, 111110 (2015).
 30. B. J. Eggleton, B. Luther-Davies, and K. Richardson, "Chalcogenide photonics," *Nat. Photonics* **5**, 141–148 (2011).
 31. L. Arizmendi, "Photonic applications of lithium niobate crystals," *Phys. status solidi* **201**, 253–283 (2004).
 32. H. Sieber, H. Boehm, U. Hollenbach, J. Mohr, U. Ostrzinski, K. Pfeiffer, M.

- Szczurowski, and W. Urbanczyk, "Low-loss single mode light waveguides in polymer," in *Proc. SPIE 8431, Silicon Photonics and Photonic Integrated Circuits III, 84311R* (International Society for Optics and Photonics, 2012), p. 84311R.
33. H. Ma, A. K.-Y. Jen, and L. R. Dalton, "Polymer-Based Optical Waveguides: Materials, Processing, and Devices," *Adv. Mater.* **14**, 1339–1365 (2002).
 34. J. Liu, G. Xu, F. Liu, I. Kityk, X. Liu, and Z. Zhen, "Recent advances in polymer electro-optic modulators," *RSC Adv.* **5**, 15784–15794 (2015).
 35. A. Liu, Z. Zhang, D. de Felipe, N. Keil, and N. Grote, "Power-Efficient Thermo-Optic Tunable Filters Based on Polymeric Waveguide Bragg Gratings," *IEEE Photonics Technol. Lett.* **26**, 313–315 (2014).
 36. Y. Jiang, Z. Da, F. Qiu, Y. Guan, and G. Cao, "Fabrication of chromophore molecule-linked azo polymer as waveguide material of polymeric thermo-optic digital optical switch," *J. Nonlinear Opt. Phys. Mater.* **26**, 1750032 (2017).
 37. N. Keil, "Thermo-optic devices on polymer platform," *Opt. Commun.* **362**, 101–114 (2016).
 38. J.-M. Brosi, C. Koos, L. C. Andreani, M. Waldow, J. Leuthold, and W. Freude, "High-speed low-voltage electro-optic modulator with a polymer-infiltrated silicon photonic crystal waveguide," *Opt. Express* **16**, 4177 (2008).
 39. P. S. Westbrook, B. J. Eggleton, R. S. Windeler, A. Hale, T. A. Strasser, and G. L. Burdge, "Cladding-mode resonances in hybrid polymer-silica microstructured optical fiber gratings," *IEEE Photonics Technol. Lett.* **12**, 495–497 (2000).
 40. Y. Enami, C. T. DeRose, C. Loychik, D. Mathine, R. A. Norwood, J. Luo, A. K.-Y. Jen, and N. Peyghambarian, "Low half-wave voltage and high electro-optic

- effect in hybrid polymer/sol-gel waveguide modulators," *Appl. Phys. Lett.* **89**, 143506 (2006).
41. Y. Enami, G. Meredith, N. Peyghambarian, M. Kawazu, and A. K.-Y. Jen, "Hybrid electro-optic polymer and selectively buried sol-gel waveguides," *Appl. Phys. Lett.* **82**, 490–492 (2003).
 42. A. Boisen, D. A. Zauner, J. Hübner, and M. Nordström, "Single-Mode Waveguides With SU-8 Polymer Core and Cladding for MOEMS Applications," *J. Light. Technol.* Vol. 25, Issue 5, pp. 1284-1289 **25**, 1284–1289 (2007).
 43. E. Fiedler, N. Haas, and T. Stieglitz, "Suitability of SU-8, EpoClad and EpoCore for flexible waveguides on implantable neural probes," in *2014 36th Annual International Conference of the IEEE Engineering in Medicine and Biology Society* (IEEE, 2014), pp. 438–441.
 44. T. Korhonen, N. Salminen, A. Kokkonen, N. Masuda, and M. Karppinen, "Multilayer single-mode polymeric waveguides by imprint patterning for optical interconnects," **8991**, 899103 (2014).
 45. L. Eldada, S. Member, and L. W. Shacklette, "Advances in Polymer Integrated Optics," **6**, 54–68 (2000).
 46. B. L. Booth, "Low loss channel waveguides in polymers," *J. Light. Technol.* **7**, 1445–1453 (1989).
 47. G. Van Steenberge, N. Hendrickx, E. Bosman, J. Van Erps, H. Thienpont, and P. Van Daele, "Laser ablation of parallel optical interconnect waveguides," *IEEE Photonics Technol. Lett.* **18**, 1106–1108 (2006).
 48. A. Elmogi, E. Bosman, J. Missinne, and G. Van Steenberge, "Comparison of epoxy- and siloxane-based single-mode optical waveguides defined by direct-write lithography," *Opt. Mater. (Amst)*. **52**, 26–31 (2016).
 49. S. S. Zakariyah, P. P. Conway, D. A. Hutt, D. R. Selviah, K. Wang, H. Baghsiahi, J.

- Rygate, J. Calver, and W. Kandulski, "Polymer Optical Waveguide Fabrication Using Laser Ablation," (2009).
50. V. Prajzler, P. Hyps, R. Mastera, and P. Nekvindova, "Properties of siloxane based optical waveguides deposited on transparent paper and foil," *Radioengineering* **25**, 230–235 (2016).
 51. Y. Ichihashi, D. Cristea, M. Kusko, and D. Rabus, "Integrated Silicon Photodiodes with Polymer (PMMA) Waveguides for Optical Interconnections and Sensing Applications," *Technology* 3–4 (2006).
 52. P. I. Okagbare, J. M. Emory, P. Datta, J. Goettert, and S. A. Soper, "Fabrication of a cyclic olefin copolymer planar waveguide embedded in a multi-channel poly(methyl methacrylate) fluidic chip for evanescent excitation," *Lab Chip* **10**, 66–73 (2010).
 53. B. S. and K. P. R. Moosburger, E. Brose, G. Fischbeck, C. Kostrzewa, "Robust digital optical switch based on a novel patterning technique for "oversized" polymer rib waveguides," in *Proceedings of European Conference on Optical Communication, Oslo, Norway*, (Telenor R & D, 1996), pp. 67–70, vol.2.
 54. "micro resist technology GmbH," <http://www.microresist.de>.
 55. Avogadro, "Avogadro," http://avogadro.cc/wiki/Main_Page.
 56. J. Zhang, M. B. Chan-Park, and C. M. Li, "Network properties and acid degradability of epoxy-based SU-8 resists containing reactive gamma-butyrolactone," *Sensors Actuators B Chem.* **131**, 609–620 (2008).
 57. T. a Anhoj, A. M. Jorgensen, D. a Zauner, and J. Hübner, "The effect of soft bake temperature on the polymerization of SU-8 photoresist," *J. Micromechanics Microengineering* **16**, 1819–1824 (2006).
 58. D. M. Altpeter, "1 Description of SU-8," 2–5 (2005).

59. X. C. Tong Ph.D, *Advanced Materials for Integrated Optical Waveguides* (2014), Vol. 46.
60. S. Keller, G. Blagoi, M. Lillemose, D. Haefliger, and A. Boisen, "Processing of thin SU-8 films," *J. Micromechanics Microengineering* **18**, 125020 (2008).
61. H. H. D. H. H. D. Nguyen, U. Hollenbach, U. Ostrzinski, K. Pfeiffer, S. Hengsbach, and J. Mohr, "Freeform three-dimensional embedded polymer waveguides enabled by external-diffusion assisted two-photon lithography," *Appl. Opt.* **55**, 1906–1912 (2016).
62. P. Dumon, W. Bogaerts, V. Wiaux, J. Wouters, S. Beckx, J. Van Campenhout, D. Taillaert, B. Luyssaert, P. Bienstman, D. Van Thourhout, and R. Baets, "Low-Loss SOI Photonic Wires and Ring Resonators Fabricated With Deep UV Lithography," *IEEE Photonics Technol. Lett.* **16**, 1328–1330 (2004).
63. T. Akiyama, K. Inagaki, T. Ohira, and M. Hikita, "Two-dimensional optical signal-processing beamformer using multilayer polymeric optical waveguide arrays," *IEEE Trans. Microw. Theory Tech.* **49**, 2055–2061 (2001).
64. A. Ródenas, G. Martin, B. Arezki, N. Psaila, G. Jose, A. Jha, L. Labadie, P. Kern, A. Kar, and R. Thomson, "Three-dimensional mid-infrared photonic circuits in chalcogenide glass," **37**, 392–394 (2012).
65. a M. Kowalevicz, V. Sharma, E. P. Ippen, J. G. Fujimoto, and K. Minoshima, "Three-dimensional photonic devices fabricated in glass by use of a femtosecond laser oscillator.," *Opt. Lett.* **30**, 1060–2 (2005).
66. M. W. Grabowski, A. C. Sullivan, and R. R. McLeod, "3D Direct-Write Waveguides in Diffusion Photopolymers," *Integr. Photonics Res. Appl. ITuD5* (2006).
67. "Nanoscribe GmbH," <http://www.nanoscribe.de/>.
68. H.-B. Sun, M. Maeda, K. Takada, J. W. M. Chon, M. Gu, and S. Kawata, "Experimental investigation of single voxels for laser nanofabrication via

- two-photon photopolymerization," *Appl. Phys. Lett.* **83**, 819–821 (2003).
69. H. Sun and S. Kawata, "Two-Photon Photopolymerization and 3D Lithographic Microfabrication," 169–274 (2004).
 70. W. H. Teh, U. Dürig, U. Drechsler, C. G. Smith, and H.-J. Güntherodt, "Effect of low numerical-aperture femtosecond two-photon absorption on (SU-8) resist for ultrahigh-aspect-ratio microstereolithography," *J. Appl. Phys.* **97**, 054907 (2005).
 71. M. J. Nasse and J. C. Woehl, "Realistic modeling of the illumination point spread function in confocal scanning optical microscopy.," *J. Opt. Soc. Am. A. Opt. Image Sci. Vis.* **27**, 295–302 (2010).
 72. T. Stichel, B. Hecht, R. Houbertz, and G. Sextl, "Compensation of spherical aberration influences for two-photon polymerization patterning of large 3D scaffolds," *Appl. Phys. A* **121**, 187–191 (2015).
 73. Q. Sun, H. Jiang, Y. Liu, Y. Zhou, H. Yang, and Q. Gong, "Effect of spherical aberration on the propagation of a tightly focused femtosecond laser pulse inside fused silica," *J. Opt. A Pure Appl. Opt.* **7**, 655–659 (2005).
 74. H. Sun and S. Kawata, *Nmr - 3d Analysis - Photopolymerization* (Springer, 2004).
 75. M. P. Larsson and M. M. Ahmad, "Improved polymer–glass adhesion through micro-mechanical interlocking," *J. Micromechanics Microengineering* **16**, S161–S168 (2006).
 76. J.-P. Fouassier and J. F. Rabek, *Radiation Curing in Polymer Science and Technology* (Elsevier Applied Science, 1993).
 77. R. Infuehr, N. Pucher, C. Heller, H. Lichtenegger, R. Liska, V. Schmidt, L. Kuna, A. Haase, and J. Stampfl, "Functional polymers by two-photon 3D lithography," *Appl. Surf. Sci.* **254**, 836–840 (2007).

78. R. A. Norwood, R. Gao, J. Sharma, and C. C. Teng, "Sources of loss in single-mode polymer optical waveguides," in *SPIE*, R. A. Norwood, ed. (International Society for Optics and Photonics, 2001), pp. 19–28.
79. H. H. D. H. H. D. Nguyen, U. Hollenbach, S. Pfirrmann, U. Ostrzinski, K. Pfeiffer, S. Hengsbach, and J. Mohr, "Photo-structurable polymer for interlayer single-mode waveguide fabrication by femtosecond laser writing," *Opt. Mater. (Amst)*. **66**, 110–116 (2017).
80. T. Findaldy, B. Chen, and D. Booher, "Single-mode integrated-optical polarizers in LiNbO₃ and glass waveguides," **8**, 641–643 (1983).
81. Y. Fukada, "Probability density function of polarization dependent loss (PDL) in optical transmission system composed of passive devices and connecting fibers," *J. Light. Technol.* **20**, 953–964 (2002).
82. N. Iizuka, K. Kaneko, and N. Suzuki, "Polarization dependent loss in III-nitride optical waveguides for telecommunication devices," *J. Appl. Phys.* **99**, (2006).
83. Y. H. Min, M. H. Lee, and J. Y. Do, "Polarization dependent loss in polymeric rib channel waveguide," *IEEE Photonics Technol. Lett.* **12**, 1483–1485 (2000).
84. K. S. Chiang, S. Y. Cheng, H. P. Chan, Q. Liu, K. P. Lor, and C. K. Chow, "Realization of Polarization-Insensitive Optical Polymer Waveguide Devices," **1**, 644–650 (2006).
85. T. Watanabe, N. Ooba, S. Hayashida, T. Kurihara, and S. Imamura, "Polymeric Optical Waveguide Circuits," *J. Light. Technol.* **16**, 1049–1055 (1998).
86. J. Kobayashi, T. Matsuura, Y. Hida, S. Sasaki, and T. Maruno, "Fluorinated polyimide waveguides with low polarization-dependent loss and their applications to thermo-optic switches," *J. Light. Technol.* **16**, 1024–1029 (1998).
87. G. M. W. David L. Favin, Bruce M. Nyman, "System and method for measuring polarization dependent loss," (November 23, 1993).

88. M. Sagues, M. Pérez, and A. Loayssa, "Measurement of polarization dependent loss, polarization mode dispersion and group delay of optical components using swept optical single sideband modulated signals," 2008 IEEE Int. Meet. Microw. Photonics jointly held with 2008 Asia-Pacific Microw. Photonics Conf. MWP2008/APMP2008 **16**, 314–317 (2008).
89. B. L. Heffner, "Deterministic, analytically complete measurement of polarization-dependent transmission through optical devices," IEEE Photonics Technol. Lett. **4**, 451–454 (1992).
90. General Photonics Corporation, *Application Note for PDL Measurement* (n.d.).
91. K. L. Kruse and C. T. Middlebrook, "Fan-out routing and optical splitting techniques for compact optical interconnects using single-mode polymer waveguides," J. Mod. Opt. **62**, S1–S10 (2014).
92. D. V Plant and A. G. Kirk, *Optical Interconnects at the Chip and Board Level: Challenges and Solutions* (2000).
93. J. W. Jang, P. G. Kim, K. N. Tu, D. R. Frear, and P. Thompson, "Solder reaction-assisted crystallization of electroless Ni–P under bump metallization in low cost flip chip technology," J. Appl. Phys. (1999).
94. K. N. Tu, H.-Y. Hsiao, and C. Chen, "Transition from flip chip solder joint to 3D IC microbump: Its effect on microstructure anisotropy," Microelectron. Reliab. **53**, 2–6 (2013).
95. J. Jordan, "Gold stud bump in flip-chip applications," in *27th Annual IEEE/SEMI International Electronics Manufacturing Technology Symposium* (IEEE, n.d.), pp. 110–114.
96. Y. Bessho, Y. Tomura, Y. Hakotani, M. Tsukamoto, T. Ishida, and K. Omoya, "A Stud-bump-bonding Technique For High Density Multi-chip-module," in *Proceedings of Japan International Electronic Manufacturing Technology*

Symposium (IEEE, n.d.), pp. 362–365.

97. Minjae Lee, Min Yoo, Jihee Cho, Seungki Lee, Jaedong Kim, Choonheung Lee, Daebyoung Kang, C. Zwenger, and R. Lanzone, "Study of interconnection process for fine pitch flip chip," in *2009 59th Electronic Components and Technology Conference* (IEEE, 2009), pp. 720–723.
98. J.-W. Yoon, H.-S. Chun, and S.-B. Jung, "Reliability evaluation of Au–20Sn flip chip solder bump fabricated by sequential electroplating method with Sn and Au," *Mater. Sci. Eng. A* **473**, 119–125 (2008).
99. D. Manassis, R. Patzelt, A. Ostmann, R. Aschenbrenner, and H. Reichl, "Technical challenges of stencil printing technology for ultra fine pitch flip chip bumping," *Microelectron. Reliab.* **44**, 797–803 (2004).
100. K. S. Kaur and G. Van Steenberge, "Laser-induced Forward Transfer for Flip-chip Packaging of Single Dies," *J. Vis. Exp.* 1–10 (2015).
101. R. Feng and R. J. Farris, "Influence of processing conditions on the thermal and mechanical properties of SU8 negative photoresist coatings," *J. Micromechanics Microengineering* **13**, 80–88 (2002).

Appendix

Fabrication notes

Impact of *structure thickness and structure position on instability*: To analyze the impact of the structure thickness and structure position on its stability, waveguide groups with varying thickness from 2.5 μm to 8 μm were written on the same wafer and baked following a certain PEB recipe. The wafer thicknesses are approximately 400 μm . Each group includes two waveguides written with the same parameters but at different depth. The bottom one is 100 μm closer to the wafer than the top one. Altering laser power, number of lines and distance between the lines lead to an increased waveguide thickness from group 1 to group 6. Repeating this experiment with different baking temperatures and baking time lead to the same conclusion. The thinner the waveguide cores or the closer they are to the air surface (i.e. further away from the wafer), the higher structure instability is observed. Analogous experiments also showed increasing bends and drifting with larger wafer thickness.

We attribute all these bends and drifting to the inner stress and material softening during thermal process, in particular during the cooling down process. By reducing the PEB temperature below the glass transition temperature of the photopolymer matrix ($T_g = 55^\circ\text{C}$), e.g. 40°C , and the extension of the baking time to more than 1 hour, this instability was avoided. Although the impact of the structure thickness is much less significant than the impact of the baking temperature and time, the core sizes were kept larger than 5 μm . This nullifies the micro-bends at PEB lower than T_g and matches the waveguide designs. At this point, samples with 400- μm thick wafers were chosen to continue with the next step in the fabrication flow – external diffusion.

Trajectory

Due to instability of the material and nanoscribe machine, this measurement was not be able to confirm. The next step is to improve the transition loss by using waveguide trajectories following B-spline interpolation. As shown in the figure

below, compared to cubic and cosine, the B-spline smoothing possesses the smallest change of radius along the trajectory

Waveguides with trajectories following B-spline, cosine, cubic interpolations were fabricated. However, the reproducibility of the material did not allow us to come to a proper conclusion on the interpolation impact.

Failed Approaches

Before coming to a conclusion that the external diffusion concept is only suitable for layers of less than 100 μm thickness to maintain the structural stability, various approaches were carried out to fix the structural stability at higher thicknesses, such as 400 μm or 200 μm . All the diffusions done in these trials were at higher than ambient temperature that is between 35 $^{\circ}\text{C}$ to 70 $^{\circ}\text{C}$.

Varying the solvent concentration

This attempt was to reduce the thermal-induced stress and to increase the material stiffness by tuning the solvent concentration in the resist. Varying the prebake temperature and duration adjusted the solvent concentration between **2 wt. % and 12 wt. %**. Qualitatively, higher concentration of solvent lowers the required PEB temperature but produce more instability while lower concentration increased the stiffness but hardly changed HaSS.

PEB at lower temperatures

Post exposure baking for SU-8 was recommended to keep higher than the glass transition temperature $T_g = 55\text{ }^{\circ}\text{C}$ [60,101]. However, as proven in Figure 3.10, the higher PEB temperature produced higher bends and drifting of the written waveguides. Hence, our approach is to eliminate inner stress during PEB process to improve the structural stability during the external diffusion.

The first result confirmed a high degree of cross linking with PEB at 50 $^{\circ}\text{C}$ for 10 minutes, i.e. lower than T_g . After developing the written structure in PGMEA following this PEB, the exposure region was not resolved. There were no typical signs of under exposure such as holes or cracks in the exposed volume. As a further step, PEB at 40 $^{\circ}\text{C}$ for 60 minutes were tested and showed no visible bends or drifting. Writing laser power must increase 10% in this case to achieve the same feature size. However, the impact on HaSS was insignificant. Strong bends and drifting still occurred after diffusion. Without PEB after writing, waveguide core

dimensions shrank to 3 μm instead of 6 μm . In this case, the cores were cured during flood exposure and hard bake. It also means the cores were cross-linked during the laser writing to a certain degree that was enough to stop the monomer diffusing into the cores.

Pre-solidification with prebake at high temperature

The idea was to solidify the resist prior to the diffusion process by carrying out a second prebake at higher temperature than 90 °C. As a consequence, the structure appeared significantly more stable with second prebakes between 90 °C and 120 °C. Only small bends occurred and the drifting was negligible. The material in this case was less sensitive. I.e. qualitatively, higher laser power was required to achieve the same feature size as before.

For samples undergoing second prebake at a temperature higher than 120 °C, the diffusion depth was hardly observed after diffusion. The reason was the beginning of thermal cross-linking the resist at temperature close to 140 °C.

Partially crosslinking

Another analogous idea was to partially cross link the resist prior to diffusion process by UV flood exposure with low dose. With sample thickness of 400 μm , an exposure dose of 2.5 J/ cm^2 at 365 nm was sufficient for curing the whole resist layer. Hence, various exposure doses within 0.018 J/ cm^2 – 0.8 J/ cm^2 (equivalent to 1 % to 32% of full dose) were applied in both cases, before and after laser writing. Furthermore, by understanding that the cross-linking of the written waveguide cores and pre-flood exposed cladding will occurred during the diffusion process at 70 °C, the post exposure baking process was omitted for some test samples as well.

As a consequence, at a dose of 200, 400 and 800 mJ/ cm^2 , though the waveguide cores were clearly visible, neither HaSS nor diffusion into the resist layer was observed. The gaseous monomer is condensed on the resist surface after cooling in the chamber and can be easily removed without changing the layer surface.

If the dosage is too low, only a cross-linking of the surface is caused by absorption. At a dose of 45 and 72 mJ/ cm², the surface showed typical furrows. At a dose of 18 mJ/ cm², a flat and clean surface was present. However, diffusion of gaseous monomer was not observed in this case.

Framing method

The approach was to cure completely the outer part of the wafer, leaving a window at the wafer center for laser writing. Two scenarios were tested. Waveguides were written in the free space of the writing window to avoid free flowing, or were anchored to the cured frame with expectation to hold tight two ends of the structures and avoid the drifting. Hand-made mask utilizing Kapton polyimide foil as absorbing material was built to form the writing window. To minimize inner-layer tension, the post exposure baking steps to cure the frame and written waveguides were combined. Samples underwent the sequence of flood exposure, laser writing, baking and finally external diffusion.

Microscopic photos of the samples after diffusion and hardbake revealed improvement of HaSS but it was still not completely overcome, as shown in the figure below. Thanks to the anchoring, bends and drifting were significantly reduced.

Another benefit of framing method was quantifying the swelling of the diffused resist by comparing the thickness of the frame and the writing window after external diffusion. Since monomer could not diffuse into the frame region, swelling did not occur there.

List of figures

Figure 1.1 The concept of the 3D optical router to perform all the optical interconnections on board and in three dimensions equipped with vertical-cavity surface-emitting lasers (VCSEL) and mirrors.	15
Figure 2.1 The principles of external diffusion (left) and internal diffusion (left)	21
Figure 2.2 Annotated molecular structure of the host components: oligomer's solvent, photoinitiator (PAG) and photoinitiator's solvent [<i>Credit: SU8 Purnima Polamarasetty, Uwe Hollenbach</i>]	23
Figure 2.3 Molecular structure host oligomer and its crosslink schemes annotated in 3D using Avogadro molecule editor: Two epoxy oligomers were shown with an octafunctional unit of bisphenol-A diglycidylether containing glycidyl groups, benzene rings and isopropyl group. Intramolecular crosslink, intermolecular crosslink and CH ₂ -methylene bridge were illustrated.....	24
Figure 2.4 Molecular structure of an exemplary guest monomer (left) and crosslink between host oligomer, GBL solvent and monomers; 1,2: crosslinks with GBL; 3,4 crosslinks with monomers	26
Figure 2.5 Refractive index of an epoxide oligomer solution as a function of the solids content: The refractive index was experimentally determined using an Abbe refractometer up to an oligomer content of 68%. The value of the refractive index for the pure epoxy oligomer ($n_D = 1.5998$) was determined by extrapolation of the straight line (dashed line).....	27
Figure 2.6: Absorption spectrum of the uncured liquid photopolymer: extremely low absorption at 780 nm for local 2-photon absorption and high absorption at 390 nm for UV cure one-photon absorption. Material transmission loss at 850 nm, 1310nm and 1550 nm are 0.04 dB/cm 0.30 dB/cm and 0.85 dB/cm respectively.	28
Figure 2.7 Refractive indices of the resist measured at 1.540, 0.988, 0.594, 0.450 and 0.402 μm wavelengths, and their Cauchy fitting dispersion curves. The refractive index of the uncured resist (black, 1) reduces slightly after UV cure at	

365 nm and hard bake at 50 °C (red, 2), but decreases more significantly if a low-index monomer was diffused into the photoresist matrix before UV cure and hard bake (blue, 4). The index of previously cured resist (red, 2) hardly changes after the monomer diffusion process (green, 3).....	30
Figure 2.8. Impact of prebake temperature on the resist refractive index.....	31
Figure 2.9 (a) Absorption spectra of the corresponding photo acid generators and the sensitizer; Surface roughness of the cured resist after chemical bath of the resist without sensitizer (b) and with the sensitizer (c); (d) Voxel height of waveguide core as a function of laser power of the resist with (black) and without sensitizer (red);.....	33
Figure 3.1 Nanoscribe setup	37
Figure 3.2 How the defocus factor was calculated (combine 2 pics)	39
Figure 3.3 (a) Side-view SEM micrograph of single lines after developing the unexposed resist and closer view of the periodic height variation along the writing direction (b) Relation between input laser intensity and voxel height in direct laser writing. Margin of error from the voxel height measurement is $\pm 0.2 \mu\text{m}$. Linear fitting shows the possibility to adjust voxel height by adapting laser intensity at different writing speeds. Higher writing speed results in a smaller core dimension.	40
Figure 3.4. Side view (a) and top view (b) of the optical setup with a field aperture placed closely in front of the microscope objective to modify the spatial beam shape in the focus plane. The slit is oriented parallel to the writing direction (x direction). Physical optics propagation (POP) simulation results from ZEMAX show the intensity distribution in false color of the laser beam at focus plane without a slit (c) and with a 250 μm slit (d). SEM picture of a single-sweep written line at the surface of the silicon wafer show a voxel width in transverse y-direction without (e) and with (f) a 250 μm slit; the unexposed volume (the cladding) was totally removed by developing with PGMEA.....	43
Figure 3.5 Fabrication process.....	45
Figure 3.6 Spin curve of the host oligomer.....	47

Figure 3.7 Second prebake at 55° for 1 hour could remove striations and wrinkles.	48
Figure 3.8 (a) Microscope picture of the end facet of a waveguide (b) schematic of multi-sweeping (c) SEM pictures of a waveguide core with multi-sweeping.	49
Figure 3.9 Stop and go issues at connection points in writing trajectory (a) schematic of parallel sweeping where connection points were in line at the same z-coordinates (b) lower writing speed caused a higher dose at the connection points (c) by shifting the sweeping lines one after the other, these connections are no longer visible.....	52
Figure 3.10 Impact of post exposure baking temperature on stability of inscribed structures. 410-µm thick samples were baked to temperatures between 50 °C and 70 °C, differing in shifting and bends.	54
Figure 3.11 Concentration profile of monomer at the gaseous monomer and solid oligomer interface.....	56
Figure 3.12 (a) Diffusion chamber at mrt; (b) Diffusion chamber Ecolav at KIT;	58
Figure 3.13 The so-called hair in the soup (HaSS) effect: top views of waveguides before and after external diffusion at 70 °C for 72 hours. The sample was 400 µm thick and the waveguide core dimensions are larger than 6µm.....	59
Figure 3.14 Rotation of the core and the moving of the waveguide cores which are supposed to be inline.....	60
Figure 3.15 Elongation of the written waveguide during the diffusion process. ...	61
Figure 3.16 The free flowing of over-exposed markers eliminates the possibility of the polymerization continuation causing the bends and drifting. The markers were written at the top surface of the resist which worsens the HaSS.....	61
Figure 3.17 Swelling in the diffused region compared to cured region. The region cured before diffusion did not swell since there is no diffusion.....	62
Figure 3.18 Diffusion depth as a function of diffusion time and temperatures with swelling (dotted lines) and after subtracting swelling (continuous lines).....	63
Figure 3.19 Vertical distribution of refractive index for waveguide cores and cladding measured by refracted near field method.....	64

Figure 3.20 From left to right: wafer deformation due to over baking; surface bubbles due to over baking; furrows due to under exposure.....	65
Figure 3.21 Shadowing effect below the written waveguides at two different exposure angles.....	66
Figure 3.22. DSC measurement for analyzing curing and softening process of the photopolymer before and after diffusion: The samples were heated up from -20 °C to 150 °C at a constant heating rate of 10 °C/min; Diffusion of monomer broadens the exothermic peak from both sides of the temperature range.....	68
Figure 4.1 a) top view and (b) end facet view of waveguide with core dimensions of 5.7 μm; (c) SEM picture of the core after developing the uncross-linked cladding matrix with end facet view	72
Figure 4.2 Area refractive index profile of a sample waveguide at the end facet measured with refracted near field method in 3D graph (a) and its cross section at x=0 (b). The peak index contrast between core and cladding at 678 nm is 0.013 73	
Figure 4.3 Near-field measurement system by HAMAMATSU. * Adapted from www.hamamatsu.com	75
Figure 4.4. (a) Top view of a sample with 3 waveguides at a distance of 200 μm. (b) End facet view of a waveguide (written at speed of 200 μm/s and input laser power of 42 mW); core dimensions are 6.9 μm x 6.9 μm. (c) BeamPROP simulation of intensity distribution of guided mode for this sample waveguide. (d) Measured near field profile illustrated with false color presents single guided mode at 1310 nm wavelength coupled from Corning SMF-28e single-mode fiber (central plot).	75
Figure 4.5 Near field pattern of the waveguides measured at transmission wavelengths: Near field intensity profile in false color measured at 850 nm in comparison with the physical core, and its cross sections in x and y at 850 nm (a, b) and at 1550nm (c, d). The 1/e ² mode field diameters are both 5.7 ± 0.3 μm at 850 nm and both 7.4 ± 0.4 μm at 1550nm. Black curve: measured intensity profile; red curve: Gaussian fitting.....	76
Figure 4.6 Far field pattern measured at 850 nm and its intensity profile cross sections.....	78
Figure 4.7 Insertion Loss at 850 nm	79

Figure 4.8 Bend loss vs. Radius of curvature at 1310 nm and 1550 nm for waveguides of 2mm length with sine function. Right: end facet images of 2 waveguides in the sample wafer showing shifted voxel.....	81
Figure 4.9 Illustrated definition of PDL through Poincaré sphere.....	82
Figure 4.10. Characterizations of a 4x2 waveguide array: (a) End facet microscope picture shows high contrast between waveguide cores and cladding, and satisfying alignment accuracy between top and bottom layer; (b) qualitative isometric view of refractive index profile measured by refracted near field portrays homogeneity of the cladding; (c) Near field pattern introduces guiding mode in a waveguide core and invisible crosstalk to neighboring waveguides (dotted frame marks the positions of the neighboring waveguide cores)	85
Figure 4.11 Transversal distribution of refractive index for waveguide cores and cladding measured by refracted near field method.....	86
Figure 4.12 (a) Schematic of an optical 3-core fanout for pitch conversion in both vertical and horizontal direction; End facet microscope picture of the input (b) and output (c) of the prototype; Two-dimensional pitch of 35 μm is converted to a linear pitch of 250 μm ; (d) Near field profiles at the output facets which were measured separately; (e) Horizontal cross section of near field profile of the waveguide 1 and its Gaussian fitting curve (red) (f) Top view microscope picture by aligning a series of photos	87
Figure 4.13 The beam profiles of WG#6, Group#2 after first bake (A) and second bake (B). The intensity of the laser used is 0.79mw, 0.89mw respectively. The beam profiles are almost identical.	89
Figure 5.1 Concept of decoupling the vertical pitch size from horizontal pitch size to increase the interconnect density	90
Figure 5.2 Process flow for optoelectronic integration of multi-layer waveguide array	91
Figure 5.3 LIFT topview : LIFT bumps on top of connecting pads.....	94
Figure 5.4 Laser ablation principle (a) and the resulting ablated mirrors by different mask width: 1000 μm (b) 500 μm (c) and 200 μm (d)	96

Figure 5.5 Ablation depth and negative facet angle as a function of scanning steps with laser tilt angle of 298 ° (a) and 294 ° (b); Side view of two layer 45 ° mirrors (c).....	97
Figure 5.6 Flip chip boning : (a) top view of a metalized resist sample; (b) μ -bumps and contact pads; (c) light coupling of two-layer integration.....	98
Figure 5.7 (a) Flatness of the negative facet of the TIR mirror captured through SEM micro-graph and its zoom-ins (b, c).....	99
Figure 5.8 Surface roughness quantified by Wyco optical profiler. (a) the 3D surface profile of the negative facet; (b) L shape profile with a linear slope after the first 20 μ m; roughness in vertical (c) and horizontal direction (d).....	100
Figure 5.9 Near field scanning of the guided modes for (a) between single mode fiber and multimode fiber (SM-MM) as the reference, (b)device under test as a waveguide (c)device under test as a waveguide and a mirror; and the setup layout (d).....	101
Figure 5.10 Simulation with Lumerical for the coupling loss between fiber and waveguide using total internal reflection mirror	103
Figure 5.11 Insertion loss setup	103

List of publications

Journal publications

- [1].H. H. D. Nguyen, U. Hollenbach, S. Pfirrmann, U. Ostrzinski, K. Pfeiffer, S. Hengsbach, and J. Mohr, "Photo-structurable polymer for interlayer single-mode waveguide fabrication by femtosecond laser writing," *Opt. Mater. (Amst)*. **66**, 110–116 (2017)
- [2].Ho Hoai Duc Nguyen, Uwe Hollenbach, Ute Ostrzinski, Karl Pfeiffer, Stefan Hengsbach, and Juergen Mohr, "Freeform three-dimensional embedded polymer waveguides enabled by external-diffusion assisted two-photon lithography," *Appl. Opt.*55, 1906-1912 (2016) *
- * Earned highlight in Spotlight on optics from Optical Society:
<https://www.osapublishing.org/spotlight/summary.cfm?id=336977>
- [3].Duc H. H. Nguyen, Kerstin Kaleta, Stefan Hengsbach, Ute Ostrzinski , Karl Pfeiffer, Uwe Hollenbach, Jürgen Mohr, " Three-dimensional buried polymer waveguides via femtosecond direct laser writing with two-photon absorption ", *Proc. SPIE 9130, Micro-Optics 2014, 91300N* (May 2, 2014).

Patents

- [1]. Duc H. H. Nguyen , patent application: "In-situ coupling from fiber laser to integrated circuit board for Lidar sender"

Conferences

- [1].Duc H. H. Nguyen, Stefan Hengsbach, Kerstin Kaleta, Ute Ostrzinski , Karl Pfeiffer, Uwe Hollenbach, Jürgen Mohr, " Three-dimensional on-board optical Interconnects enabled by femtosecond direct laser writing in polymer", *Proc. DGaO, 115th Annual Conference, 2014*.
- [2].Duc H. H. Nguyen, Uwe Hollenbach, Kerstin Kaleta, Stefan Hengsbach, , Ute Ostrzinski , Karl Pfeiffer, Jürgen Mohr, "Freeform three-dimensional polymer

waveguides for on-board optical interconnects”, Poster, Summer School on Optical Interconnects, Greece, 2014.

[3].Duc H. H. Nguyen, Uwe Hollenbach, Kerstin Kaleta, Stefan Hengsbach, , Ute Ostrzinski , Karl Pfeiffer, Jürgen Mohr, “Direct laser writing for three-dimensional on-board optical interconnection”, Poster, Helmholtz Day of Teratronics, Germany, 2014.

[4].Duc H. H. Nguyen, Uwe Hollenbach, Kerstin Kaleta, Stefan Hengsbach, , Ute Ostrzinski , Karl Pfeiffer, Jürgen Mohr, “3D buried waveguides in photopolymers using two-photon laser lithography”, Poster, Karlsruhe Days of Optics & Photonics 2013

Curriculum Vitae

Ho Hoai Duc NGUYEN

Education

- 2012 – 2016 Karlsruhe Institute of Technology (KIT), Germany
PhD candidate, Helmholtz Institute of Microstructure Technology (IMT)
Earned highlight of the research results in [Spotlight on optics](#) from Optical Society
- 2014 - 2015 HECTOR School of Engineering & Management, Karlsruhe, Germany
Master of Business Administration Fundamentals (MBA)
- 2010 - 2012 **Europhotonics Master Program**, Erasmus Mundus Scholarship
Master of Science in Optics and Photonics, Marseille-France and KIT, Germany